



저작자표시-비영리-변경금지 2.0 대한민국

이용자는 아래의 조건을 따르는 경우에 한하여 자유롭게

- 이 저작물을 복제, 배포, 전송, 전시, 공연 및 방송할 수 있습니다.

다음과 같은 조건을 따라야 합니다:



저작자표시. 귀하는 원저작자를 표시하여야 합니다.



비영리. 귀하는 이 저작물을 영리 목적으로 이용할 수 없습니다.



변경금지. 귀하는 이 저작물을 개작, 변형 또는 가공할 수 없습니다.

- 귀하는, 이 저작물의 재이용이나 배포의 경우, 이 저작물에 적용된 이용허락조건을 명확하게 나타내어야 합니다.
- 저작권자로부터 별도의 허가를 받으면 이러한 조건들은 적용되지 않습니다.

저작권법에 따른 이용자의 권리는 위의 내용에 의하여 영향을 받지 않습니다.

이것은 [이용허락규약\(Legal Code\)](#)을 이해하기 쉽게 요약한 것입니다.

[Disclaimer](#)

공학박사 학위논문

Upconversion in Lanthanide-doped Structurally Disordered Host Matrix

란탄족 이온이 도핑된 구조적으로 무질서한
호스트 매트릭스에서의 상향변환 특성 연구

2019 년 8 월

서울대학교 대학원

재료공학부

문 병 석

Upconversion in Lanthanide-doped Structurally Disordered Host Matrix

란탄족 이온이 도핑된 구조적으로 무질서한
호스트 매트릭스에서의 상향변환 특성 연구

지도교수 김 현 이

이 논문을 공학박사 학위논문으로 제출함

2019 년 6 월

서울대학교 대학원

재료공학부

문 병 석

문 병 석의 박사학위 논문을 인준함

2019 년 6 월

위 원 장	남 기 태	(인)
부 위 원 장	김 현 이	(인)
위 원	선 정 윤	(인)
위 원	고 영 학	(인)
위 원	김 동 환	(인)

Abstract

Upconversion in Lanthanide-doped Structurally Disordered Host Matrix

Byeong-Seok Moon

Department of Materials Science and Engineering

Seoul National University

Lanthanide trivalent ions (Ln^{3+}) embedded in an inorganic host solid are capable of a unique optical phenomenon, upconversion, which sequentially absorbs multiple low-energy photons to convert them into a higher-energy photon via abundant energy levels of 4f-4f transitions. Upconversion suggests the promising applications, such as energy harvesting for solar cells, 3D volumetric display or deep tissue optogenetics. In recent years, the enormous efforts were dedicated to enhancing upconversion efficiency and tuning emission spectra for the diverse applications. Host engineering is one of the most powerful approaches because the intrinsic optical properties of lanthanides are determined by the non-centrosymmetric

crystal-field interaction with host ions at an atomic level. In general, the host matrix with lower local symmetry poses the larger crystal-field interaction, resulting in enhanced upconversion efficiency. To break the local symmetry, various strategies have been demonstrated in terms of doping interstitial impurities, exerting external electric field or pressure. However, despite the great progress, the ordering nature of inorganic species, in other words, the short-range (1st coordination) order inherited in conventional crystal and glass materials, still constrains the boundary of host engineering.

In this thesis, a new class of upconversion host material, which developed by hyper-quenching of the molten inorganic species to possess completely amorphous microstructure without short-range order, is investigated. It is found that the transition probabilities of lanthanides which elevated by non-centrosymmetric crystal-fields in this host material effectively enhances the upconversion emission of Er^{3+} to realize bright single-band emission at green region with exceptionally fast decay time. This phenomenon accompanies minimal energy loss in two-photon upconversion in contrast to previously demonstrated single-band upconversion at red or NIR regions which were realized via complex energy transfer pathways that fatally inherit the dissipative energy loss by phonon generation. Furthermore, the altered balance of transition probabilities was found to effectively alleviate detrimental nonradiative energy transfers, such like cross-relaxation

and energy back transfer. This unique feature provides a significant privilege to establish population inversion in the excited states of lanthanides, which facilitating much efficient upconversion lasing than the other materials ever reported. All these findings, including the development and the characterization of structurally disordered host matrix, will bring the invaluable insight for designing future upconversion devices, which paves the way for the potential applications.

Keywords: Lanthanide-doped inorganic materials, Upconversion, Host engineering, Single-band emission, Microlasers

Student number: 2014-21475

Table of contents

Abstract	i
List of Tables	vii
List of Figures	viii
Chapter 1 Introduction	1
1.1 Upconversion in lanthanide-doped materials and emerging applications	2
1.2 The state-of-the-art engineering technologies	3
1.2.1 Upconversion nanocrystals as a nanowaveguide	4
1.2.2 Upconversion enhancement by a single plasmonic particle	13
1.3 Host engineering: breaking local symmetry	20
1.4 Thesis outline	21
Chapter 2 Ultrafast single-band upconversion luminescence in a liquid- quenched amorphous matrix	33
2.1 Introduction.....	34
2.2 Materials and methods	36
2.3 Laser-induced liquid-quenching of upconversion nanoparticles	40
2.4 Single-band upconversion luminescence at green spectral region	42
2.5 Theoretical interpretation: Judd-Ofelt theory	43

2.5.1	Judd-Ofelt theory and optical properties of lanthanides	43
2.5.2.	Calculating the relative Judd-Ofelt parameters.....	45
2.5.3	Correlation with host matrix's microstructure.....	49
2.6	Upconversion pathway of liquid-quenched amorphous host matrix.....	50
2.7	Verification of mechanism with alternative dopants.....	54
2.8	Conclusion	55
Chapter 3 Ultralow-threshold wavelength-tunable continuous-wave upconversion microlasers.....		77
3.1	Introduction.....	78
3.2	Materials and methods	81
3.3	Liquid-quenched upconversion microspheres as an optical resonator.....	84
3.4	Continuous-wave upconversion lasing.....	85
3.5	Lasing threshold investigation	87
3.6	Classical laser physics.....	88
3.7	Robust operation and reversible wavelength-tunability.....	91
3.8	Conclusions.....	94
Chapter 4 Conclusion and outlook.....		107
4.1	Conclusions.....	108
4.2	Outlook	109
References.....		110

Abstract (Korean)	127
--------------------------------	-----

List of Tables

Table 2.1. Reduced matrix elements of the visible Er^{3+} transitions for the relative JO parameters calculation [111].	67
Table 2.2. Upconversion luminescence decay times of $\beta\text{-NaYF}_4$ and A- $\text{NaYF}_4\text{:SiO}_2$ co-doped with Yb^{3+} and Er^{3+} ions.....	68

List of Figures

Figure 1.1. (a) Comparison of conventional luminescence and upconversion luminescence [79]. (b) Energy transfer upconversion of Tm^{3+} (Er^{3+}) and Yb^{3+} co-doped system [8].	23
Figure 1.2. Schematic representation of upconversion mechanism [80]. (a) Excited state absorption (ESA). (b) Energy transfer upconversion (ETU). (c) Cooperative sensitization upconversion (CSU). (d) Energy migration upconversion (EMU). A: activator ion, S: sensitizer ion, L: ladder ion and M: migratory ion.	23
Figure 1.3. (a) Microscopic upconversion materials with various shape and size [81]. (b) Upconversion emission spectra with various dopants [1].	24
Figure 1.4. Examples of emerging applications of microscopic upconversion materials [80].	24
Figure 1.5. (a) SEM image of $\text{NaYF}_4:\text{Yb}^{3+},\text{Tm}^{3+}$ nanocrystal. Inset shows the magnified view. (b) Element mapping of $\text{NaYF}_4:\text{Yb}^{3+},\text{Er}^{3+}$ nanocrystal. (c)-(d) Optical images of $\text{NaYF}_4:\text{Yb}^{3+},\text{Tm}^{3+}$ nanocrystal and $\text{NaYF}_4:\text{Yb}^{3+},\text{Er}^{3+}$ nanocrystal subjected to 980-nm excitation, respectively.	25
Figure 1.6. XRD pattern of $\text{NaYF}_4:\text{RE}$ nanowire powder and standard card of $\beta\text{-NaYF}_4$.	25
Figure 1.7. (a) Optical pathway of dark-field microscope equipped for UCL	

measurement. (b) Optical image of individual $\text{NaYF}_4:\text{Yb}^{3+},\text{Tm}^{3+}$ nanocrystal excited by 980-nm laser. The yellow regions are where the emission spectra are acquired ($250\text{ nm} \times 400\text{ nm}$). (c) UCL spectra emitted from end and middle of single $\text{NaYF}_4:\text{Yb}^{3+},\text{Tm}^{3+}$ nanocrystal. (d) Integral UCL intensity ratio between end and the midpoints for different emission wavelengths. (e) UCL spectra at different positions of single $\text{NaYF}_4:\text{Yb}^{3+},\text{Tm}^{3+}$ nanocrystal. (f) Normalized integral UCL intensity for blue, red, NIR, and total emission (as defined in c) at different nanocrystal positions. (g) Optical image of $\text{NaYF}_4:\text{Yb}^{3+},\text{Er}^{3+}$ nanocrystal and UCL spectra at end and midpoint of nanocrystal.....26

Figure 1.8. Upconversion emission process of $\text{Yb}^{3+},\text{Tm}^{3+}$ co-doped NaYF_4 .
.....27

Figure 1.9. (a) Schematic of UC populating mechanism for $\text{NaYF}_4:\text{Yb}^{3+},\text{Er}^{3+}$. (b) Integral UCL intensity ratio between the end and the middle point at different emission wavelengths in a single $\text{NaYF}_4:\text{Yb}^{3+},\text{Er}^{3+}$ nanowire subject to 980-nm excitation. Note the multiband emissions of $\text{Yb}^{3+},\text{Er}^{3+}$ ion-doped NaYF_4 , assigned to $^2\text{H}_{11/2} \rightarrow ^4\text{I}_{15/2}$ at 525 nm, $^4\text{S}_{3/2} \rightarrow ^4\text{I}_{15/2}$ at 550 nm and $^4\text{F}_{9/2} \rightarrow ^4\text{I}_{15/2}$ at 660 nm, respectively. The corresponding UC populating mechanism is shown in Fig. S3(a). Interestingly, compared with the end and middle emissions of a single $\text{NaYF}_4:\text{Yb}^{3+},\text{Er}^{3+}$ nanowire, the long-wavelength emissions in the middle of the nanowire are enhanced in a wavelength-

dependent manner.27

Figure 1.10. (a) Upconversion luminescence spectra at different points in a single NaYF₄:Yb³⁺,Er³⁺ nanowire subject to 980-nm illumination. (b) Integral intensity of green emissions (²H_{11/2},⁴S_{3/2}-⁴I_{15/2}), red emissions (⁴F_{9/2}-⁴I_{15/2}), and total emissions at the different positions in the NaYF₄:Yb³⁺,Er³⁺ nanowire.28

Figure 1.11. (a) Proposed UC multicolor emissions in single NaYF₄:Yb³⁺,Tm³⁺ nanocrystal. (b) Optical images and lifetime curves (blue emissions) of agglomerated and monodispersed NaYF₄:Yb³⁺,Tm³⁺ nanocrystals, respectively. (c) ²H_{11/2}-⁴I_{15/2} emission/⁴S_{3/2}-⁴I_{15/2} emission ratio (R_{HS}) at different positions in a single NaYF₄:Yb³⁺,Er³⁺ nanocrystal subject to 980-nm excitation. (d) Calculated confined power and critical angle for total internal reflection at different UC emission wavelengths in single NaYF₄:Yb³⁺,Tm³⁺ nanocrystals. (e) Proposed populating mechanism in single NaYF₄:Yb³⁺,Tm³⁺ nanocrystal subject to 980-nm excitation.29

Figure 1.12. Experimental setup and sample characterization. a-b. Experimental setup (a) and investigation scheme (b) of the UCNP monolayer coupled with a gold plasmonic nanoparticle. c-d. SEM images of the UCNP monolayer coupled with AuNTs (c) and AuNSs (d). (Inset: SEM images of synthesized AuNTs and AuNSs.) e-f. UV-Vis/NIR spectra of AuNTs matched

with the UCNP excitation wavelength (e) and AuNSs matched with the UCNP emission wavelength (f)..... 30

Figure 1.13. Dark-field image of AuNT (a) and AuNS (b) coupled with the UCNP monolayer. c-d, Scattering spectra of selected AuNTs (c) and AuNSs (d) identified by white circles in (a) and (b), respectively. e-f, luminescence spectra of a UCNP monolayer coupled with AuNTs (e) and AuNSs (f). The green curves show the reference spectra and the inset in (f) shows a magnified view of spectrum at 656 nm. 31

Figure 1.14. Enhancement factors of the intensity for the excitation coupling (a) and the emission coupling (b) depending on the LSPR peak wavelength variation from the excitation and emission wavelengths (groups 1 to 5).... 32

Figure 1.15. Upconversion host engineering based on breaking local symmetry. (a) Upconversion enhancement by interstitial Li^+ ion doping [76]. (b) External electric field induced upconversion enhancement [77]. (c) Mechanical strain induced upconversion enhancement [78]..... 32

Figure 2.1. Optical setup for laser focusing and spectral and lifetime analyses of upconversion materials. 57

Figure 2.2. Laser-induced full melting and instant quenching process. Highly crystalline $\beta\text{-NaYF}_4$ nanocrystals were used as the initial material. A pretreatment process, as described above, was performed to facilitate the

whole process. Only the heat by laser irradiation was used to liquefy the precursors. The molten precursors were then spontaneously quenched by the extinction of the surface effect. The spherical particle shape of the sample indicates that the precursors were fully melted and shaped to minimize their surface energy. The entire process was initiated and terminated under 980 nm CW laser of $3 \times 10^6 W/cm^2$ 58

Figure 2.3. Partially melted nanocrystals in a crumb larger than 10 μm during laser irradiation. The temperature of the crumb was elevated via the rapid heat accumulation, which involved a number of nanoparticles in the focusing spot absorbing energy and then dissipating heat into the surroundings. Whereas a small crumb of a few nanoparticles cannot induce adequate heat accumulation, for a large crumb larger than $\sim 10 \mu m$, the heat dissipation into the surroundings prevents heat accumulation. As a result, the size of the homogeneous liquid-quenched sample was limited from several hundred nanometers to several microns, which is comparable to the size of the focused laser spot. 59

Figure 2.4. Single-band upconversion luminescence of the liquid-quenched amorphous $NaYF_4:SiO_2$ co-doped with Er^{3+} and Yb^{3+} : (a) Schematic of the liquid-quenched amorphous $NaYF_4:SiO_2$ (A- $NaYF_4:SiO_2$) synthesis from crystalline β - $NaYF_4$ nanocrystals coated with a thin SiO_2 layer using laser irradiation. (b-c) SEM images of a crumb of β - $NaYF_4$ nanocrystals and as-

synthesized A-NaYF₄:SiO₂ on the substrate at low (b) and high magnification (c). (Color insets are the color images of typical upconversion emission from β -NaYF₄ and A-NaYF₄:SiO₂). (d-e) TEM images of \sim 45 nm-diameter β -NaYF₄ nanocrystals coated with an \sim 8 nm SiO₂ layer (d) and the corresponding lattice structure (e). (f-g) TEM cross-sectional image of A-NaYF₄:SiO₂ (f) and its halo-like SAED pattern (g). (h) Single-band upconversion emission spectrum of A-NaYF₄:SiO₂ (20%, 2%) compared with the multiband upconversion of β -NaYF₄ (20%, 2%) under 980 nm CW laser irradiation at 3×10^6 W cm⁻². The intensity of each spectrum is normalized by volume of the acquired samples. 60

Figure 2.5. The application of an amorphous phase stabilizer: a thin layer of SiO₂ coated onto the β -NaYF₄. a-b, TEM-EDS analysis of β -NaYF₄ (a) and β -NaYF₄@SiO₂ nanocrystals (b). A thin layer of SiO₂ of \sim 8 nm was introduced and confirmed by TEM observation and EDS analysis. (c), The average size of the synthesized nanocrystals was 45.8 nm, and the SiO₂ layer thickness was \sim 8 nm. (d), SAED of the β -NaYF₄ nanocrystals. A sharp ring-type diffraction pattern was observed because nanocrystals can be considered as a polycrystalline material. 61

Figure 2.6. Liquid-quenched host materials without SiO₂ stabilizer. a-b, Laser-induced liquid-quenching was applied to β -NaYF₄ without SiO₂ (a); however, without the amorphous phase stabilizer SiO₂, the quenched matrix

was semi-crystalline because of spontaneous recrystallization (left side of b, white arrows indicate amorphous regions), as confirmed by the SAED (selected area electron diffraction) patterns (right side of b). c, Chemical composition of the liquid-quenched NaYF₄ was not changed from that of the initial β -NaYF₄ (cf. Figure 2.5a) during the liquid-quenching process, as confirmed by TEM-EDS analysis (Ni, Ga and Pt originated from the sample preparation process). d, Insufficient change in the upconversion spectrum was observed in the liquid-quenched NaYF₄. Notably, because of the amorphous regions, the $^2H_{11/2} \rightarrow ^4I_{15/2}$ transition of the liquid-quenched NaYF₄ was substantially enhanced compared with that of the untreated β -NaYF₄. 62

Figure 2.7. Cross-sectional investigation of liquid-quenched amorphous NaYF₄:SiO₂ (A-NaYF₄:SiO₂). a-b, SEM image of the as-synthesized A-NaYF₄:SiO₂ (a) and its cross-sectional analysis (b). The thin film of the cross-section was prepared by focused ion beam (FIB) milling for HRTEM analysis. c, The amorphous region was partially crystallized (inset) when the electron beam (200 kV) was focused for high magnification. Usually, a non-glassy amorphous structure experiences recrystallization when it is heated or irradiated by an electron beam, whereas a glassy amorphous structure experiences a glass transition or melting [102,126]. d, The matrix exhibits a typical halo-like pattern of an amorphous structure in the SAED (selected area electron diffraction) pattern. 63

Figure 2.8. Chemical homogeneity of the liquid-quenched amorphous matrix. a, TEM-EDS mapping images of as-synthesized A-NaYF₄:SiO₂, Yb³⁺, Er³⁺ (20%, 2%). The chemical homogeneity was preserved during the process. The mapping image of Yb Lα1 was misconducted because of its spectral overlap with Ni Kα1. b, EDS spectrum of the mapping area and the calculated composition. Note that the EDS analysis is quasi-quantitative; thus, a rough composition of the analyte was obtained. The peak intensities of the elements were barely changed from the initial state (β-NaYF₄:Yb³⁺, Er³⁺ (20%, 2%)). The contents of Si and O were incorporated from the SiO₂ coating layer during the liquid-quenching process. Analytical elements are not included in the composition. (Ga: focused ion beam (FIB) gun source, Pt: protecting layer for FIB process, Ni: substrate, Cr: from the TEM detector, Cu: TEM grid) 64

Figure 2.9. Normalized integrated intensity over the entire visible range (400-700 nm) and over three color ranges (blue, green, and red: 400-500, 500-600, and 600-700 nm, respectively). a, The integrated intensity from each sample was collected using optical microscopy, and the volume was correlated using a TEM finder grid. The liquid-quenched amorphous matrix sample was approximated as a perfect sphere, and the approximate SiO₂ volume was extracted for a fair comparison. Approximately 80 nanocrystals with 45 nm diameters were used to calculate the total volume of the crystalline sample. The surface quenching effect of the nanocrystals was compensated by

applying an ‘ideal volume-to-size factor ($\times 1.25$ for a 45 nm nanocrystal)’ [96].

..... 65

Figure 2.10. Liquid-quenched amorphous $\text{Y}_2\text{O}_3:\text{SiO}_2$. a-b, The liquid-quenched $\text{Y}_2\text{O}_3:\text{SiO}_2$ (a) was separated into two phases; the crystalline and amorphous regions were confirmed by the HRTEM image (left image of b) and the SAED pattern (right image of b). Crystalline $\text{Y}_2\text{Si}_x\text{O}_{3+2x}$ was possibly formed during instant quenching. c-d, EDS mapping data confirming that the two separate phases are compositionally homogeneous (c) and the chemical composition calculated from EDS analysis (d). e, Upconversion emission of semi-crystalline $\text{Y}_2\text{O}_3:\text{SiO}_2$ was an intense green single-band spectrum similar to that of $\text{A-NaYF}_4:\text{SiO}_2$, despite the liquid-quenched microstructure being a mixture of crystalline and amorphous regions..... 66

Figure 2.11. Gaussian-Lorentzian-fitted single-band upconversion emission spectrum of $\text{A-NaYF}_4:\text{SiO}_2$, Yb^{3+} , Er^{3+} (20%, 2%)...... 68

Figure 2.12. (a-b) Normalized electric-dipole transition probabilities (a) and decay curves of the $^2\text{H}_{11/2} \rightarrow ^4\text{I}_{15/2}$ transition (b) of Er^{3+} embedded in $\beta\text{-NaYF}_4$ and $\text{A-NaYF}_4:\text{SiO}_2$. (c) Ternary diagram of the normalized electric-dipole transition probability difference (ΔED) between the 1st and 2nd probable transitions of Er^{3+} plotted by the relative values of the JO parameters ($\Omega^r_{\lambda=2,4,6}$, $\Sigma\Omega^r_{\lambda} = 1$). Marked points correspond to the relative JO parameters of Er^{3+} ions embedded in various host matrices. ($\text{A-NaYF}_4:\text{SiO}_2(*)$) is estimated in

the present study. Data for ErBr_3 vapor (\blacktriangle), molten $\text{LiNO}_3 + \text{KNO}_3$ (\blacktriangledown), and glass (\blacksquare) are from ref [113], and those for $\beta\text{-NaYF}_4$ (\blacklozenge) and crystals (\bullet) are from ref [109].)..... 69

Figure 2.13. Power dependence and temporal behavior of A- $\text{NaYF}_4\text{:SiO}_2$ co-doped with Yb^{3+} and Er^{3+} : (a) Upconversion luminescence spectra of intense single-band-emitting A- $\text{NaYF}_4\text{:SiO}_2$, Yb^{3+} , Er^{3+} (20%, 2%) under irradiation at various power densities of the 980 nm pump laser. (b-c) Power dependence of A- $\text{NaYF}_4\text{:SiO}_2$, Yb^{3+} , Er^{3+} over the entire pump power range (b) and the higher power range (c). The colored box indicates the range of linear dependent emission intensity. (d) Temporal behavior of $^2\text{H}_{11/2} \rightarrow ^4\text{I}_{15/2}$ and $^4\text{S}_{3/2} \rightarrow ^4\text{I}_{15/2}$ with increasing pump power density. (e) The decay time of $^2\text{H}_{11/2} \rightarrow ^4\text{I}_{15/2}$ as a function of the pump power density. (f) Intensity difference (ΔI) of $^4\text{S}_{3/2} \rightarrow ^4\text{I}_{15/2}$ between the initial rise and the subsequent decay. Dashed lines in (b), (d), (e) and (f) indicate the threshold power density of $7.5 \times 10^5 \text{ W cm}^{-2}$ at which the extraordinary temporal behavior of $^4\text{S}_{3/2} \rightarrow ^4\text{I}_{15/2}$ is observed..... 70

Figure 2.14. Power dependence of crystalline $\beta\text{-NaYF}_4\text{:Yb}^{3+}$, Er^{3+} (20%, 2%). a, Upconversion luminescence spectra of multiband $\beta\text{-NaYF}_4\text{:Yb}^{3+}$, Er^{3+} (20%, 2%) under low and high pump power densities of 980 nm laser excitation. **b-c**, Power dependence of the low-power saturated group (**b**) and the high-power saturated group (**c**) of $\beta\text{-NaYF}_4\text{:Yb}^{3+}$, Er^{3+} in a double-

logarithmic plot.	71
Figure 2.15. Energy diagram and upconversion pathways of β -NaYF ₄ :Yb ³⁺ , Er ³⁺	72
Figure 2.16. Upconversion luminescence decay curves of crystalline β -NaYF ₄ co-doped with Yb ³⁺ and Er ³⁺ ions.	73
Figure 2.17. Upconversion luminescence decay curves of A-NaYF ₄ :SiO ₂ co-doped with Yb ³⁺ and Er ³⁺ ions.....	74
Figure 2.18. Single-band upconversion luminescence of A-NaYF ₄ :SiO ₂ , Yb ³⁺ , Tm ³⁺ and the proposed mechanism of single-band upconversion: (a) Upconversion luminescence spectra of A-NaYF ₄ :SiO ₂ and β -NaYF ₄ co-doped with Yb ³⁺ and Tm ³⁺ (20%, 2%) at 3×10^6 W cm ⁻² . (b-c) Comparison of the power dependence (b) and the decay time (c) of $^1G_4 \rightarrow ^3H_6$ corresponding to the enhanced transition in the liquid-quenched amorphous matrix. The intensity was normalized to the end point of maximum power. (d) The proposed mechanism of the single-band upconversion in Er ³⁺ and Tm ³⁺ sensitized by Yb ³⁺ . Dotted, dot-dashed, dashed, and solid lines indicate non-radiative relaxation, photon absorption, energy transfer, and upconversion emission, respectively. CR indicates cross-relaxation.....	75
Figure 2.19. Upconversion luminescence spectrum of A-NaYF ₄ :SiO ₂ , Yb ³⁺ , Ho ³⁺ (20%, 2%).	76

Figure 3.1. Continuous-wave upconversion lasing in liquid-quenched upconversion microspheres (LQUM): a. Schematic of the fabrication of a LQUM and the upconversion lasing in the LQUM through a free-space beam with a 980-nm continuous-wave pump laser. The LQUM accommodates the upconversion lasing through energy transfer upconversion of the activator (Er^{3+} or Tm^{3+}) with the sensitizer (Yb^{3+}). b-c. SEM image of the LQUM at low (b) and high magnification (c). Because the direction of light circulation must be aligned perfectly with the circumference of the microsphere, a LQUM dangling on the TEM grid wall was selected for the formation of WGM resonators. d. The upconversion luminescence of UCNPs (below) and a LQUM with the upconversion lasing (above). Doping concentrations of Yb^{3+} and Er^{3+} were 20% and 2%, respectively. The color inset shows an optical microscopy image of the illuminated LQUM. e. The upconversion lasing supported by the energy transfer upconversion process in the LQUM. Short-dashed, dot-dashed, solid, long-dashed, and dotted lines indicate absorption, energy transfer, spontaneous emission, stimulated emission, and non-radiative relaxation, respectively..... 96

Figure 3.2. Study of the size of liquid-quenched upconversion microspheres (LQUM). a-b. Emission spectrum of upconversion lasing from LQUMs of various diameters. A LQUM of 1.46 μm in diameter (a) exhibits a low Q factor due to high curvature loss [130]. A LQUM of 2.14 μm in diameter (b) does not exhibit resonance wavelengths in the red emission band of Er^{3+} ; therefore, the upconverted photons of the red emission band could not

participate in the laser process. Therefore, to maximize the laser efficiency, we concluded that 2.44 μm is the optimal LQUM diameter in the present study, which is in line with the theoretical calculation [175]..... 97

Figure 3.3. Continuous-wave laser operation. a. The rise and decay times were measured using pulsed excitation with a 10- μs pulse width. b. Temporal stability analysis reveals that the continuous-wave laser operation is stable within the instrumental noise level. To investigate the temporal behavior, the excitation pulse was generated from a 980-nm continuous-wave diode laser equipped with an arbitrary function generator (Rigol, DG4102). The emission was measured by a Si-APD (Thorlabs, APD410A) and recorded with an oscilloscope (Rigol, DS2102A-S). The rise and decay curves were fitted with a single-exponential function to calculate the rise and decay times [72] using the equation $y = y_0 + A \times \exp^{-(x-x_0)/t}$ 98

Figure 3.4. Pumping polarization effect. a-b. Two cases of pumping depending on the pumping sides: the pumping far (a) and near (b) sides from the laser emission point. c-d. Polar plot of the intensity of laser emission along with the pumping polarization angle in the xy plane for the far (c) and near (d) sides. e-f. Emission spectrum with the pumping polarization angle in the xy plane (0° and 90°) for the pumping far (e) and near (f) sides. By controlling the pumping polarization angle, we confirmed that the laser emission exhibits negligible sensitivity to the pumping polarization. 99

Figure 3.5. Ultralow-threshold continuous-wave upconversion lasing: a-b. Emission spectrum of a LQUM doped with Yb^{3+} and Er^{3+} in green (a) and red (b) bands around the lasing threshold. The laser peaks corresponding to $^2\text{H}_{11/2} \rightarrow ^4\text{I}_{15/2}$, $^4\text{S}_{3/2} \rightarrow ^4\text{I}_{15/2}$ and $^4\text{F}_{9/2} \rightarrow ^4\text{I}_{15/2}$ are labeled to Peak_H, Peak_S and Peak_F, respectively. c-d. Generation (c) and linewidth saturation (d) of the laser peaks with increasing pump power density..... 100

Figure 3.6. Power dependence of upconversion lasing. a. Comparison of upconversion lasing and upconversion luminescence at different pump power densities. b-e. Power dependence of the intensities and the intensity ratios of upconversion lasing (b) and upconversion luminescence (c). Above the lasing thresholds, the upconversion lasing intensity increases proportionally with the upconversion luminescence intensity of the corresponding emission bands. This finding is confirmed by the identical intensity ratios of Peak_H/Peak_F and $^2\text{H}_{11/2}/^4\text{F}_{9/2} (\rightarrow ^4\text{I}_{15/2})$ in upconversion lasing (d) and upconversion luminescence (e), respectively. 101

Figure 3.7. Spatial, spectral, and polarization analysis of laser emission: a. Schematic of whispering-gallery-mode analysis in the LQUM determined by circulating directions (clockwise (CW) and counterclockwise (CCW)) and transverse modes (transverse magnetic (TM) and transverse electric (TE) modes). b. Spatially resolved spectrum of the laser emission from the LQUM. The narrow rectangular section was spatially selected by the spectrograph's

entrance slit and resolved using a high-resolution grating. c. Deconvolution of the laser peaks using Gaussian-Lorentz fitting. d-f. Polarization investigation of the laser peaks using the emission spectrum (d), a polar plot of the intensities (e) and the intensity ratio (f). The fitting curves in e and f were drawn by a cosine-square function. 102

Figure 3.8. Theoretical investigation of laser wavelength. a, The laser emission spectrum of a LQUM under a weak excitation of 0.01 MWcm^{-2} at room temperature was used to investigate the coldest pump conditions. b, Refractive index (n) curves were calculated from the transverse magnetic mode lasing wavelengths of a..... 103

Figure 3.9. Wavelength tuning of laser emission wavelengths: a. Schematic of wavelength tuning achieved by controlling the pump power density (ΔP) and operation temperature (ΔT). The initial lasing wavelength and the shifted lasing wavelengths under the control of the pump power density and operation temperature are indicated by λ_0 , λ_P and λ_T , respectively. b. Emission spectrum of the spectrally tuned laser peaks. $\Delta\lambda_P$ and $\Delta\lambda_T$ indicate the shifts in the lasing wavelength with the increase in pump power density (from 0.01 to 3.16 MW cm^{-2}) and operation temperature (from 298 to 423 K). c. Stability analysis in terms of static (above) and dynamic (below) operations. d-e. Linear plots of the laser peaks' wavelength as a function of pump power density (d) and operation temperature (e). 104

Figure 3.10. Microscopic heating of a sample. a. Schematic of the home-built heating system. b-c. SEM (b) and color (c) images of upconversion microparticles used for temperature calibration. d. Emission spectrum of the upconversion microparticles as a function of the metal ceramic heater's temperature. e. Calibrated temperature obtained using the intensity ratio, $^2H_{11/2}/^4S_{3/2} (\rightarrow ^4I_{15/2})$ of the upconversion microparticles..... 105

Figure 3.11. a. Upconversion luminescence and upconversion lasing in a LQUM doped with Yb^{3+} and Tm^{3+} (20% and 2%) b. Emission spectrum in the blue emission band around the lasing threshold of $\sim 1.5 \text{ kWcm}^{-2}$. c-d, SEM (c) and color (d) images of a LQUM measuring $1.99 \mu\text{m}$ in diameter doped with Yb^{3+} and Tm^{3+} 106

Chapter 1

Introduction

1.1 Upconversion in lanthanide-doped materials and emerging applications

Lanthanide trivalent ions (Ln^{3+}) embedded in an inorganic host solid are capable of a unique optical phenomenon, upconversion, which sequentially absorbs multiple low-energy photons to convert them into a higher-energy photon via abundant energy levels of 4f-4f transitions [1] (Figure 1.1). Owing to the presence of real intermediate energy levels, the upconversion of Ln^{3+} possesses much higher efficiency than other non-linear optical processes, such like second harmonic generation that excited by high peak power pulsed lasers (e.g., a nanosecond pulse laser), so can be excited by low cost continuous-wave near-infrared (NIR) diode lasers (e.g., 980 nm laser) [2]. The mechanism of upconversion can be classified into four schemes; excited state absorption, energy transfer upconversion, cooperative sensitization upconversion and energy migration upconversion (Figure 1.2). Among them, energy transfer upconversion, which is consist of sensitizer (e.g. Yb^{3+}) and activator (e.g. Er^{3+} , Tm^{3+} and Ho^{3+}), is considered to be the most efficient upconversion mechanism since the sensitizer provides significantly larger absorption cross-section than that of the activators [3].

From mid-2000s, the significant progress in the field of upconversion have been motivated by the development of microscopic upconversion materials spanning from micro- to nanoscale [4]. These microscopic

upconversion materials have been synthesized with various shape and size through a number of techniques and their emission spectra was carefully manipulated in the consideration of dopant selection [3] (Figure 1.3). Furthermore, the inorganic species, which typically used for hosting Ln^{3+} , provide excellent thermo-, chemical-, photostability [5]. Based on these advantages, a wide range of applications has been emerged such as security ink [6], detection of latent fingerprint [7], energy harvesting for solar cells [8], 3D volumetric display [9] and deep tissue optogenetics [10] (Figure 1.4). In particular, upconversion materials have proven its validity as a luminescent probe for chemical and biological applications with low fluorescence background and long life-time compared with other conventional probes, e.g., fluorescence dyes and quantum dots [5]. The core strategy for realizing these applications lies in the unique use of NIR light source to generate visible or ultraviolet lights which typically require higher-energy light sources in the case of other conventional materials. Despite these great potential and emerging applications, the practical use of upconversion materials still faces the challenges in low conversion efficiency and difficulty in fine tuning of emission spectra [11].

1.2 The state-of-the-art engineering technologies

For recent years, the enormous efforts have been dedicated to

understanding and improving the performance of upconversion materials. One of the effective strategies is dopant engineering. By varying the combination of dopants and their concentration, the complex energy transfer pathway between dopants (sensitizer-activator or activator-activator) can be desirably manipulated since the spatial distribution of dopants, i.e., interionic distance, acts crucial role in energy transfer rates. Another one is surface engineering such like core-shell structuring or ligand decorations, which has significant effect on materials smaller than 50 nm. The principles and the established milestones of aforementioned engineering strategies have been covered by many previous literatures [1,2,7,12-14]. In this chapter, therefore, the state-of-the-art engineering technologies of multidisciplinary perspectives to further expand the capability of upconversion materials is studied.

1.2.1 Upconversion nanocrystals as a nanowaveguide

One-dimensional, nanometer-scale optical waveguides, given their capability to guide light at the sub-wavelength scale, are especially attractive for application as building blocks for integrated nano- and micro-photonic systems for optical communication or biological sensing, where they can function as both active device elements and interconnects [15-22]. However, due to the difficulty associated with efficiently coupling the light into the nanowaveguides [23,24], luminescence-based nanowaveguides fabricated

using semiconductors and polymers have been introduced as alternative solutions for minimizing the coupling loss by directly producing emission light within the nanowaveguides under blue or ultraviolet light excitation [24-27]. Unfortunately, semiconductor- and organic polymer optical waveguides have exhibited only limited performance, such as their intrinsic narrow emission bands and unavoidable spectral distortion during their propagation in nanowaveguides [21,25-29]. Therefore, to achieve high-density multichannel transmission in nanoscale photonics, there is a demand for a medium which can guide multiple emission bands over a broad bandwidth while preventing any change to the spectral shape after propagation.

Lanthanide upconversion (UC) luminescence nanocrystals exhibit a broadband UC emission bandwidth from 300 to 900 nm and a relatively narrow channel linewidth under near-infrared (NIR) excitation [30-35]. Because the multiband emission in UC nanocrystals is enabled by the anti-Stokes process with a large Stokes shift, unexpected interference with the excitation light can be minimized, which is of importance in optical communications [34,36]. We also previously reported on the up-conversion enhancement in the islands of Au-Ag alloy/NaYF₄:Yb³⁺,Tm³⁺/Er³⁺ composite films [37]. Inspired by these unique advantages, we propose the use of UC materials as nanowaveguides to tackle issues often found in semiconductor/polymer-based nanowaveguides, because we hypothesize that an individual

UC nanocrystal may form a Fabry–Perot microcavity (where two fiber ends work as a partial reflecting mirror for the resonant oscillation) and serve as an optical waveguide along the axial direction [28,38]. Recently, Wang et al. observed directional light emission in a single micron-scaled NaYF₄ (with a diameter of 1–4 μm and a length of 10–20 μm) via photonic UC without the need for any special alignment under NIR irradiation [39]. However, to the best of our knowledge, there has been no report of a single optical waveguide using UC nanocrystals because of the limited measurement capability of the individual UC nanocrystals. There is a great need for a spectral and spatial in-depth analysis of the waveguide effects of sub-wavelength nanocrystals corresponding to wavelengths because the wavelength effect is critical in nanocrystals with a small mode-field diameter. For those reasons, we demonstrate that an individual NaYF₄:Yb³⁺,Tm³⁺ (Yb³⁺,Er³⁺) nanocrystal has the potential to act as a nanowaveguide and report on the optical characteristics in guiding the light in sub-wavelength scale.

Rare-earth-ion doped NaYF₄ nanocrystals (β -NaYF₄:18% Yb³⁺, 0.2% Tm³⁺ or β -NaYF₄:18% Yb³⁺, 2% Er³⁺) were synthesized using a liquid–solid–solution phase-transfer method [40,41]. As revealed by scanning electron microscopy (SEM) (Figure 1.5a), the NaYF₄ nanocrystals formed a regular hexagonal prism structure with smooth facets and were uniform in size (diameter ~ 190 nm, length ~ 2 μm). The characteristic peaks in the X-ray

diffraction (XRD) pattern of the material were a good match with the hexagonal NaYF₄ (PDF no. 16-0334) (Figure 1.6). Element mapping under a high-resolution transmission electron microscope (HR-TEM) revealed that all the elements are homogeneously distributed (see Figure 1.5b). Figure 1.5c, d show the fluorescence images of individual NaYF₄:Yb³⁺,Tm³⁺ and NaYF₄:Yb³⁺,Er³⁺ nanocrystals, respectively, when subjected to 980-nm excitation. The emission colors from the middle and the end of the β -NaYF₄:Yb³⁺,Er³⁺ nanocrystal appear different (red-shifted), implying the position dependency of the upconversion luminescence (UCL) emission.

To investigate the emissions of UC nanocrystals, a dark-field scattering imaging microscope was used. Figure 1.7a illustrates the optical layout of the dark-field microscope for UCL spectrum detection; the UCL spectrum emitted by the individual NaYF₄:Yb³⁺,Tm³⁺ nanocrystal was detected under 980-nm continuous-wave laser excitation (Figure 1.7b). Figure 1.7c shows the UCL spectra emitted from the end and the middle of the NaYF₄:Yb³⁺,Tm³⁺ nanocrystal (detection area: 250 nm \times 400 nm, as shown in Figure 1.7b). Compared to semiconductor/polymer nanowaveguides, the UC nanowaveguides exhibit narrow multiband emissions (with a linewidth of \sim 15 nm in full-width-half- maximum (FWHM)) over a broad bandwidth from UV to NIR. The emission peaks originate from the UC transitions of ¹D₂ \rightarrow ³F₄ at 451 nm, ¹G₄ \rightarrow ³H₆ at 480 nm, ¹D₂ \rightarrow ³H₅ at 513 nm,

$^1G_4 \rightarrow ^3F_4$ at 648 nm, and $^3F_3 \rightarrow ^3H_6$ at 726 nm and $^3H_4 \rightarrow ^3H_6$ at 800 nm, respectively (Figure 1.8) [42-44].

The UCL emissions from the middle of the UC nanocrystal are substantial compared with those emitted from the end, as shown in Figure 1.7b and c. The position-dependent UCL from the nanocrystal can be attributed to the fact that the long wavelength UCL (~600–900 nm) behaves differently from a short-wavelength UCL during the propagation. Because the diameter of the UC nanocrystal (which can be regarded as being equal to the mode-field diameter of the waveguide) is at the sub-wavelength level, the guided UCL at a longer wavelength will experience a higher propagation loss; this higher loss is due to the greater scattering around the middle of the nanocrystal. The integrated UCL intensity ratio between the emissions from the end and the middle positions are shown in Figure 1.7d. The position-dependent emission profiles from the long-wavelength UCLs are also apparent in Figure 1.7e and f; it was observed that, nearer the middle point, the emission levels of the long wavelengths increased. In contrast, the short-wavelength emission appears to be less position-dependent due to the mode-field diameter of the waveguide. Such position- and wavelength-dependent emissions of the UC nanocrystal are also observed with Er^{3+} -doped nanocrystal ($NaYF_4:Yb^{3+},Er^{3+}$) (Figure 1.7g, 1.9 and 1.10), suggesting that this phenomenon does not depend on a specific luminescence center. On the

other hand, either the non-uniform doping of rare-earth ions or a local thermal effect can lead to position-dependent UC emission [45,46]. Before proceeding further, therefore, we set out to verify those possible influences. First, Element mapping of NaYF₄:Yb³⁺,Er³⁺ nanocrystal (Figure 1.5b) shows uniform doping of rare-earth ions in the UC nanocrystal. Second, the temperature throughout the NaYF₄:Yb³⁺,Er³⁺ nanocrystal is homogeneous, because the intensity ratio between the ²H_{11/2}-⁴I_{15/2} and ⁴S_{3/2}-⁴I_{15/2} (R_{HS}) is independent of the position (Figure 1.11c) [46]. The R_{HS}, determined by the distribution of the electron population, is highly sensitive to the thermal energy distribution because of the narrow energy separation (~680 cm⁻¹) between the ²H_{11/2} and ⁴S_{3/2} [47]. All these observations suggest that the position-dependent emission depends on the intrinsic optical properties of the NaYF₄ nanocrystal.

The light propagation, confinement, and reabsorption in the UC nanocrystals are governed by the waveguide- and microcavity effects of the NaYF₄ nanocrystal [27,28]. Based on the wave nature of light, the fractional guided power in a UC nanocrystal can be derived from Maxwell's equation, which gives [28]

$$\eta = 1 - \left[\left(2.4e^{[-1/V]} \right)^2 / V^3 \right], \quad V = k(d/2)(n_{NW}^2 - n_0^2)^{0.5} \text{ and } k = 2\pi / \lambda$$

where λ is the wavelength, d is the waveguide diameter, and n_{NW} and n_0 are

the refractive indices of NaYF₄:RE and air, respectively. As shown in Figure 1.11(d), individual NaYF₄:RE nanocrystals exhibit strong wavelength-dependent confinement, e.g., 50% at 450 nm vs. 9.5% at 800 nm when $d = 190$ nm. Because the mode-field diameter of the UC nanocrystal is relatively smaller than the wavelength of the light, a long wavelength can only propagate over limited distances due to the severe scattering loss. If the mode-field diameter is larger than 800 nm, the short wavelength will experience a higher loss due to the higher light absorption coefficient of the UC nanocrystal in the ultraviolet region. This wavelength-dependent loss cannot be explained by ray optics (e.g. Snell's law or the critical angle) because the ray optics model the light as a ray and do not consider the wavelength of the light.

Due to the waveguide effect, UCL can propagate through the UC nanocrystal for a longer time, which allows the UCL to act as a Fabry-Perot micro-cavity. As a result of the Fresnel reflection, about 4.0% of the light is reflected from both ends of the waveguide. Thus, the light stays in the UC nanocrystal for an even longer time, which newly enables light re-absorption. Regarding the waveguide effect, the lifetime constant of the nanocrystal can be regarded as being shown in Figure 1.11b. The lifetime constant is determined by $\tau_1 = \tau_0 / (1 - \eta a)$, where τ_0 is the intrinsic lifetime constant, η represents the probability of photon re-emission according to the radiative

rate (a constant in the present study), a represents the re-absorption ratio. Furthermore, $a = (n - n_l)/n$, where n is the total number of emitting photons and n_l is the number of photons leaving the nanocrystal [48,49]. As shown in Figure 1.11b, the lifetime constant for an individual NaYF₄:Yb³⁺, Tm³⁺ nanocrystal ($\tau_S = \sim 480 \mu s$) is longer than that of agglomerated NaYF₄:Yb³⁺, Tm³⁺ nanocrystals ($\tau_A = \sim 400 \mu s$). This observation suggests an increase in the re-absorption ratio as a result of the fall in the number of photons leaving a nanocrystal (n_l) is caused by the waveguide effect [27,28]. Eric et al. highlighted the importance of the photon loss in the optical waveguide and reported on the use of subwavelength-diameter silica wires as a waveguide, which has a similar diameter and wavelength dependent refractive index as the NaYF₄:RE nanocrystals used in the present study [50,51]. Based on the above, we believe that the intrinsic re-absorption property of a NaYF₄:RE nanocrystal would allow it to be used as a building block for the construction of a nanowaveguide.

Because of both the waveguide- and microcavity effect of NaYF₄:RE nanocrystals, shorter-wavelength emissions are prone to an emission-reabsorption-emission process (Figure 1.11a) [27,28]. Although there is some loss due to non-radiative transition and cross-relaxation, this phenomenon leads to an increase in the longer-wavelength emissions in the middle of the NaYF₄:RE nanocrystal (Figure 1.11a, e). This explains the observed

wavelength- and position-dependent UCL. By making use of this phenomenon, NaYF₄:RE nanocrystals can be used as a wavelength-selective add/drop coupler, simply by selecting the coupling position along the length direction. Compared to existing semiconductor/polymer luminescence waveguides, a NaYF₄:RE nanocrystal can act as both a light source and an optical waveguide. In addition, the emission wavelengths remain unaltered with the propagation, which indicates that they can produce potentially high levels of fidelity in optical communications.

Consequently, we find that the multiband emissions from the NaYF:Yb³⁺,Tm³⁺(Yb³⁺,Er³⁺) nanocrystals are wavelength- and position-dependent (i.e., there is a strong long-wavelength emission in the middle of the nanocrystals) while the emission wavelengths remain unaltered during the propagation. These unique waveguide characteristics of a single NaYF:Yb³⁺,Tm³⁺(Yb³⁺,Er³⁺) nanocrystal can be attributed to the optical waveguide and microcavity effects. Compared to existing luminescence waveguides, UC NaYF₄:RE nanocrystals provide relatively narrow linewidth multiband emissions over a broad spectral range without any unexpected wavelength peak shift or distortion, which makes them well suited for application to a new class of waveguide couplers or optical waveguides.

Work presented in this section has been published in: "Spectral and Spatial Characterization of Upconversion Luminescent Nanocrystals as

Nanowaveguides", *Nanoscale*, 9 (26), 9238–9245 (2017).

1.2.2 Upconversion enhancement by a single plasmonic particle

While upconversion nanoparticles (UCNPs) have attracted significant interest in different areas including bio-imaging [52,53], controllable drug delivery [54,55], and solar cells [56], the luminescence of UCNPs has been significantly limited by the upconversion energy efficiency [57]. To overcome this issue, great effort has been devoted to selecting novel host materials [58] or optimizing the crystal field [59]. However, the energy conversion efficiency still remains low [60]. One of the representative methods to enhance the upconversion emission consists of taking advantage of plasmonic nanoparticles in the vicinity of UCNPs [61], i.e., using the so-called plasmonic coupling effect. The plasmon coupling has been proven to enhance the upconversion luminescence by one or two orders of magnitudes [57,62,63] by the amplification of the excitation source [57], the resonance of the emission light [64], as well as the increase of the emission rate [65] in the upconversion process [11].

To push the limits of understanding, pioneer studies were conducted in pairing systems of UCNPs and plasmonic nanoparticles in a single nanoparticle level, which is the ideal experimental setup to access its full-parameterization [11]. Despite remarkable achievements utilizing a marked

substrate [62], electron lithography-based templates [57], and atomic force microscope [66], there has been a lack of concern about the intrinsic variations of plasmonic nanoparticles such as their size and shape, which ultimately induce variations of localized surface plasmon resonance (LSPR) peak wavelengths [67]. This could be a potential problem for practical nanoparticle applications because the plasmonic electric field varies with morphological changes of plasmonic nanoparticles. [11]. Therefore, it is important to investigate the dependence of upconversion enhancement on variations of the LSPR peak in a systematic manner [68]. For those reasons, we study the dependence of upconversion enhancement on the LSPR peak variation in a single particle level by massive data collection which has not been attainable with the conventional particle-to-particle coupling system.

A monodispersed UCNPs was uniformly self-assembled as a monolayer on top of single plasmonic nanoparticles to provide a homogeneous coupling system (Figure 1.12a and b). Gold nanospheres (AuNSs) with 50 nm diameter and gold nanotriangles (AuNTs) with an edge length of 140 nm were used to match the 543 nm emission and 980 nm excitation wavelength of UCNPs, respectively. The density of plasmonic nanoparticles on the substrate was controlled to avoid undesired coupling effects from neighboring plasmonic nanoparticles. Upconversion nanoparticles (20 nm in diameter) were synthesized using a previously

published method [69] and self-assembled onto plasmonic nanoparticles as a uniform monolayer using an interfacial assembly method [65] to provide a homogeneous coupling system as shown in Figure 1.12c, d. While the plasmonic enhancement of luminophore is sensitive to the distances from plasmonic structures, in our system, we were able to conveniently investigate the upconversion luminescence of the UCNP monolayer by utilizing an averaged coupling scheme. The LSPR peak wavelength of individual plasmonic nanoparticles and the enhanced upconversion luminescence were investigated simultaneously using a dark field optical microscope equipped with a 980 nm laser. The weak shoulder peak of AuNT at around 650 nm is neglected despite a spectral overlap with $^4F_{9/2} \rightarrow ^4I_{15/2}$ UC emission peak. Therefore, AuNSs were used for emission coupling and AuNTs were used for excitation coupling, respectively. The emission at 656 nm of UCNPs appears to be stronger than that in the green region at around 550 nm due to the energy transfer among Yb^{3+} and energy back transfer from Er^{3+} to Yb^{3+} . The spectra of the solutions of as-synthesized AuNSs and AuNTs were measured by a UV-Vis/NIR spectrometer (Figure 1.12e, f). The LSPR peak of AuNS is well matched with the UCNP emission peak at a wavelength of 543 nm while the LSPR peak of AuNT encloses the excitation wavelength of 980 nm. Therefore, we used AuNS for emission coupling and AuNT for excitation coupling, respectively. The shoulder peak of AuNT around 650 nm was neglected due

to the small contribution compared to the main peak at 980 nm despite a spectral overlap with $^4F_{9/2} \rightarrow ^4I_{15/2}$ UC emission peak.

Figures 1.13a, b show dark field scattering images of plasmonic nanoparticles coupled with the UCNP monolayer. Even though the peak positions of ensemble LSPR, i.e., the averaged LSPR peak of many plasmonic nanoparticles in a solution, are well matched with the excitation and the emission wavelengths of UCNPs (Figure 1.12e,f), the individual plasmonic nanoparticles have an apparent variation in the LSPR peak positions due to their geometric inhomogeneity (Figure 1.13c,d), shown as the various colored spots in dark field images under white light illumination (Figure 1.13a,b). The scattering spectra of individual plasmonic nanoparticles and the luminescence spectrum of the UCNP monolayer were collected from 50 coupling spots. To investigate how the LSPR peak variation of plasmonic nanoparticles affects the enhancement of the luminescence spectrum of UCNPs, the collected data points were divided into 5 groups based on the degree of mismatch between the LSPR peak and the luminescence spectrum of UCNPs for both excitation and emission cases. Group 1 contains the plasmonic nanoparticles exhibiting LSPR peaks that deviated by 10 nm or less from the peak for the ensemble as-synthesized solution (their scattering spectra are shown in Figure 1.13c, d for excitation and emission coupling, respectively). For AuNTs, due to the limit of quantum efficiency of the CCD

camera beyond 900 nm ($< 50\%$), the shoulder peak of AuNT at around 661 nm was used to identify the LSPR peak wavelength deviation from the excitation wavelength. Similarly, groups 2, 3, 4, and 5 contain plasmonic nanoparticles with LSPR peak variations within 10–20, 20–30, 30–40, and 40–50 nm from the excitation or emission wavelengths. The obtained luminescence spectra of the UCNP monolayer coupled with plasmonic nanoparticles were compared with that of a reference UCNP monolayer. Representative spectra of group 1 are shown in Figure 1.13e, f for excitation and emission coupling, respectively. It can be seen that the UCNP luminescence intensity was enhanced by 3–4 times for the excitation wavelength coupling while it is slightly quenched for the emission wavelength coupling.

Figure 1.14 shows the dependence of the luminescence enhancement factor on the deviation of the LSPR peak wavelength from the excitation and emission wavelengths. The enhancement factor was calculated by dividing the luminescence intensity of the UCNP monolayer coupled with plasmonic nanoparticles by the intensity of the reference UCNP monolayer. For excitation coupling, the enhancement factor decreases from 3.26 to 1 along groups 1 to 5 (Figure 1.14a). The linear fit of the enhancement factor indicates that the enhancement factor decreases by 0.052 fold with every 1 nm shift of LSPR wavelength. In the case of group 5, the plasmonic effects are

diminished so the spectrum becomes almost equivalent to that of the reference UCNPs. The R-squared factor is 0.92, suggesting that the descending tendency of the enhancement factor along the deviation of the AuNT LSPR peak wavelength is highly reliable. Compared to a previous report that used a thin film system composed of multi-layered nanoparticles [68], the plasmonic wavelength dependence of the luminescence enhancement factor in this study is more substantial, probably due to the elimination of the averaging effect in the single particle level coupling system. On the other hand, for emission coupling, a slight decrease of upconversion luminescence is observed (Figure 1.14b). This is most likely attributed to a quenching effect between plasmonic nanoparticles and UCNPs; when a luminophore contacts a metal surface, quenching occurs due to energy transfer and non-radiative relaxation [66]. The linear fit of the enhancement factor exhibits a slope of 0.003 with an R-squared factor of 0.19, showing that the quenching process is not linearly dependent on the LSPR peak deviation in this coupling system. Interestingly, the most significant quenching takes place in group 2, which is deviated from the UCNP emission wavelength by 10 to 20 nm. Plasmonic enhancement is highly sensitive to the electric field intensity at an emission peak of fluorophore whereas FRET quenching is proportional to the overlapped area of spectra of donor and acceptor [70]. Therefore, at on-resonance, the plasmonic enhancement and the quenching are compensated

each other [71] but quenching takes place at 10-20 nm off-resonances. Note that, for the case of excitation coupling, due to the absence of spectral overlap [70], quenching is not as effective as for the emission coupling, resulting in significant UC enhancement. Our results show that the LSPR peak wavelength deviation significantly affects the enhancement factor of the UCNP luminescence and, as a result, plasmonic nanoparticles with even small spectral variations are required to be precisely controlled for reliable investigation and practical applications.

Consequently, the excitation resonance coupling displayed up to a 3.26-fold enhancement of the intensity while the emission resonance coupling resulted in a slight quenching of the UCNP intensity. Our method could provide a convenient strategy for massive data collection involving plasmonic nanoparticles in a single nanoparticle level. Further, our strategy may provide a guideline for single-nanoparticle investigations involving plasmonic nanoparticles that essentially include plasmonic variations inevitably occurring between individual nanoparticles in practical synthesis techniques.

Work presented in this section has been published in: " Systematic Investigation of the Wavelength-Dependent Upconversion Enhancement Induced by Single Plasmonic Nanoparticles", *Journal of Physical Chemistry C*, 122 (24), 13047–13053 (2018).

1.3 Host engineering: breaking local symmetry

Because the intrinsic optical properties of lanthanides are determined by the non-centrosymmetric crystal-field interaction with host ions at an atomic level, host engineering is the most fundamental approach than the other strategies [1,2,72]. In quantum mechanics, the optical phenomena, i.e. electronic transition between energy levels, occurs through operators that link the initial and final quantum state of electron. Specifically, electric dipole (ED) operator requires opposite parity state after transition; in contrast, magnetic dipole (MD) and electric quadrupole (EQ) operators require same parity after transition. Under these constraints (called as Laporte's selection rule), 4f-4f intra-shell ED transitions should be forbidden because the initial and the final parity state of the electrons doesn't change after transition [5]. However, in real world, 4f-4f ED transitions are commonly observed in Ln^{3+} compounds because of the crystal-field perturbation induced by host ions or ligands [73]. In general, this perturbation effect becomes stronger when the crystal-field is exerted to Ln^{3+} in non-centrosymmetric way. Based on this consideration, the great effort was dedicated to discovering the most efficient upconversion host material. Currently, the majority of upconversion study was demonstrated by hexagonal (β)- NaYF_4 because of relatively high upconversion efficiency than the others (which mainly originating from its lower local symmetry), excellent stability and easy chemistry for nanoparticle synthesis. However,

the upconversion efficiency of this material is still inferior to semiconductors, fluorescent dyes or quantum dots [11]. Therefore, to further enhance the efficiency, various strategies have been demonstrated in terms of doping impurities [74-76], exerting external electric field [77] or mechanical strain [78] by means of breaking the local symmetry (Figure 1.15). Despite the great progress, the ordering nature of inorganic species, in other words, the short-range (1st coordination) order inherited in conventional crystal and glass materials, still constrains the boundary of host engineering.

1.4 Thesis outline

The goal of this thesis is to develop a new class of upconversion host material that overcomes the limitations of the conventional approaches. There are two issues to breakdown the short-range order of inorganic species; (1) the powerful heating method to immediately reach the high melting temperature (over several hundred degree of Celsius), (2) the effective amorphization scheme to prevent recrystallization upon quenching. To accomplish the goal, a crumb of Ln^{3+} -doped $\beta\text{-NaYF}_4$ upconversion nanoparticles were fully liquefied by highly focused laser beam and rapidly quenched by direct contact of metallic substrate. To facilitate the complete amorphization, SiO_2 was introduced as a phase stabilizer during the melting process and the chemical and structural homogeneity was confirmed by

transmission electron microscopy techniques. Chapter 2 covers the fabrication, the investigation of the microstructure, the upconversion properties and its detailed mechanism. To pave the way for practical applications, the developed material was tested as a laser gain medium. By virtue of the surface tension during the melting process, the material was easily polished into smooth microspheres which can serve as a whispering-gallery-mode resonator. Consequently, the upconversion lasing threshold for continuous-wave operation was found to be significantly lower than the previous works and the detailed principles are presented in Chapter 3. The conclusions and outlook of this thesis are summarized in Chapter 4.

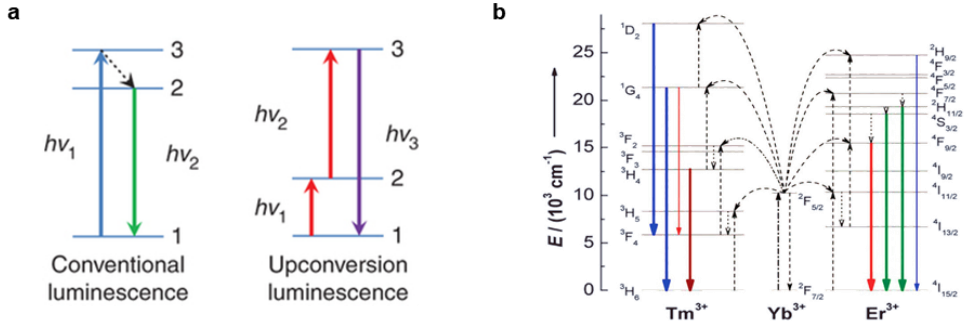


Figure 1.1. (a) Comparison of conventional luminescence and upconversion luminescence [79]. (b) Energy transfer upconversion of Tm³⁺ (Er³⁺) and Yb³⁺ co-doped system [8].

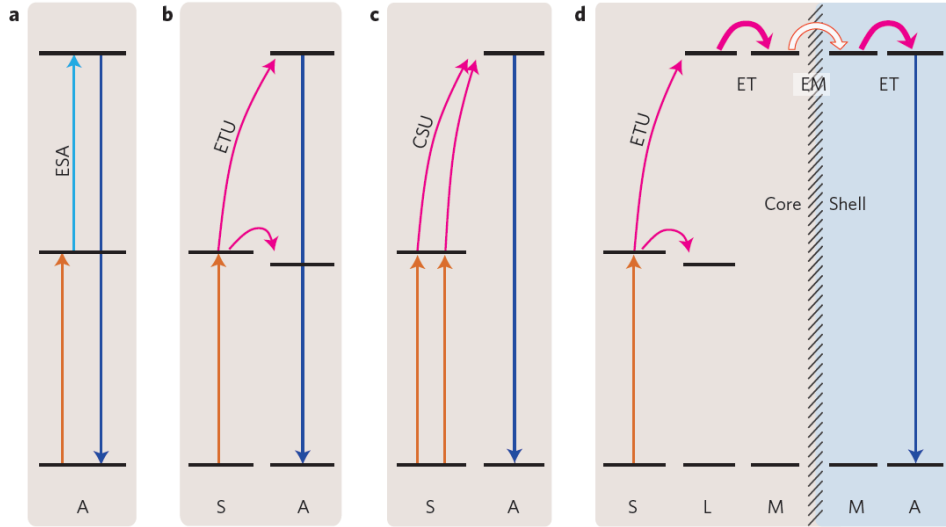


Figure 1.2. Schematic representation of upconversion mechanism [80]. (a) Excited state absorption (ESA). (b) Energy transfer upconversion (ETU). (c) Cooperative sensitization upconversion (CSU). (d) Energy migration upconversion (EMU). A: activator ion, S: sensitizer ion, L: ladder ion and M: migratory ion.

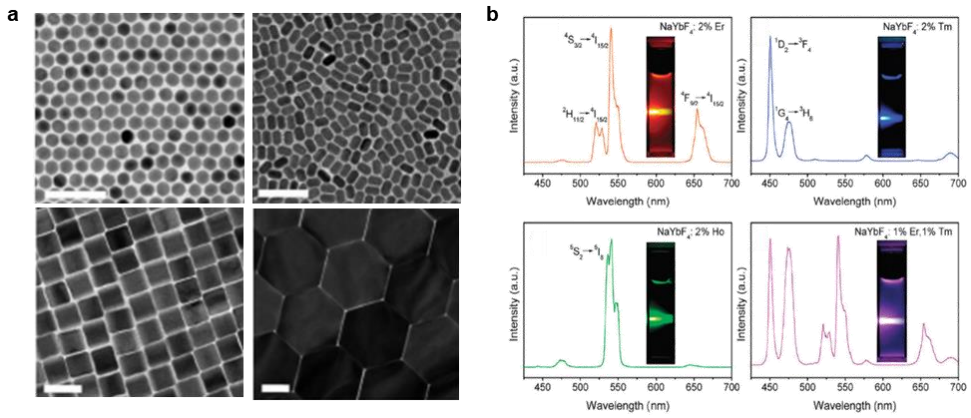


Figure 1.3. (a) Microscopic upconversion materials with various shape and size [81]. (b) Upconversion emission spectra with various dopants [1].

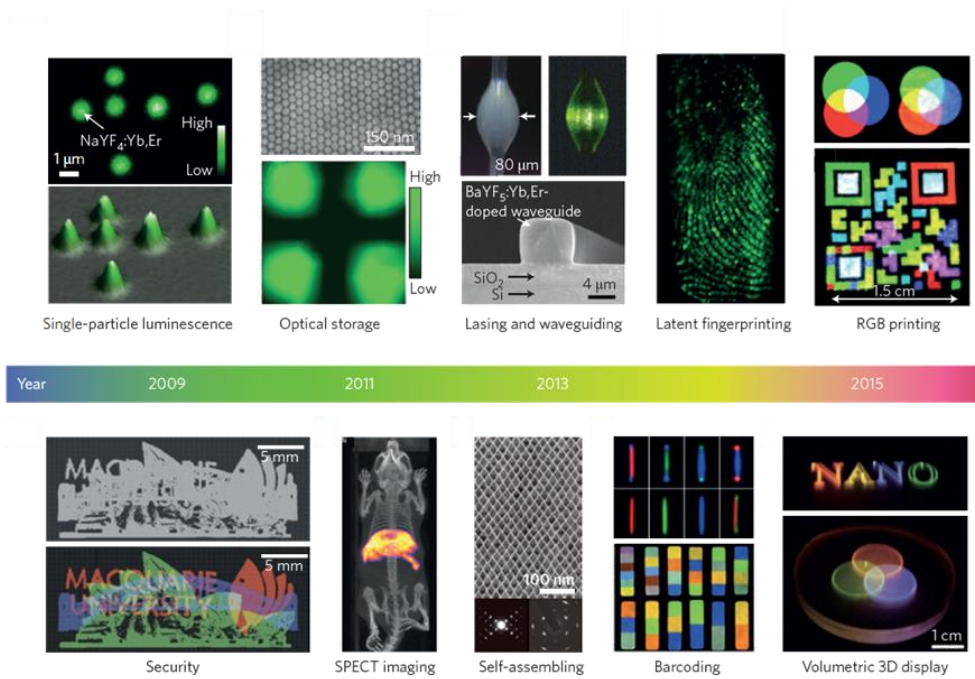


Figure 1.4. Examples of emerging applications of microscopic upconversion materials [80].

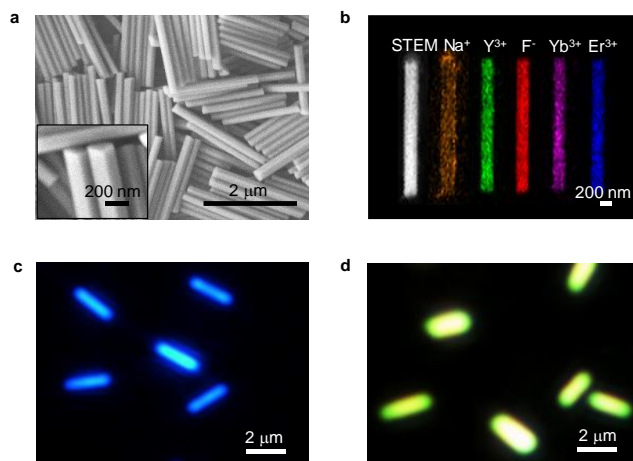


Figure 1.5. (a) SEM image of $\text{NaYF}_4:\text{Yb}^{3+},\text{Tm}^{3+}$ nanocrystal. Inset shows the magnified view. (b) Element mapping of $\text{NaYF}_4:\text{Yb}^{3+},\text{Er}^{3+}$ nanocrystal. (c)-(d) Optical images of $\text{NaYF}_4:\text{Yb}^{3+},\text{Tm}^{3+}$ nanocrystal and $\text{NaYF}_4:\text{Yb}^{3+},\text{Er}^{3+}$ nanocrystal subjected to 980-nm excitation, respectively.

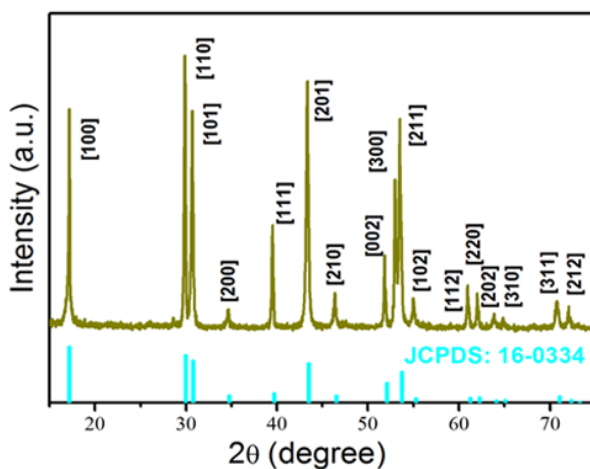


Figure 1.6. XRD pattern of $\text{NaYF}_4:\text{RE}$ nanowire powder and standard card of β - NaYF_4 .

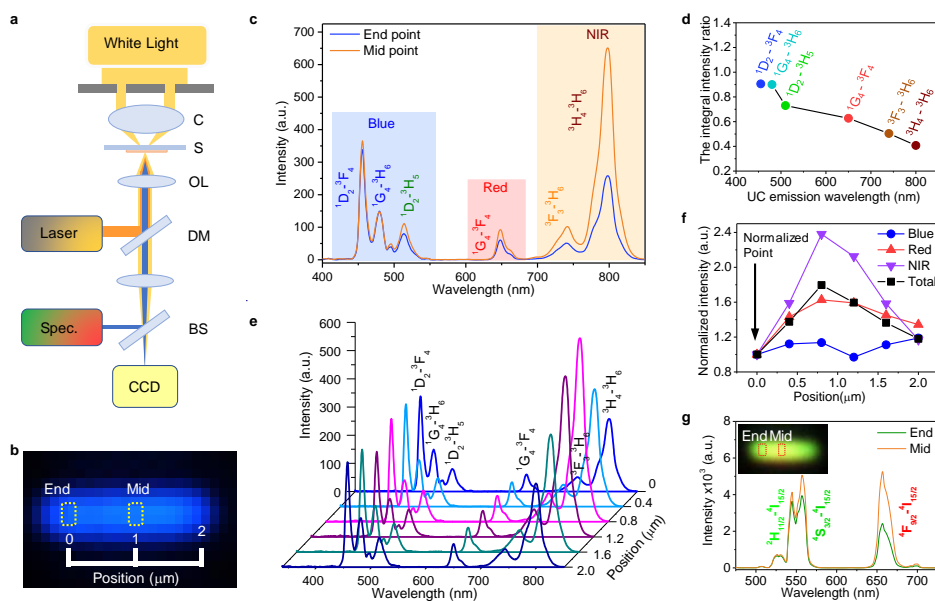


Figure 1.7. (a) Optical pathway of dark-field microscope equipped for UCL measurement. (b) Optical image of individual NaYF₄:Yb³⁺,Tm³⁺ nanocrystal excited by 980-nm laser. The yellow regions are where the emission spectra are acquired (250 nm × 400 nm). (c) UCL spectra emitted from end and middle of single NaYF₄:Yb³⁺,Tm³⁺ nanocrystal. (d) Integral UCL intensity ratio between end and the midpoints for different emission wavelengths. (e) UCL spectra at different positions of single NaYF₄:Yb³⁺, Tm³⁺ nanocrystal. (f) Normalized integral UCL intensity for blue, red, NIR, and total emission (as defined in c) at different nanocrystal positions. (g) Optical image of NaYF₄:Yb³⁺,Er³⁺ nanocrystal and UCL spectra at end and midpoint of nanocrystal.

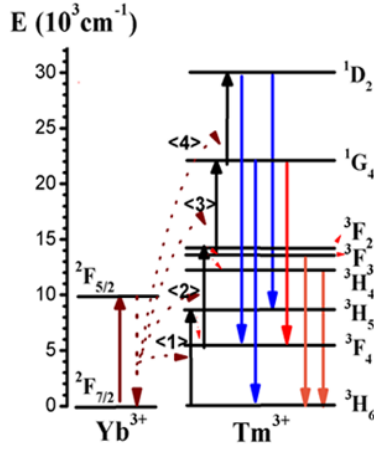


Figure 1.8. Upconversion emission process of Yb³⁺, Tm³⁺ co-doped NaYF₄.

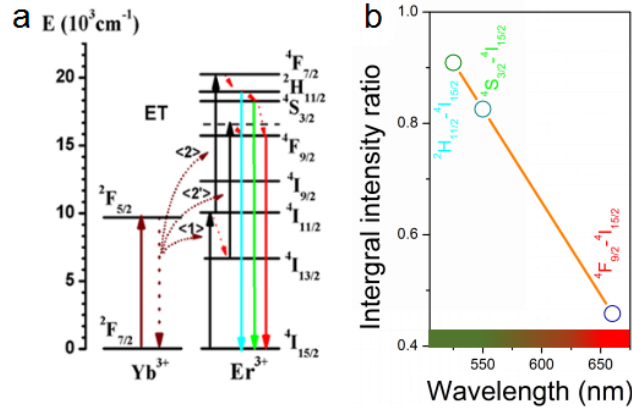


Figure 1.9. (a) Schematic of UC populating mechanism for NaYF₄:Yb³⁺,Er³⁺.

(b) Integral UCL intensity ratio between the end and the middle point at different emission wavelengths in a single NaYF₄:Yb³⁺,Er³⁺ nanowire subject to 980-nm excitation. Note the multiband emissions of Yb³⁺,Er³⁺ ion-doped NaYF₄, assigned to ²H₁₁/₂→⁴I₁₅/₂ at 525 nm, ⁴S₃/₂→⁴I₁₅/₂ at 550 nm and ⁴F₉/₂→⁴I₁₅/₂ at 660 nm, respectively. The corresponding UC populating

mechanism is shown in Fig. S3(a). Interestingly, compared with the end and middle emissions of a single $\text{NaYF}_4:\text{Yb}^{3+},\text{Er}^{3+}$ nanowire, the long-wavelength emissions in the middle of the nanowire are enhanced in a wavelength-dependent manner.

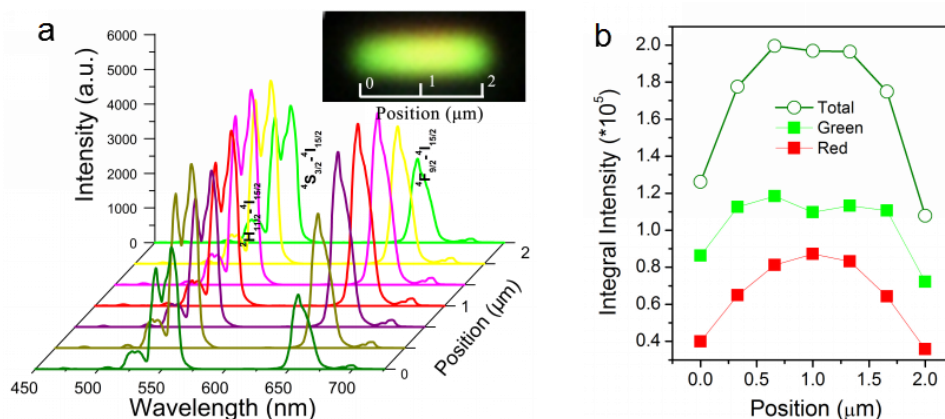


Figure 1.10. (a) Upconversion luminescence spectra at different points in a single $\text{NaYF}_4:\text{Yb}^{3+},\text{Er}^{3+}$ nanowire subject to 980-nm illumination. (b) Integral intensity of green emissions ($^2\text{H}_{11/2}, ^4\text{S}_{3/2}-^4\text{I}_{15/2}$), red emissions ($^4\text{F}_{9/2}-^4\text{I}_{15/2}$), and total emissions at the different positions in the $\text{NaYF}_4:\text{Yb}^{3+},\text{Er}^{3+}$ nanowire.

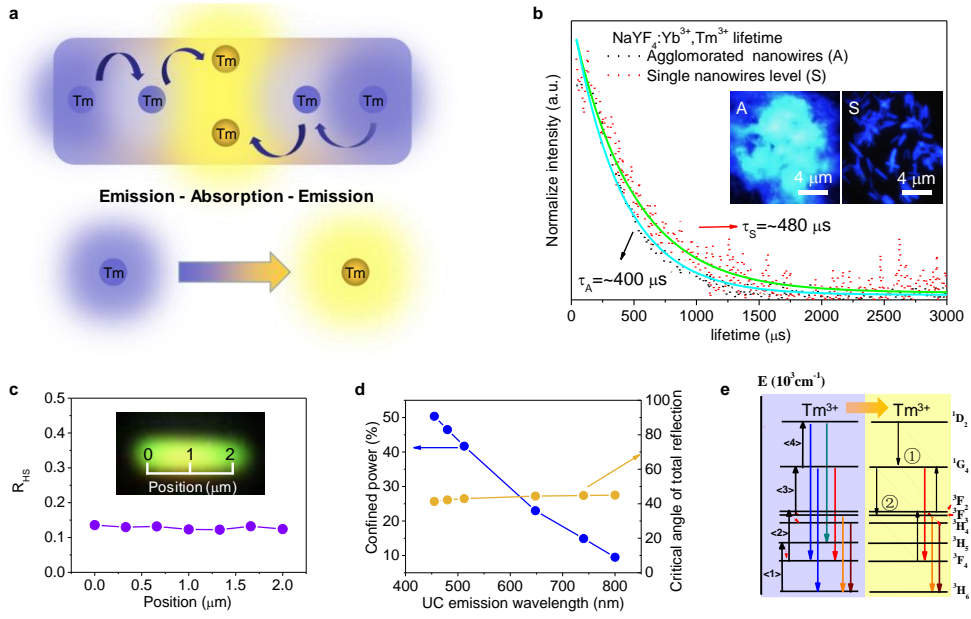


Figure 1.11. (a) Proposed UC multicolor emissions in single NaYF₄:Yb³⁺,Tm³⁺ nanocrystal. (b) Optical images and lifetime curves (blue emissions) of agglomerated and monodispersed NaYF₄:Yb³⁺,Tm³⁺ nanocrystals, respectively. (c) $^2H_{11/2}$ - $^4I_{15/2}$ emission/ $^4S_{3/2}$ - $^4I_{15/2}$ emission ratio (R_{HS}) at different positions in a single NaYF₄:Yb³⁺,Er³⁺ nanocrystal subject to 980-nm excitation. (d) Calculated confined power and critical angle for total internal reflection at different UC emission wavelengths in single NaYF₄:Yb³⁺,Tm³⁺ nanocrystals. (e) Proposed populating mechanism in single NaYF₄:Yb³⁺,Tm³⁺ nanocrystal subject to 980-nm excitation.

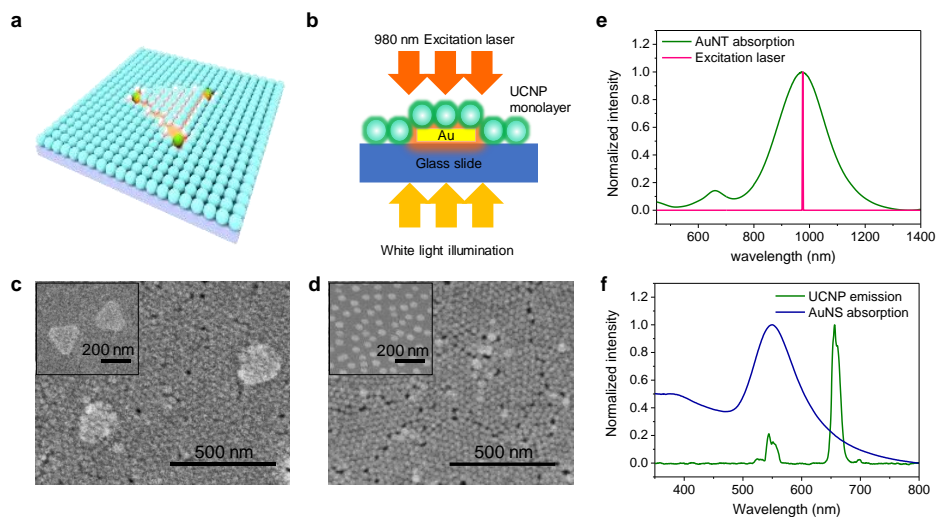


Figure 1.12. Experimental setup and sample characterization. a-b. Experimental setup (a) and investigation scheme (b) of the UCNP monolayer coupled with a gold plasmonic nanoparticle. c-d. SEM images of the UCNP monolayer coupled with AuNTs (c) and AuNSs (d). (Inset: SEM images of synthesized AuNTs and AuNSs.) e-f. UV-Vis/NIR spectra of AuNTs matched with the UCNP excitation wavelength (e) and AuNSs matched with the UCNP emission wavelength (f).

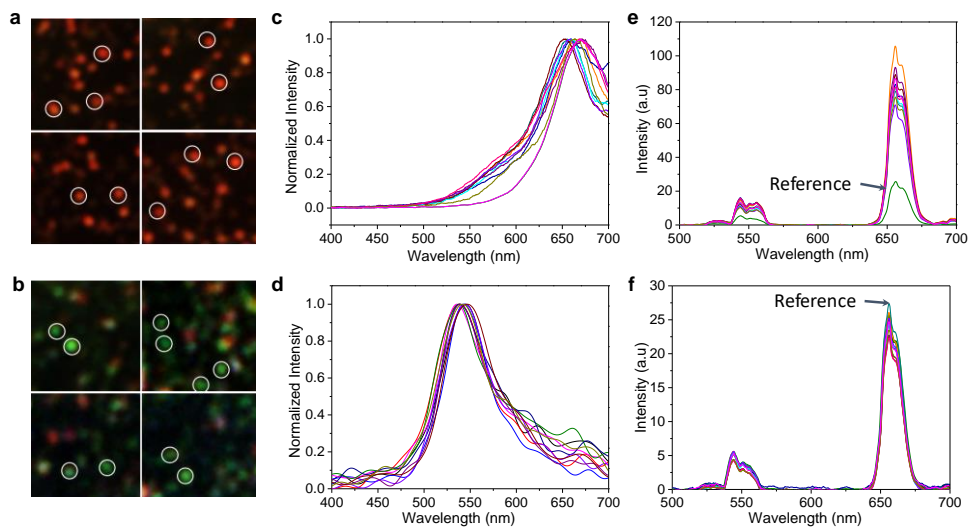


Figure 1.13. Dark-field image of AuNT (a) and AuNS (b) coupled with the UCNP monolayer. c-d, Scattering spectra of selected AuNTs (c) and AuNSs (d) identified by white circles in (a) and (b), respectively. e-f, luminescence spectra of a UCNP monolayer coupled with AuNTs (e) and AuNSs (f). The green curves show the reference spectra and the inset in (f) shows a magnified view of spectrum at 656 nm.

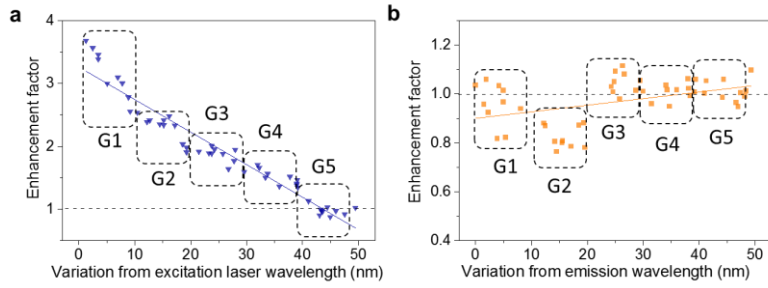


Figure 1.14. Enhancement factors of the intensity for the excitation coupling (a) and the emission coupling (b) depending on the LSPR peak wavelength variation from the excitation and emission wavelengths (groups 1 to 5).

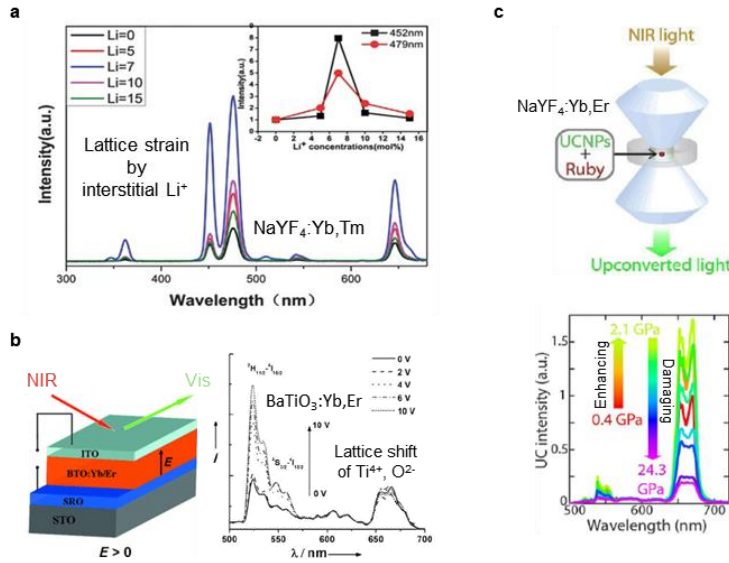


Figure 1.15. Upconversion host engineering based on breaking local symmetry. (a) Upconversion enhancement by interstitial Li⁺ ion doping [76]. (b) External electric field induced upconversion enhancement [77]. (c) Mechanical strain induced upconversion enhancement [78].

Chapter 2

Ultrafast single-band upconversion luminescence in a liquid-quenched amorphous host matrix

2.1 Introduction

Lanthanide (Ln^{3+})-doped upconversion materials converting sequentially absorbed low-energy photons into a higher-energy photon have advanced dramatically over the past half-century because of their excellent photostability, sharp linewidth with fixed spectral positions and low-threshold pumping power [1,82]. In particular, the unique use of near-infrared (NIR) photons in visible-light applications has given birth to emerging research fields such as deep-tissue bioimaging [83], energy harvesters for solar cells [8] and volumetric 3D displays [9]. However, the use of upconversion materials for practical applications demands exquisite control of the upconversion spectra and efficient energy conversion [4]. Because the upconversion of Ln^{3+} generally provides multiband emission originating from its abundant 4f intermediate states [83], one of the long-standing issues in exploiting upconversion luminescence is to achieve efficient single-band emission [1,2,7,14,84] for applications where the crosstalk of individual color units must be avoided [84], such as multiplexed molecular imaging [85], color displays [9] and security coding [86]. In addition, given that multiband emission causes distribution of the available energy into several frequencies, single-band emission is preferred when high conversion efficiency of a photonic device is required, such as in non-linear photonic devices [80].

One strategy to obtain single-band emission of upconversion is to

filter out unwanted spectral bands using fluorescence-absorbing dyes [85] or the surface quenching effect [87]. Although this approach is straightforward and applicable to various systems, the upconversion efficiency appears to be inferior to that of multiband emission because of the considerable energy loss of the filtered emission band. Thus, for high upconversion efficiency, the concentration of upconversion pathways on a specific spectral band through non-radiative energy transfers, such as cross-relaxation [88-90], energy back transfer [91], or transition metal ion mediation [92,93] is preferred. Alternatively, with the assistance of an automated screening system [94], a new combination of multiple Ln^{3+} ions that possesses a unitary upconversion pathway as a result of complex non-radiative energy transfers between dopants was demonstrated. However, the upconversion pathways via various non-radiative energy transfers fatally inherit the dissipative energy loss via phonon relaxation. As a result of the aforementioned limitations, single-band emissions with high upconversion efficiency in comparison with their multiband counterparts have been realized only for the red or NIR region [95].

In this chapter, we report highly efficient green single-band upconversion luminescence of Er^{3+} embedded in a liquid-quenched amorphous matrix. In accordance with the Judd-Ofelt (JO) theory, the single-band upconversion originates from the elevated transition probability of $^2\text{H}_{11/2} \rightarrow ^4\text{I}_{15/2}$ caused by the covalent and asymmetric microenvironment of the

liquid-quenched amorphous matrix. The elevation in the transition probability was validated by the decay time of $^2H_{11/2} \rightarrow ^4I_{15/2}$. Notably, this work is the first report of single-band upconversion demonstrated without the involvement of non-radiative energy transfers via modification of the transition probability, leading to an ultrafast, sub-microsecond decay time, the fastest ever reported [2,5,96]. By adapting an alternative matrix, Y_2O_3 , we also demonstrate that the equivalent single-band upconversion occurs irrespective of the host matrix composition. Furthermore, to elucidate the upconversion pathway of the single-band emission, the power dependence and the temporal behavior of all of the spectral peaks in the visible range are thoroughly investigated. Finally, the possible mechanism of the single-band upconversion in the liquid-quenched amorphous matrix is validated using alternative dopants (Tm^{3+} and Ho^{3+}).

2.2 Materials and methods

Materials: $ErCl_3 \cdot 6H_2O$ (99.9%), $YCl_3 \cdot 6H_2O$ (99.9%), $YbCl_3 \cdot 6H_2O$ (99.9%), $TmCl_3 \cdot 6H_2O$ (99.9%), $HoCl_3 \cdot 6H_2O$ (99.9%), NaOH (98+%), NH_4F (98+%), 1-octadecene (ODE) (90%), oleic acid (OA) (90%), Igepal CO-520, $NH_3 \cdot H_2O$ (30 wt%), and tetraethyl orthosilicate (TEOS) (99.0+%) were purchased from Sigma-Aldrich. All chemicals were used as received without further purification.

Synthesis of nanocrystals: Lanthanide-doped hexagonal (β)-NaYF₄ upconversion nanocrystals and SiO₂-coated nanocrystals were synthesized following the methods of reference [97]. To synthesize upconversion nanocrystals, YCl₃·6H₂O (236.6 mg, 0.78 mmol), YbCl₃·6H₂O (77.498 mg, 0.2 mmol) and ErCl₃·6H₂O (7.634 mg, 0.02 mmol) were added to a 250-ml flask containing 15 ml of ODE and 6 ml of OA. The mixture was vigorously stirred using a glass-coated stirrer and heated at 160 °C for 1 h under an Ar atmosphere to remove H₂O and O₂ before being cooled to 25 °C; the mixture at this stage was yellowish and transparent. Next, 10 ml of methanol containing NH₄F (0.1482 g, 4 mmol) and NaOH (0.1 g, 2.5 mmol) was added dropwise in the prepared solution and the resulting white opaque mixture was then stirred another 30 min. To remove the methanol, the solution was heated at 120 °C for 1 h, followed by heating to 320 °C to induce nucleation and growth of nanocrystals. After cooling, the nanocrystals were collected by centrifugation, re-dispersed in cyclohexane, and then washed twice with copious amounts of ethanol. Finally, the synthesized nanocrystals (1 mmol) were stored in 10 ml of cyclohexane before use. To coat an SiO₂ thin layer onto the nanocrystals, 0.5 ml of Igepal CO-520, 9.6 ml of cyclohexane and 0.4 ml of prepared β -NaYF₄ nanocrystal solution were mixed in a 20-ml glass vial and then stirred for 30 min before 0.08 ml of NH₃·H₂O was added. After 0.04 ml of TEOS was injected quickly into the solution, the container was

sealed hermetically and stirred at 900 rpm for 24 h. β -NaYF₄@SiO₂ nanoparticles were precipitated by adding methanol, re-dispersed in ethanol, washed with excessive cyclohexane three times, and then stored in 10 ml of DI water.

Optical setup and characterization: An inverted optical microscope (Olympus, IX73) was equipped with a single-mode 980 nm diode laser (RGB photonics, Lambda beam PB 980-250 mW). The samples were observed using an oil-type 100 \times objective, and the same objective lens was simultaneously used to obtain the focused laser spot (2 μ m \times 4 μ m) with a power density ranging from 1.25×10^4 to 3×10^6 W cm⁻² on the sample. A spectrograph (Andor, Shamrock 303i) with a 1200 lines/mm grating (500 nm centered) and an EMCCD (Andor, DU970P) were used for spectral analysis over the full visible range from 380 to 720 nm. Subsequently, a narrow spectral range (\sim 5 nm) of the grated spectrum was selected by an external slit for accurate temporal behavior measurement of each transition. An arbitrary function generator (Rigol, DG4102) and an oscilloscope (Rigol, DS2102A-S) equipped with a Si-APD (Thorlabs, APD410A/M) were synchronized before the measurement. All of the aforementioned components of the optical setup are detailed in the scheme in Figure 2.1. Rise and decay curves were fitted with double-exponential functions to calculate the rise and decay times using the equation $y = y_0 + A_1 \exp^{-(x-x_0)/t_1} + A_2 \exp^{-(x-x_0)/t_2}$. In this study, of

the two terms, only the dominant lifetime (τ_1) was compared for the temporal behavior investigation.

Synthesis of liquid-quenched amorphous matrix: Forty microliters of β -NaYF₄@SiO₂ nanoparticles in DI water were deposited onto a Si wafer and then simply dried at 65 °C. The fully dried sample was then heat-treated in a tube furnace at 250 °C for 12 h under low vacuum of 7.0×10^{-2} Torr to prevent undesirable oxidation. After naturally cooling, the prepared sample was moved to a finder grid (Ted Pella, Ni grid, G400F1-N3) through simple rubbing. The attached sample was in the form of crumbs (see details in Figure 2.2). These pretreatments were performed to promote the laser melting process. Next, the heat was induced by laser irradiation to liquefy the precursors; the molten material was then spontaneously quenched by the removal of the surface effect. The liquid-quenching process was initiated and terminated instantly under a maximum power of the focused laser spot (under a 980 nm CW laser of 3×10^6 W cm⁻²).

TEM cross-sectional imaging, SAED and EDS analyses: As-synthesized A-NaYF₄:SiO₂ was easily located by the coordination of the finder grid. The cross-sectional sample of the thin film was prepared by FIB milling (JEOL, JIB-4601F, Ga ion source) for HRTEM images (JEOL, JEM ARM 200F), SAED and EDS analyses.

2.3 Laser-induced liquid-quenching of upconversion nanoparticles

As stated in the Lindemann criterion [98], nanocrystals exhibit a lower melting temperature than their corresponding bulk state by promoting surface liquefaction. Furthermore, the large surface area of the nanocrystals accommodates an effective barrier that prevents heat diffusion by confining phonon propagation at the surface [99], resulting in rapid heat accumulation. Given such unique thermal properties of nanocrystals, we found that upconversion nanocrystals could be melted by the heat generated by the non-radiative relaxation during the upconversion process [99] under brief irradiation with a 980 nm continuous-wave (CW) laser. Upon melting, the liquefied upconversion nanocrystals are monolithically integrated and immediately quenched because of the extinction of the nanocrystals' surface effects. This liquid-quenching process is effectively performed when the upconversion nanocrystals are deposited onto a substrate in the form of crumbs smaller than a few micrometers in diameter, comparable to the size of the focused laser spot of approximately $2\ \mu\text{m} \times 4\ \mu\text{m}$. Note that the laser-induced melting of upconversion nanoparticles wasn't successful when the size of crumb is bigger than the laser spot (Figure 2.3).

Based on this finding, a liquid-quenched amorphous matrix of NaYF_4 (named as A- $\text{NaYF}_4\text{:SiO}_2$) was created by full melting of hexagonal $\beta\text{-NaYF}_4$ nanocrystals coated with a thin SiO_2 layer under irradiation by 980 nm CW

laser (Figure 2.4a). The size of the liquid-quenched sample was mainly determined by the size of the crumb of the deposited upconversion nanocrystals, which ranged from the submicron-scale to several micrometers in diameter (Figure 2.4b). The liquid-quenched matrix was typically integrated into a spherical shape to minimize its surface energy (Figure 2.4c). After the liquid-quenching process, the crystalline β -NaYF₄ nanocrystals coated with an ~8 nm SiO₂ thin layer (Figure 2.4d and e) changed into the liquid-quenched amorphous matrix, as confirmed by TEM cross-sectional images and its halo-like selected-area electron diffraction (SAED) pattern (Figure 2.4f and g). To prevent recrystallization of the liquefied matrix, SiO₂, a well-known network former [100], was introduced as an amorphous phase stabilizer into the β -NaYF₄ nanocrystals (Figure 2.5). This step was necessary because the liquid-quenched NaYF₄ without SiO₂ tended to form a semi-crystalline microstructure via spontaneous recrystallization during the quenching process [101], resulting in an insufficient change in the upconversion spectrum (Figure 2.6). The incorporation of SiO₂ into the liquid-quenched matrix of NaYF₄ resulted in a non-glassy amorphous structure (Figure 2.7) implying strong disorder in a short-range structure (i.e., 1st coordination) [102]. The chemical composition of A-NaYF₄:SiO₂ was confirmed to be homogeneous by TEM-EDS analysis (Figure 2.8).

2.4 Single-band upconversion luminescence at green spectral region

Under irradiation by a 980 nm pump laser with a power density of $3 \times 10^6 \text{ W cm}^{-2}$, A-NaYF₄:SiO₂, Yb³⁺, Er³⁺ (20%, 2%) exhibited an intense green single-band upconversion luminescence, and β -NaYF₄:Yb³⁺, Er³⁺ (20%, 2%) nanocrystals showed a typical multiband upconversion spectrum (Figure 2.4h). In the full visible range, the total summated upconversion emission of A-NaYF₄:SiO₂ was ~45% greater than that of β -NaYF₄ upon normalization by volume (Figure 2.9). In particular, the upconversion emission intensity of the $^2\text{H}_{11/2} \rightarrow ^4\text{I}_{15/2}$ transition (corresponding to 525 nm) in A-NaYF₄:SiO₂ was enhanced by ~16.4 times, resulting in ~87% of the upconversion spectrum residing in the green band. Compared with the yellow-green emission of β -NaYF₄, the pure-green emission of A-NaYF₄:SiO₂ was observed under equivalent pump power density (insets of Figure 2.4b and 2.4c). The possibility of a new intermediate energy state arising from the SiO₂ component in the electron transition can be simply excluded because of its large band gap energy of ~9 eV. Its exclusion is also confirmed by the fact that, even in the absence of SiO₂, the liquid-quenched semi-crystalline NaYF₄ exhibits a substantial increase in intensity of the $^2\text{H}_{11/2} \rightarrow ^4\text{I}_{15/2}$ emission (Figure 2.6). Therefore, this dramatic spectral change of the upconversion nanocrystals from multi- to single-band is mainly attributed to the microstructural change of the host matrix from a crystalline to an amorphous

matrix.

We further investigated $\text{Y}_2\text{O}_3:\text{SiO}_2$ as an alternative host matrix. After the liquid-quenching process, the equivalent green single-band upconversion emission was also observed in the liquid-quenched $\text{Y}_2\text{O}_3:\text{SiO}_2$ (Figure 2.10), implying that the origin of the single-band upconversion lies in the structural configurations of the liquid-quenched amorphous matrix, not in the host material's composition.

2.5 Theoretical interpretation: Judd-Ofelt theory

2.5.1 Judd-Ofelt theory and optical properties of lanthanides

Luminescence spectra of trivalent lanthanide ions (Ln^{3+}) are determined by their 4f-4f or 4f-5d electronic transitions. In particular, because of their abundant 4f inner-shell energy states, the wavelength of emission can cover the whole optical range, spanning from the UV to the visible and NIR regions [5]. In most cases, Ln^{3+} are utilized as a dopant ion embedded in a host matrix because the host ions can provide non-centrosymmetric crystal fields to the emissive centers. As a result, the 4f orbital perturbation by the crystal fields generates exceptional mixed parity states, leading to partially allowed 4f-4f electric dipole (ED) transitions, which are naturally forbidden by quantum selection rules (forbidding parity conservation) [73]. That is, Ln^{3+}

as a free-ion state cannot emit photons corresponding to 4f-4f ED transitions according to quantum theory. Accordingly, the upconversion emission spectra of Ln^{3+} are highly sensitive to the local environment of the emissive center, namely, the crystal field of the host ions [103]. Nevertheless, the sharp spectral lines of Ln^{3+} are well preserved and are similar to a free-ion state because of the shielding effect of the outer shells [73]. This protective nature of the 4f orbitals enables highly useful approximations in which a doped Ln^{3+} is considered to act as a free ion surrounded by a static electric field of the host ion. On the basis of these approximations, Judd-Ofelt (JO) theory was developed to explain the absorption and emission spectra of Ln^{3+} and has been demonstrated to successfully predict experimental data within reasonable errors [104-106]. In accordance with the JO theory [104,105], the spectral intensities and ratios of 4f transitions are mainly governed by the product of host-dependent JO parameters ($\Omega_{\lambda=2,4,6}$) and host-independent reduced matrix elements ($U_{\lambda=2,4,6}$) [107]. Therefore, absorption and luminescence spectra, radiative lifetimes, transition probabilities and quantum efficiencies of Ln^{3+} embedded in a host matrix are readily predicted using JO parameters [106].

Despite the (JO) theory being a well-developed guide for predicting the optical properties of Ln^{3+} , the absolute JO parameters of small-sized samples, such as nanoparticles or microparticles, are hardly measured because of the difficulty in obtaining the quantitative absorption spectra that

are necessary to calculate the JO parameters [108]. As an alternative to the absorption spectra, the diffuse-reflectance spectra were combined with the emission branch ratios to derive the absolute JO parameters of the micro-sized sample; however, this approach still requires a sufficient volume of measured sample [109].

In contrast, the relative JO parameters are well known to be derived much more easily than the absolute JO parameters by simply using the emission spectra. Even though the relative values are insufficient to elucidate all the spectral properties of Ln^{3+} embedded in the host material's crystal field [110], in the present study, we found that the relative values of the JO parameters provide important information about the origin of the single-band upconversion emission in the liquid-quenched amorphous matrix via the ratio of each radiative transition possibility. Using the upconversion spectra, the relative JO parameters ($\Omega_{\lambda=2,4,6}^r$, $\Sigma\Omega_{\lambda}^r = 1$) of Er^{3+} embedded in A- $\text{NaYF}_4\text{:SiO}_2$ were investigated.

2.5.2. Calculating the relative Judd-Ofelt parameters

The relative JO parameters of the liquid-quenched amorphous $\text{NaYF}_4\text{:SiO}_2$, Yb^{3+} , Er^{3+} (A- $\text{NaYF}_4\text{:SiO}_2$, Yb^{3+} , Er^{3+}) were calculated using the upconversion emission spectrum according to the estimation method

described in previous literature reports [109]. The Einstein A coefficient ($A_{JJ'}$) for spontaneous emissions provides direct information about the spectral intensities and the ratios of Ln^{3+} ions and is mainly determined by a summation of the electrical dipole (ED) and the magnetic dipole (MD) transition ($J \rightarrow J'$) probabilities. However, because the MD transition is normally negligible in an upconversion process (a small fraction, less than 5% of the total emission [111]), the effect of the host matrix on Er^{3+} was simply estimated on the basis of the changes of the electric dipole transition possibilities (A_{ED}).

In the Judd-Ofelt (JO) theory [104,105], A_{ED} is mainly governed by the product of highly host-dependent JO parameters ($\Omega_{\lambda=2,4,6}$) and host-independent reduced matrix elements ($U_{\lambda=2,4,6}$) [107]. Therefore, the transition probability of the $J \rightarrow J'$ transition is expressed as

$$A_{JJ'} \approx A_{ED} = C(\nu^3) [(\Omega_2 \times U_2) + (\Omega_4 \times U_4) + (\Omega_6 \times U_6)]$$

where $C(\nu)$ is the physical constant as a linear function of emission frequency to the third power. Using the branch ratio (β), which is proportional to the spontaneous emission probability of each transition, we can derive $A_{JJ'}$ from the integrated intensity (I) of the upconversion emission spectrum as

$$\beta_{JJ'} = \frac{I_{JJ'}}{\sum_K I_{JK}} = \frac{A_{JJ'}}{\sum_K A_{JK}}$$

where the sum runs over all possible final states, K . The absolute JO parameters can be estimated if the complete set of all of the transitions from the equivalent excited state are measured. With the incomplete set of transitions, however, the relationship of each JO parameter can be determined using the simultaneous equation method. Given that the reduced matrix elements of each transition can be found in the literature [111], at least three simultaneous equations for the individual transitions are mathematically required to determine the relationship of four variables: three JO parameters and physical constant C .

In the visible range, only three emission peaks at 408, 555 and 700 nm were available to calculate the branch ratio (β) because they correspond to the radiative transitions from an equivalent state: $^2H_{9/2} \rightarrow ^4I_{15/2}$, $^4I_{13/2}$ and $^4I_{11/2}$, respectively. The measured integrated intensities and reduced matrix elements of these three transitions enabled us to determine the relative JO parameters of A-NaYF₄:SiO₂, Yb³⁺, Er³⁺.

The integrated intensities of each transition were deconvoluted using Gaussian-Lorentzian fitting from the upconversion emission spectrum of A-NaYF₄:SiO₂, Yb³⁺, Er³⁺ (Figure 2.11). The measured integrated intensities of $^2H_{9/2} \rightarrow ^4I_{15/2}$, $^4I_{13/2}$ and $^4I_{11/2}$ were 293, 1400 and 1069 (a.u.), respectively. Using reduced matrix elements of each transition (Table 2.1), we obtain the simultaneous equations as

$${}^2H_{9/2} \rightarrow {}^4I_{15/2}: C \times [24527(cm^{-1})]^3 \times [(0 \times \Omega_2) + (0.078 \times \Omega_4) + (0.17 \times \Omega_6)] = 293 \times R$$

$${}^2H_{9/2} \rightarrow {}^4I_{13/2}: C \times [18046(cm^{-1})]^3 \times [(0.073 \times \Omega_2) + (0.12 \times \Omega_4) + (0.41 \times \Omega_6)] = 1400 \times R$$

$${}^2H_{9/2} \rightarrow {}^4I_{11/2}: C \times [14404(cm^{-1})]^3 \times [(0.077 \times \Omega_2) + (0.11 \times \Omega_4) + (0.096 \times \Omega_6)] = 1069 \times R$$

where $R = \sum_K A_{JK} / \sum_K I_{JK}$, and the constants C and R can be reduced into a single variable. Therefore, the calculated relative JO parameters ($\Omega^r_2, \Omega^r_4, \Omega^r_6, \sum \Omega^r = 1$) of A-NaYF₄:SiO₂, Y³⁺, Er³⁺ were 0.82, 0.9, and 0.9, respectively.

The estimated relative JO parameters (Ω^r_2, Ω^r_4 , and Ω^r_6) were 0.82, 0.09, and 0.09, respectively, for A-NaYF₄:SiO₂, Yb³⁺, Er³⁺ and 0.63, 0.05, 0.32 [109], respectively, for β -NaYF₄:Yb³⁺, Er³⁺ (Figure 2.11). Using the estimated relative JO parameters, we calculated the electric-dipole transition probability (A_{ED}) ratios for the visible Er³⁺ transitions (${}^2H_{9/2} \rightarrow {}^4I_{15/2}$, ${}^4I_{13/2}$, ${}^4I_{11/2}$; ${}^4F_{7/2} \rightarrow {}^4I_{15/2}$; ${}^2H_{11/2} \rightarrow {}^4I_{15/2}$; ${}^4S_{3/2} \rightarrow {}^4I_{15/2}$; and ${}^2F_{9/2} \rightarrow {}^4I_{15/2}$); the results are presented in Figure 2.12a. Although the highest A_{ED} was found in the ${}^2H_{11/2} \rightarrow {}^4I_{15/2}$ transition in both host matrices, the A_{ED} differences between the ${}^2H_{11/2} \rightarrow {}^4I_{15/2}$ transition and the other transitions were much more intense in A-NaYF₄:SiO₂ because ${}^2H_{11/2} \rightarrow {}^4I_{15/2}$ is a well-known “hypersensitive

transition” [112]; it is highly sensitive to changes in the host matrix’s microstructure. Therefore, the ultrafast decay time of $^2H_{11/2} \rightarrow ^4I_{15/2}$ (0.2 μs) uniquely observed in A-NaYF₄:SiO₂ (β -NaYF₄: 171.9 μs) (Figure 2.12b) is apparently attributable to the matchlessly high A_{ED} value of $^2H_{11/2} \rightarrow ^4I_{15/2}$ because the lifetime of an excited state is inversely proportional to the transition probability [73]. Given that the population of the other states generally takes several tens of microseconds [96], compared to the other transitions in A-NaYF₄:SiO₂ (4–7 μs) and β -NaYF₄, Yb³⁺, Er³⁺ (47–390 μs) (see Table 2.2), the ultrafast $^2H_{11/2} \rightarrow ^4I_{15/2}$ transition could effectively prevent the other states from populating by dominating the photon consumption process, leading to the green single-band emission spectrum.

2.5.3 Correlation with host matrix’s microstructure

To further understand the characteristics of the liquid-quenched amorphous matrix, a ternary diagram of the electric-dipole transition probability difference (ΔED) between the 1st and 2nd probable transitions was plotted with the relative values of the JO parameters, as shown in Figure 2.12c. For a rational comparison, the ΔED values were normalized by the summation of all of the transition probabilities. We marked A-NaYF₄:SiO₂, β -NaYF₄ and other host materials reported in the literature [109,113] based

on their estimated relative JO parameters. In the ternary diagram, the drastic increase in ΔE_D is observed under the conditions of $\Omega_2^r \geq 0.75$, representing the disordered host matrix, because the Ω_2 parameter increases with increasing covalency of the chemical bond and the asymmetric crystal field of the 1st coordination host ions [106,114]. Based on this criterion, we conclude that the liquid-quenched amorphous matrix provides an extremely disordered environment, thereby ensuring sufficient short-range disorder [112] to elevate the $^2H_{11/2} \rightarrow ^4I_{15/2}$ transition probability by the same extent as it is elevated by the molten phase.

2.6 Upconversion pathway of liquid-quenched amorphous host matrix

To elucidate the upconversion pathway of the single-band upconversion emission, the power dependence and the temporal behavior of A-NaYF₄:SiO₂ were investigated under pump power densities ranging from 1.25×10^4 W cm⁻² to 3×10^6 Wcm⁻² (Figure 2.13a). Compared with β -NaYF₄ nanocrystals, which experience early saturation of upconversion under a pump power density greater than 10^4 W cm⁻² (Figure 2.14 and 2.15), A-NaYF₄:SiO₂ appears to be much more sensitive to the pump power density. The power dependence of crystalline β -NaYF₄:Yb³⁺, Er³⁺ (20%, 2%) was investigated at various 980 nm pump power densities ranging from 1.25×10^4 W/cm² to 3×10^6 W/cm² for comparison with the power dependence of A-NaYF₄:SiO₂,

Yb³⁺, Er³⁺ (20%, 2%). The upconversion emission peaks of β -NaYF₄:Yb³⁺, Er³⁺ can be classified into two groups: one group is saturated at low power density, and the other is saturated at high power density, which can be easily distinguished by the slope in the double-logarithmic plot (Figure 2.14a). The former exhibiting sufficient emissions under low power density demonstrates the value of the slope of each transition in a double-logarithmic plot near 0.1, confirming that the population of the excited states are extremely saturated [6,115], except for the case of the thermally coupled $^4S_{3/2} \rightarrow ^4I_{15/2}$ and $^2H_{11/2} \rightarrow ^4I_{15/2}$ transitions (0.070 and 0.210) (Figure 2.14b). This saturation behavior might be explained by the high temperature under laser irradiation, as the $^2H_{11/2}$ state is easily populated from $^4S_{3/2}$ via thermal excitation because of their small energy gap ($\sim 800 \text{ cm}^{-1}$) [116]. In contrast, the slope of the latter group is steeper than that of the former group, i.e., the latter group is less saturated (Figure 2.14c), because the corresponding excited states require one more energy transfer step from the former group's excited states (see the Er³⁺ energy levels in Figure 2.15). Consequently, slopes less than 0.5 indicate that the overall excited states of β -NaYF₄:Yb³⁺, Er³⁺ were highly saturated under high pump power density ($>10^4 \text{ W/cm}^2$) because of its relatively long lifetime [117]. The saturated long-lived intermediate states commonly result in a high chance of energy transfer to the other states, eventually resulting in a multiband emission [84].

First, we observed that the single-band upconversion was not achieved under low-power excitation. However, at power densities greater than $7.5 \times 10^4 \text{ W cm}^{-2}$, the intensity of the $^2\text{H}_{11/2} \rightarrow ^4\text{I}_{15/2}$ transition increased faster, with the highest slope of ~ 1.286 , compared with the other upconversion transitions (slopes less than 1.1) in the double-logarithmic plot (Figure 2.13b). This result suggests that the $^2\text{H}_{11/2} \rightarrow ^4\text{I}_{15/2}$ transition has great luminescence capability under high-power excitation because of its elevated transition probability in A-NaYF₄:SiO₂. The slope shift of the $^4\text{F}_{7/2} \rightarrow ^4\text{I}_{15/2}$ emission from 1.09 to 1.971 presumably arises from second harmonic generation (SHG) of Yb³⁺, having a marked threshold power and a slope of ~ 2 .

At high pump power densities greater than $7.5 \times 10^5 \text{ W cm}^{-2}$, a decrease of the slopes was observed for all of the transitions, resulting in negative slopes for all of the transitions, except $^2\text{H}_{11/2} \rightarrow ^4\text{I}_{15/2}$ of Er³⁺ and the SHG of Yb³⁺ (Figure 2.13c). The decrease of the slopes might be due to the temperature quenching effect, which is inevitable in a high-power upconversion process [118]. To explain the moderate quenching of the $^2\text{H}_{11/2} \rightarrow ^4\text{I}_{15/2}$ transition compared with the quenching of the other transitions, we investigated the temporal behavior of thermally coupled $^2\text{H}_{11/2} \rightarrow ^4\text{I}_{15/2}$ and $^4\text{S}_{3/2} \rightarrow ^4\text{I}_{15/2}$ transitions, as shown in Figure 2.13d. Interestingly, at high pump power excitation, we found that the intensity of the $^4\text{S}_{3/2} \rightarrow ^4\text{I}_{15/2}$ transition increased rapidly and subsequently decreased until the steady-state was

reached. We believe that this extraordinary decay curve results from the phonon-assisted population [119] of $^4S_{3/2} \rightarrow ^2H_{11/2}$, which effectively alleviates the quenching of $^2H_{11/2} \rightarrow ^4I_{15/2}$ in A-NaYF₄:SiO₂ because among all of the transitions, it is found only in $^4S_{3/2} \rightarrow ^4I_{15/2}$ (Figure 2.16 and 2.17). Accordingly, the abrupt decrease in the decay time of $^2H_{11/2} \rightarrow ^4I_{15/2}$ also supports the hypothesis of an over-populated excited state [120] of $^2H_{11/2}$ (Figure 2.13e).

We also observed that the intensity difference between the initial rise and the subsequent decay (ΔI) of $^4S_{3/2} \rightarrow ^4I_{15/2}$ was linearly amplified with increasing pump power density (Figure 2.13f), indicating that the phonon-assisted population in A-NaYF₄:SiO₂ was mainly governed by the balance of rate equations [121]. Although the intensity ratio of $^2H_{11/2}$ and $^4S_{3/2} \rightarrow ^4I_{15/2}$ is well known to be determined by the Boltzmann distribution [99], the non-equilibrium dynamics of $^4S_{3/2} \rightarrow ^2H_{11/2}$ is uniquely reported in the present study.

According to the aforementioned findings of the drastic increase in the $^2H_{11/2} \rightarrow ^4I_{15/2}$ transition with increasing pump power and the alleviated quenching of $^2H_{11/2} \rightarrow ^4I_{15/2}$ via the phonon-assisted population of $^4S_{3/2} \rightarrow ^2H_{11/2}$, the intense green single-band upconversion spectrum of A-NaYF₄:SiO₂ could be obtained at the highest pump power density of $3.0 \times 10^6 \text{ W cm}^{-2}$.

2.7 Verification of mechanism with alternative dopants

We also adapted all other popular dopants (Tm^{3+} and Ho^{3+}) to verify the single-band upconversion process in the liquid-quenched amorphous matrix. The single-band emission was also observed in the Tm^{3+} -embedded liquid-quenched amorphous matrix ($\text{A-NaYF}_4\text{:SiO}_2$, Yb^{3+} , Tm^{3+}). The blue emission of $\beta\text{-NaYF}_4\text{:Yb}^{3+}$, Tm^{3+} originated from the $^1\text{D}_2$ state populated by the cross-relaxation of $^1\text{G}_4 + ^3\text{H}_4 \rightarrow ^3\text{F}_4 + ^1\text{D}_2$ instead of the energy transfer from Yb^{3+} [122]. By contrast, in the case of $\text{A-NaYF}_4\text{:SiO}_2$, Yb^{3+} , Tm^{3+} , the most dominant emission was the host sensitive $^1\text{G}_4 \rightarrow ^3\text{H}_6$ transition (Figure 2.18a), which resulted in $\text{A-NaYF}_4\text{:SiO}_2$, Yb^{3+} , Tm^{3+} exhibiting a higher power dependence of upconversion emission and a faster decay time than its crystalline counterpart (Figure 2.18b and c). Although the $^1\text{D}_2 \rightarrow ^3\text{F}_4$ transition is also host sensitive [123], the cross-relaxation was possibly excluded by the photon consumption through the fast radiation of $^1\text{G}_4 \rightarrow ^3\text{H}_6$.

The proposed mechanism that leads to the single-band upconversion in the liquid-quenched amorphous matrix is depicted in Figure 2.18d. The single-band upconversion appears to occur at the radiative transitions sensitive to the host material ($^2\text{H}_{11/2} \rightarrow ^4\text{I}_{15/2}$ of Er^{3+} and $^1\text{G}_4 \rightarrow ^3\text{H}_6$ of Tm^{3+}) because the other radiative transitions are excluded by the monopolistic photon consumption of the host sensitive transitions. Notably, the single-band emission arising from the $^2\text{H}_{11/2} \rightarrow ^4\text{I}_{15/2}$ transition of Er^{3+} is attractive, as it is

a pathway with less energy dissipation and the least non-radiative relaxation, providing an efficient two-photon upconversion pathway. On the other hand, Ho^{3+} did not display single-band upconversion behavior in the liquid-quenched amorphous matrix because of the absence of the host sensitive transition in the two-photon upconversion process [124]; only the intensity ratio in the emission spectrum changed (Figure 2.19). The host sensitive transitions in Ho^{3+} occur only in three-photon upconversion.

2.8 Conclusion

In conclusion, highly efficient and ultrafast green single-band upconversion of Er^{3+} was obtained via the $^2\text{H}_{11/2} \rightarrow ^4\text{I}_{15/2}$ transition in a liquid-quenched amorphous matrix, resulting in minimal energy loss in the two-photon upconversion process. This spectral modulation of the upconversion emission was achieved by direct manipulation of the transition probabilities, which is the primal property of luminophores. The liquid-quenched amorphous matrix proposed in the present study has great potential in future applications, such as photonic integrated circuits, which demand high upconversion efficiency with an exceptionally fast response time; such requirements have not been satisfactorily attained previously. We also believe that the ultrafast decay time of our material will enable the development of

new applications for upconversion materials, e.g., an ultrafast upconversion laser, high-speed IR photon counting, or digital information processing [125].

Work presented in this chapter has been published in: " Ultrafast Single-Band Upconversion Luminescence in a Liquid-Quenched Amorphous Matrix", *Advanced Materials*, 30 (25), 1800008 (2018).

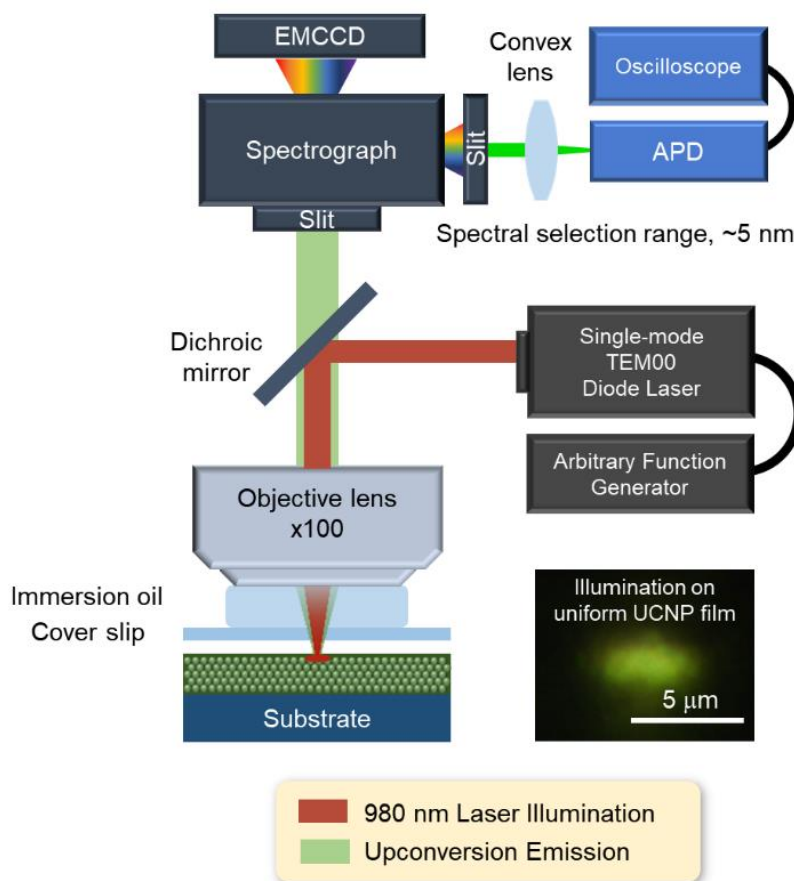


Figure 2.1. Optical setup for laser focusing and spectral and lifetime analyses of upconversion materials.

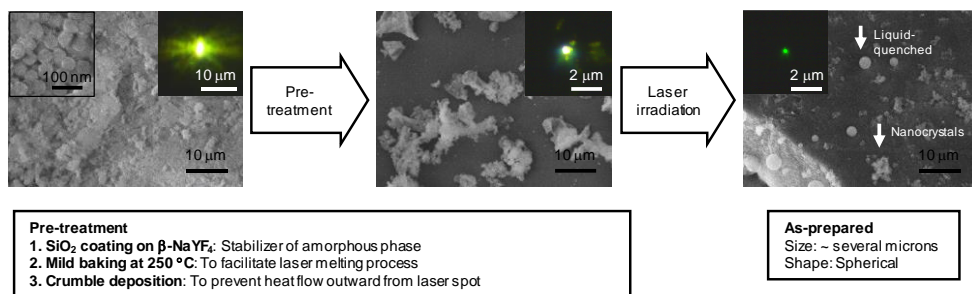


Figure 2.2. Laser-induced full melting and instant quenching process. Highly crystalline $\beta\text{-NaYF}_4$ nanocrystals were used as the initial material. A pretreatment process, as described above, was performed to facilitate the whole process. Only the heat by laser irradiation was used to liquefy the precursors. The molten precursors were then spontaneously quenched by the extinction of the surface effect. The spherical particle shape of the sample indicates that the precursors were fully melted and shaped to minimize their surface energy. The entire process was initiated and terminated under 980 nm CW laser of $3 \times 10^6 \text{ W/cm}^2$.

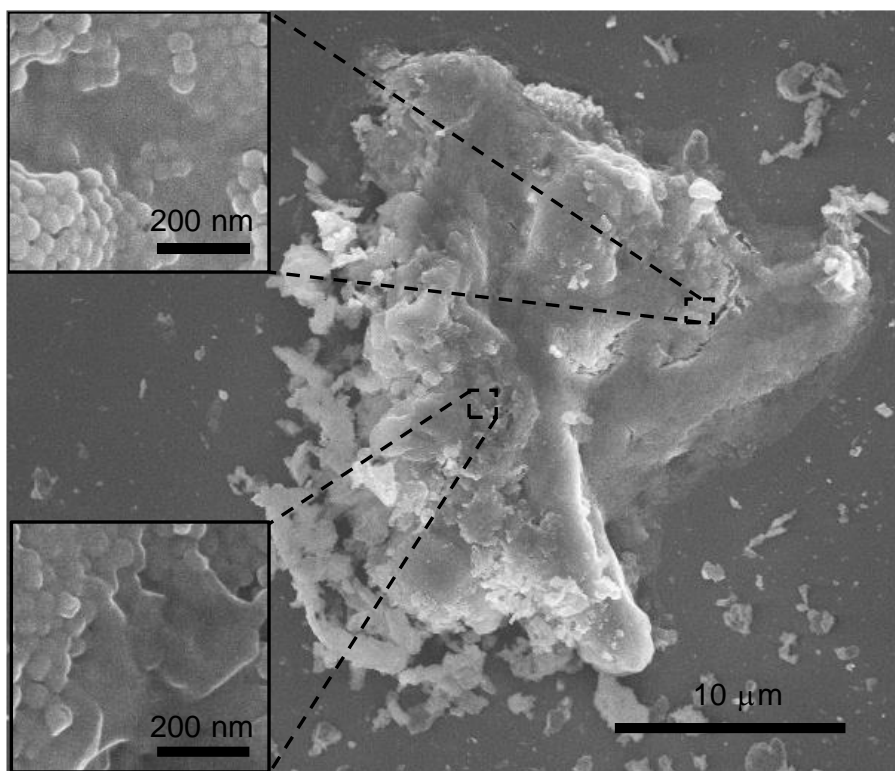


Figure 2.3. Partially melted nanocrystals in a crumb larger than $10\ \mu\text{m}$ during laser irradiation. The temperature of the crumb was elevated via the rapid heat accumulation, which involved a number of nanoparticles in the focusing spot absorbing energy and then dissipating heat into the surroundings. Whereas a small crumb of a few nanoparticles cannot induce adequate heat accumulation, for a large crumb larger than $\sim 10\ \mu\text{m}$, the heat dissipation into the surroundings prevents heat accumulation. As a result, the size of the homogeneous liquid-quenched sample was limited from several hundred nanometers to several microns, which is comparable to the size of the focused laser spot.

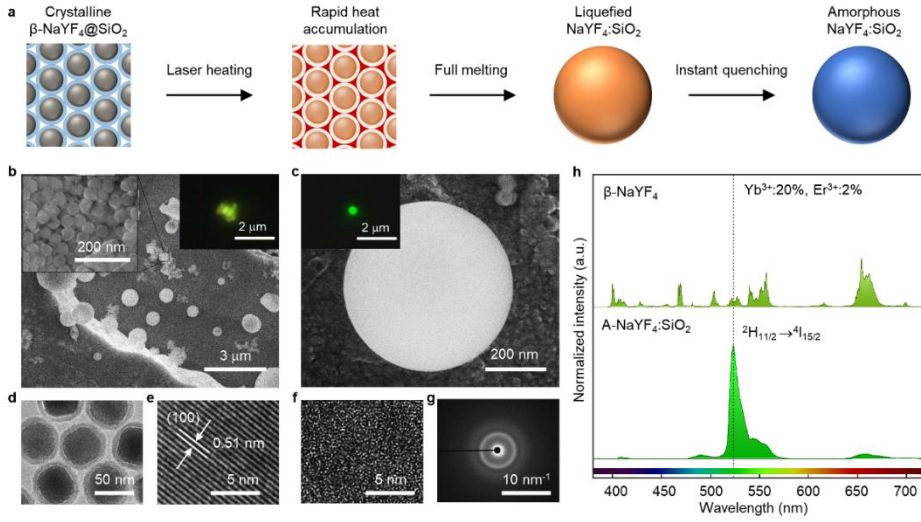


Figure 2.4. Single-band upconversion luminescence of the liquid-quenched amorphous $\text{NaYF}_4:\text{SiO}_2$ co-doped with Er^{3+} and Yb^{3+} : (a) Schematic of the liquid-quenched amorphous $\text{NaYF}_4:\text{SiO}_2$ (A- $\text{NaYF}_4:\text{SiO}_2$) synthesis from crystalline $\beta\text{-NaYF}_4$ nanocrystals coated with a thin SiO_2 layer using laser irradiation. (b-c) SEM images of a crumb of $\beta\text{-NaYF}_4$ nanocrystals and as-synthesized A- $\text{NaYF}_4:\text{SiO}_2$ on the substrate at low (b) and high magnification (c). (Color insets are the color images of typical upconversion emission from $\beta\text{-NaYF}_4$ and A- $\text{NaYF}_4:\text{SiO}_2$). (d-e) TEM images of ~ 45 nm-diameter $\beta\text{-NaYF}_4$ nanocrystals coated with an ~ 8 nm SiO_2 layer (d) and the corresponding lattice structure (e). (f-g) TEM cross-sectional image of A- $\text{NaYF}_4:\text{SiO}_2$ (f) and its halo-like SAED pattern (g). (h) Single-band upconversion emission spectrum of A- $\text{NaYF}_4:\text{SiO}_2$ (20%, 2%) compared with the multiband upconversion of $\beta\text{-NaYF}_4$ (20%, 2%) under 980 nm CW laser irradiation at 3×10^6 W cm^{-2} . The intensity of each spectrum is normalized by volume of the acquired samples.

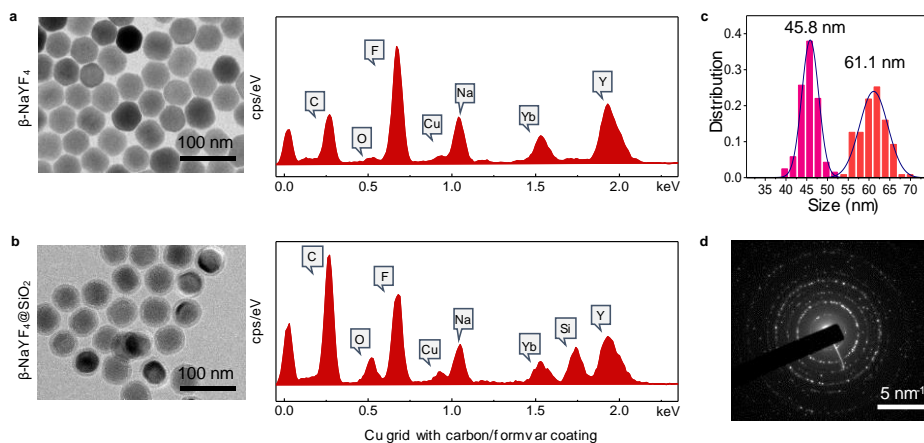


Figure 2.5. The application of an amorphous phase stabilizer: a thin layer of SiO₂ coated onto the β -NaYF₄. a-b, TEM-EDS analysis of β -NaYF₄ (a) and β -NaYF₄@SiO₂ nanocrystals (b). A thin layer of SiO₂ of ~8 nm was introduced and confirmed by TEM observation and EDS analysis. (c), The average size of the synthesized nanocrystals was 45.8 nm, and the SiO₂ layer thickness was ~8 nm. (d), SAED of the β -NaYF₄ nanocrystals. A sharp ring-type diffraction pattern was observed because nanocrystals can be considered as a polycrystalline material.

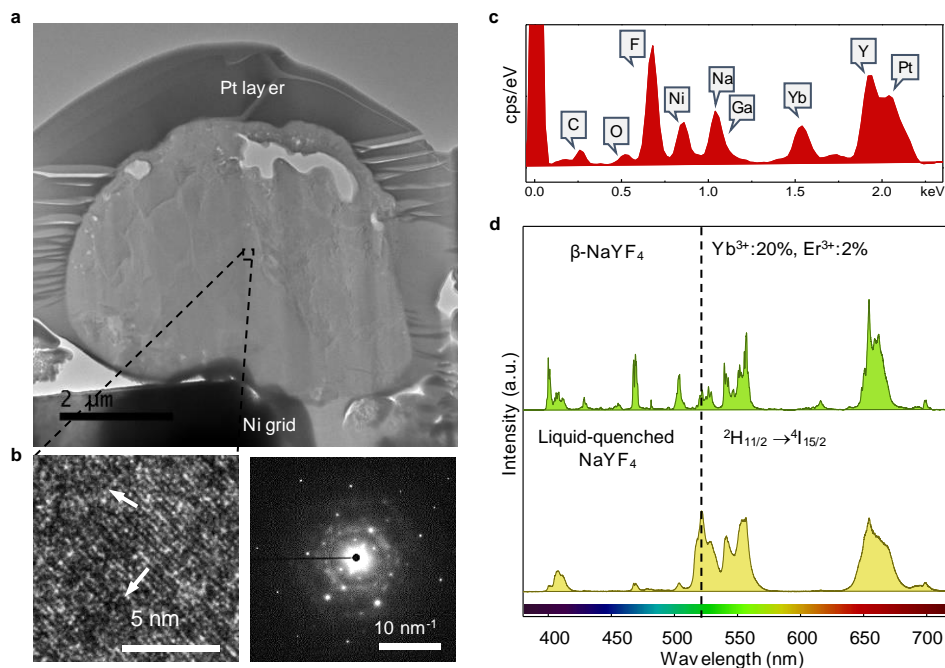


Figure 2.6. Liquid-quenched host materials without SiO₂ stabilizer. a-b, Laser-induced liquid-quenching was applied to β -NaYF₄ without SiO₂ (a); however, without the amorphous phase stabilizer SiO₂, the quenched matrix was semi-crystalline because of spontaneous recrystallization (left side of b, white arrows indicate amorphous regions), as confirmed by the SAED (selected area electron diffraction) patterns (right side of b). c, Chemical composition of the liquid-quenched NaYF₄ was not changed from that of the initial β -NaYF₄ (cf. Figure 2.5a) during the liquid-quenching process, as confirmed by TEM-EDS analysis (Ni, Ga and Pt originated from the sample preparation process). d, Insufficient change in the upconversion spectrum was observed in the liquid-quenched NaYF₄. Notably, because of the amorphous regions, the $^2H_{11/2} \rightarrow ^4I_{15/2}$ transition of the liquid-quenched NaYF₄ was substantially enhanced compared with that of the untreated β -NaYF₄.

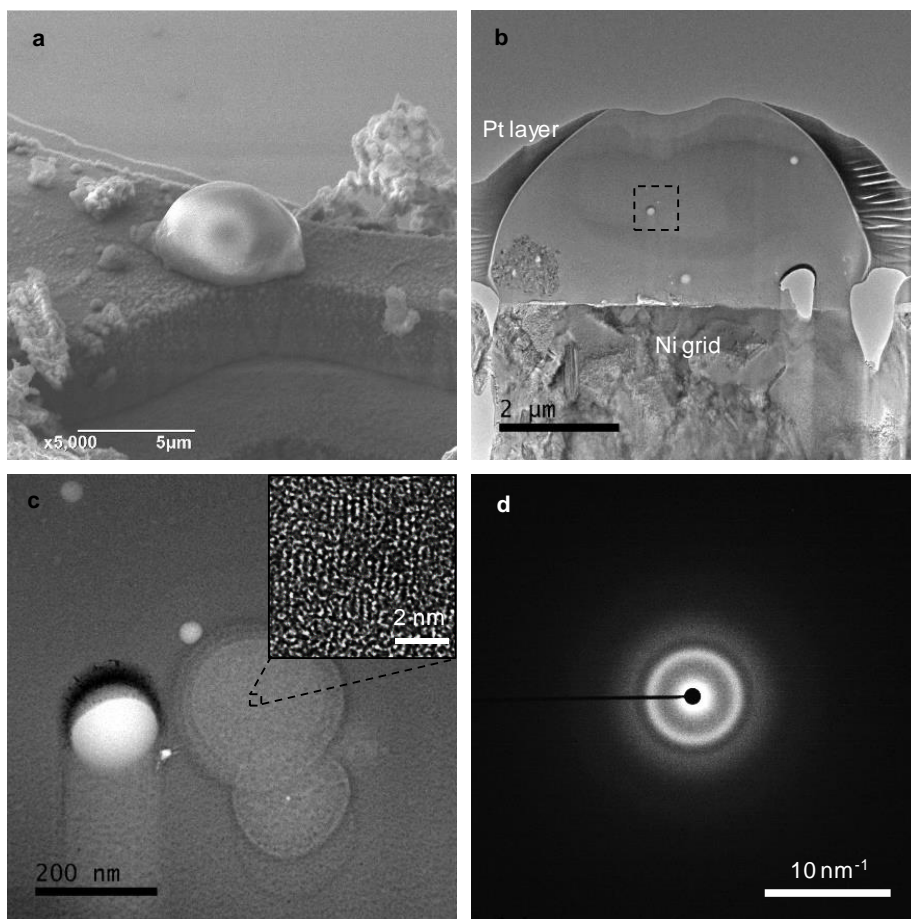


Figure 2.7. Cross-sectional investigation of liquid-quenched amorphous $\text{NaYF}_4\text{:SiO}_2$ (A- $\text{NaYF}_4\text{:SiO}_2$). a-b, SEM image of the as-synthesized A- $\text{NaYF}_4\text{:SiO}_2$ (a) and its cross-sectional analysis (b). The thin film of the cross-section was prepared by focused ion beam (FIB) milling for HRTEM analysis. c, The amorphous region was partially crystallized (inset) when the electron beam (200 kV) was focused for high magnification. Usually, a non-glassy amorphous structure experiences recrystallization when it is heated or irradiated by an electron beam, whereas a glassy amorphous structure experiences a glass transition or melting [102,126]. d, The matrix exhibits a typical halo-like pattern of an amorphous structure in the SAED (selected area electron diffraction) pattern.

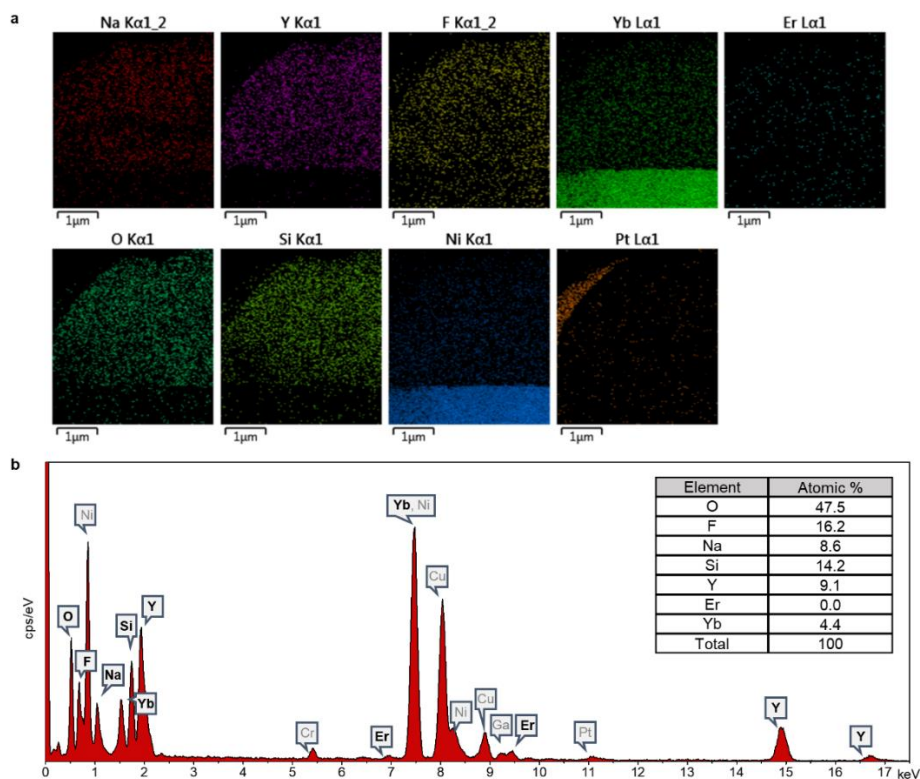


Figure 2.8. Chemical homogeneity of the liquid-quenched amorphous matrix. a, TEM-EDS mapping images of as-synthesized A-NaYF₄:SiO₂, Yb³⁺, Er³⁺ (20%, 2%). The chemical homogeneity was preserved during the process. The mapping image of Yb L α 1 was misconducted because of its spectral overlap with Ni K α 1. b, EDS spectrum of the mapping area and the calculated composition. Note that the EDS analysis is quasi-quantitative; thus, a rough composition of the analyte was obtained. The peak intensities of the elements were barely changed from the initial state (β -NaYF₄:Yb³⁺, Er³⁺ (20%, 2%)). The contents of Si and O were incorporated from the SiO₂ coating layer during the liquid-quenching process. Analytical elements are not included in the composition. (Ga: focused ion beam (FIB) gun source, Pt: protecting layer for FIB process, Ni: substrate, Cr: from the TEM detector, Cu: TEM grid)

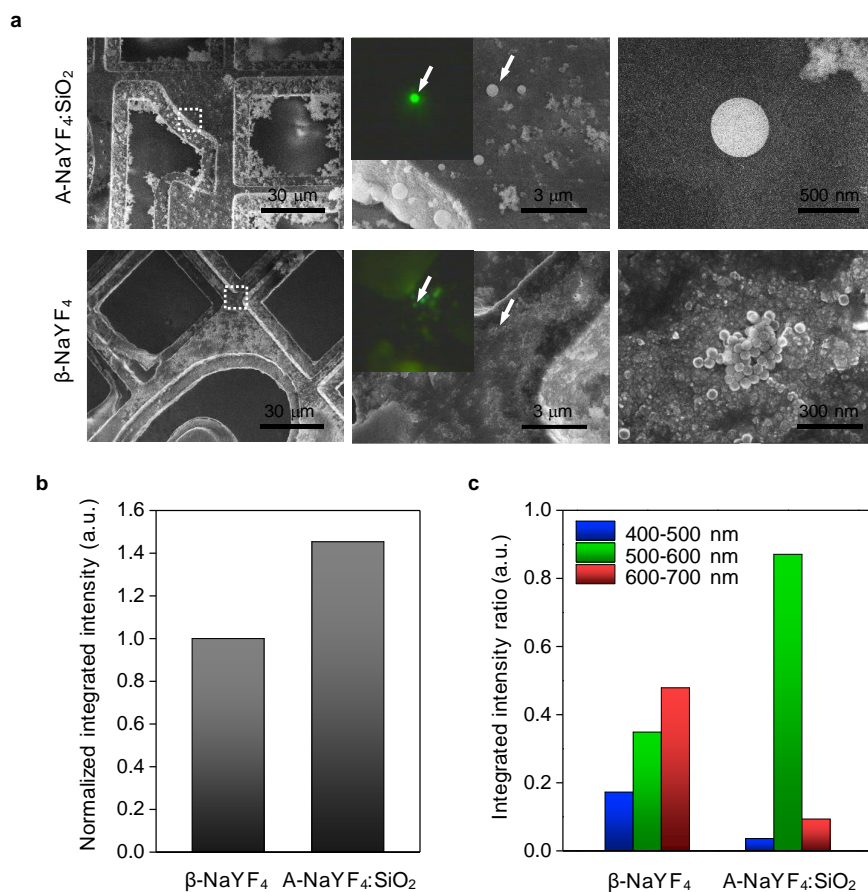


Figure 2.9. Normalized integrated intensity over the entire visible range (400-700 nm) and over three color ranges (blue, green, and red: 400-500, 500-600, and 600-700 nm, respectively). a, The integrated intensity from each sample was collected using optical microscopy, and the volume was correlated using a TEM finder grid. The liquid-quenched amorphous matrix sample was approximated as a perfect sphere, and the approximate SiO₂ volume was extracted for a fair comparison. Approximately 80 nanocrystals with 45 nm diameters were used to calculate the total volume of the crystalline sample. The surface quenching effect of the nanocrystals was compensated by applying an ‘ideal volume-to-size factor ($\times 1.25$ for a 45 nm nanocrystal)’ [96].

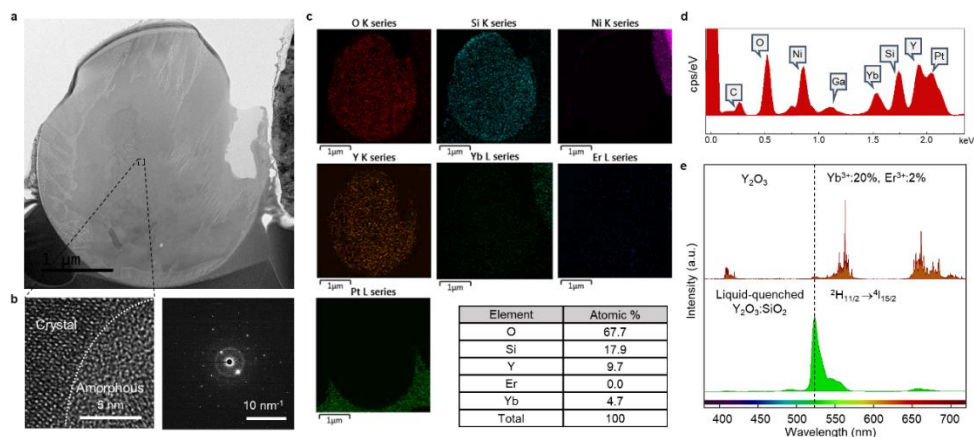


Figure 2.10. Liquid-quenched amorphous $\text{Y}_2\text{O}_3:\text{SiO}_2$. a-b, The liquid-quenched $\text{Y}_2\text{O}_3:\text{SiO}_2$ (a) was separated into two phases; the crystalline and amorphous regions were confirmed by the HRTEM image (left image of b) and the SAED pattern (right image of b). Crystalline $\text{Y}_2\text{Si}_x\text{O}_{3+2x}$ was possibly formed during instant quenching. c-d, EDS mapping data confirming that the two separate phases are compositionally homogeneous (c) and the chemical composition calculated from EDS analysis (d). e, Upconversion emission of semi-crystalline $\text{Y}_2\text{O}_3:\text{SiO}_2$ was an intense green single-band spectrum similar to that of $\text{A-NaYF}_4:\text{SiO}_2$, despite the liquid-quenched microstructure being a mixture of crystalline and amorphous regions.

$J \rightarrow J'$	Wavelength (nm)	U_2	U_4	U_6
${}^4F_{9/2} \rightarrow {}^4I_{15/2}$	655	0	0.5655	0.4651
${}^4S_{3/2} \rightarrow {}^4I_{15/2}$	545	0	0	0.2285
${}^2H_{11/2} \rightarrow {}^4I_{15/2}$	525	0.7056	0.4109	0.087
${}^4F_{7/2} \rightarrow {}^4I_{15/2}$	490	0	0.1467	0.6273
${}^2H_{9/2} \rightarrow {}^4I_{15/2}$	408	0	0.078	0.17
${}^2H_{9/2} \rightarrow {}^4I_{13/2}$	555	0.073	0.12	0.41
${}^2H_{9/2} \rightarrow {}^4I_{11/2}$	700	0.077	0.11	0.096

Table 2.1. Reduced matrix elements of the visible Er^{3+} transitions for the relative JO parameters calculation [111].

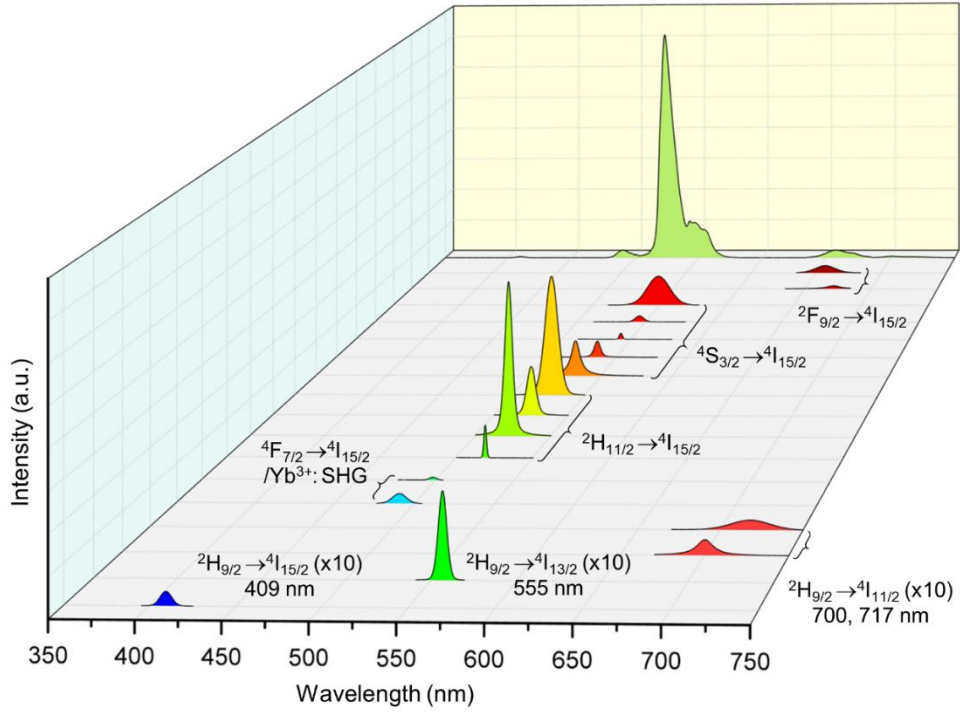


Figure 2.11. Gaussian-Lorentzian-fitted single-band upconversion emission spectrum of A-NaYF₄:SiO₂, Yb³⁺, Er³⁺ (20%, 2%).

Host matrix	Decay time of radiative transition						
	$^2H_{9/2} \rightarrow ^4I_{15/2}$	$^2F_{5/2} \rightarrow ^2F_{7/2}$	$^2H_{11/2} \rightarrow ^4I_{15/2}$	$^4S_{3/2} \rightarrow ^4I_{15/2}$	$^2H_{9/2} \rightarrow ^4I_{13/2}$	$^2F_{9/2} \rightarrow ^4I_{15/2}$	$^2H_{9/2} \rightarrow ^4I_{11/2}$
β -NaYF ₄	90.5	N.D.	171.9	191.7	47.9	387.8	68.6
A-NaYF ₄ :SiO ₂	6.6	6.6	0.2	5.1	N.D.	4.3	N.D.

N.D. means "not detectable" due to weak signal

Table 2.2. Upconversion luminescence decay times of β -NaYF₄ and A-NaYF₄:SiO₂ co-doped with Yb³⁺ and Er³⁺ ions.

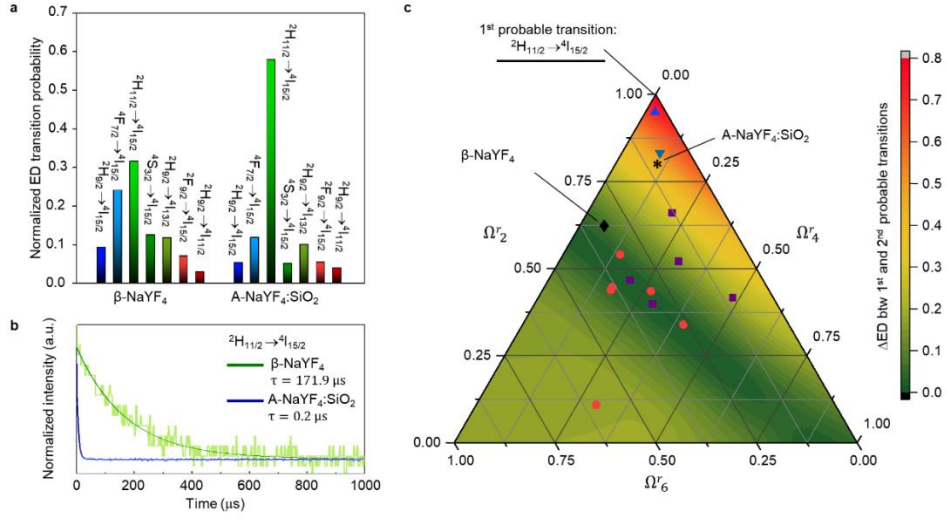


Figure 2.12. (a-b) Normalized electric-dipole transition probabilities (a) and decay curves of the $2\text{H}_{11/2} \rightarrow 4\text{I}_{15/2}$ transition (b) of Er^{3+} embedded in $\beta\text{-NaYF}_4$ and $\text{A-NaYF}_4\text{:SiO}_2$. (c) Ternary diagram of the normalized electric-dipole transition probability difference (ΔED) between the 1st and 2nd probable transitions of Er^{3+} plotted by the relative values of the JO parameters (Ω_{λ}^r , $\Sigma\Omega_{\lambda}^r = 1$). Marked points correspond to the relative JO parameters of Er^{3+} ions embedded in various host matrices. ($\text{A-NaYF}_4\text{:SiO}_2$ (*) is estimated in the present study. Data for ErBr_3 vapor (\blacktriangle), molten $\text{LiNO}_3 + \text{KNO}_3$ (\blacktriangledown), and glass (\blacksquare) are from ref [113], and those for $\beta\text{-NaYF}_4$ (\blacklozenge) and crystals (\bullet) are from ref [109].)

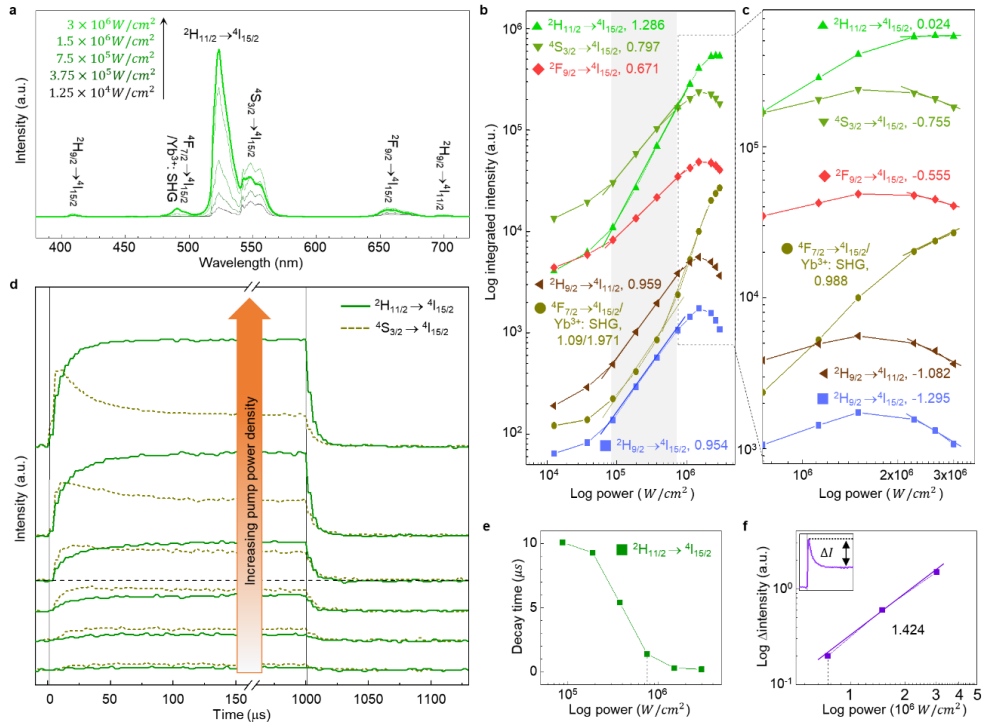


Figure 2.13. Power dependence and temporal behavior of A-NaYF₄:SiO₂ co-doped with Yb³⁺ and Er³⁺: (a) Upconversion luminescence spectra of intense single-band-emitting A-NaYF₄:SiO₂, Yb³⁺, Er³⁺ (20%, 2%) under irradiation at various power densities of the 980 nm pump laser. (b-c) Power dependence of A-NaYF₄:SiO₂, Yb³⁺, Er³⁺ over the entire pump power range (b) and the higher power range (c). The colored box indicates the range of linear dependent emission intensity. (d) Temporal behavior of $2\text{H}_{11/2} \rightarrow 4\text{I}_{15/2}$ and $4\text{S}_{3/2} \rightarrow 4\text{I}_{15/2}$ with increasing pump power density. (e) The decay time of $2\text{H}_{11/2} \rightarrow 4\text{I}_{15/2}$ as a function of the pump power density. (f) Intensity difference (ΔI) of $4\text{S}_{3/2} \rightarrow 4\text{I}_{15/2}$ between the initial rise and the subsequent decay. Dashed lines in (b), (d), (e) and (f) indicate the threshold power density of $7.5 \times 10^5 \text{ W cm}^{-2}$ at which the extraordinary temporal behavior of $4\text{S}_{3/2} \rightarrow 4\text{I}_{15/2}$ is observed.

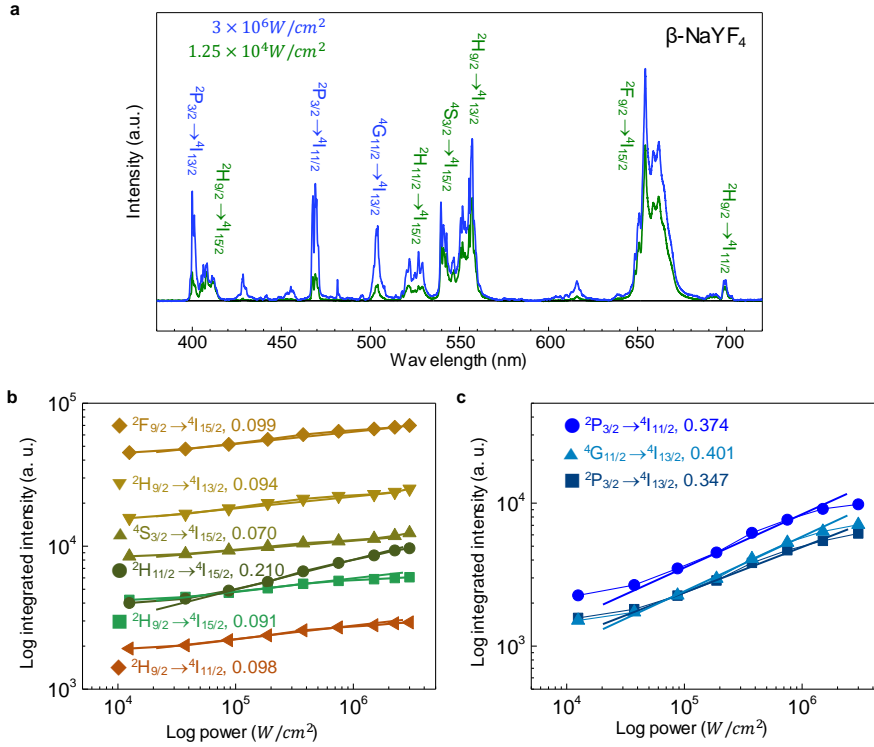


Figure 2.14. Power dependence of crystalline $\beta\text{-NaYF}_4\text{:Yb}^{3+}, \text{Er}^{3+}$ (20%, 2%).

a, Upconversion luminescence spectra of multiband $\beta\text{-NaYF}_4\text{:Yb}^{3+}, \text{Er}^{3+}$ (20%, 2%) under low and high pump power densities of 980 nm laser excitation. **b-c**, Power dependence of the low-power saturated group (**b**) and the high-power saturated group (**c**) of $\beta\text{-NaYF}_4\text{:Yb}^{3+}, \text{Er}^{3+}$ in a double-logarithmic plot.

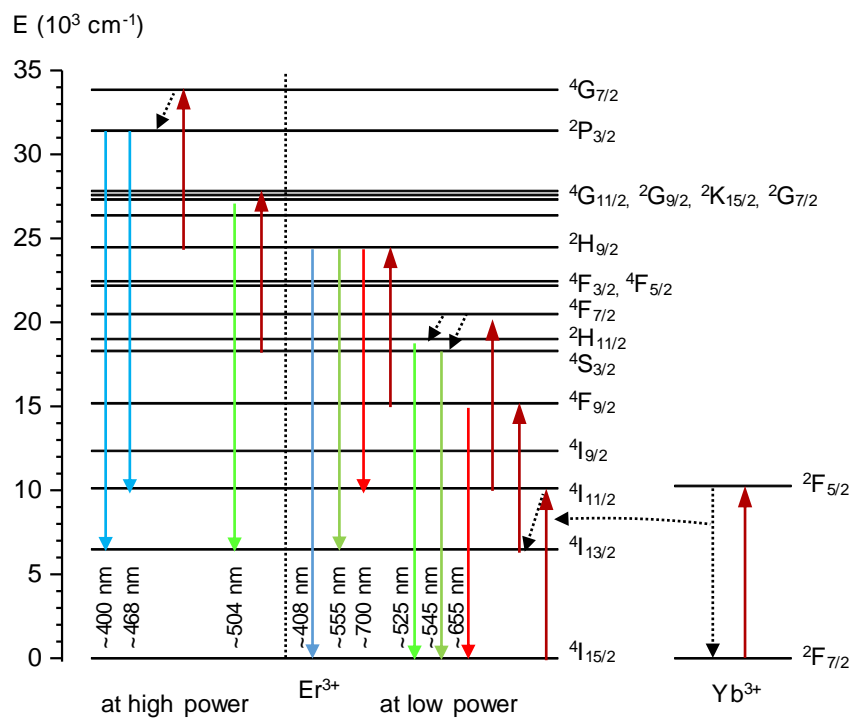


Figure 2.15. Energy diagram and upconversion pathways of β -NaYF₄:Yb³⁺, Er³⁺.

β -NaYF₄:Yb³⁺, Er³⁺ (20%, 2%) under 980 nm CW laser of $3 \times 10^6 \text{ W/cm}^2$

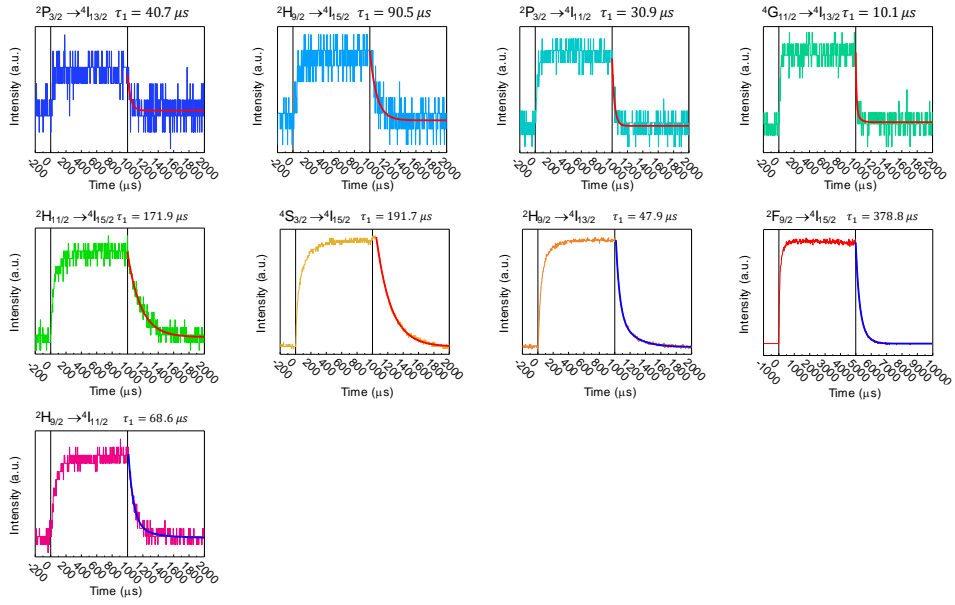


Figure 2.16. Upconversion luminescence decay curves of crystalline β -NaYF₄ co-doped with Yb³⁺ and Er³⁺ ions.

A-NaYF₄:SiO₂, Yb³⁺, Er³⁺ (20%, 2%) under 980 nm CW laser of $3 \times 10^6 \text{ W/cm}^2$

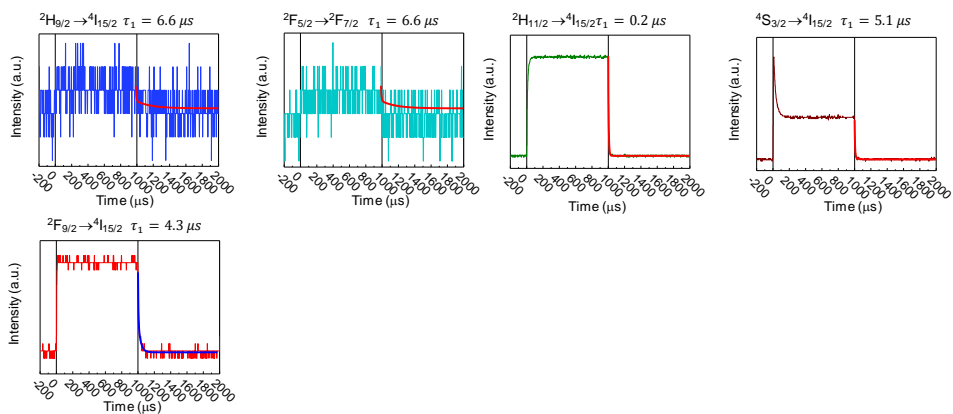


Figure 2.17. Upconversion luminescence decay curves of A-NaYF₄:SiO₂ co-doped with Yb³⁺ and Er³⁺ ions.

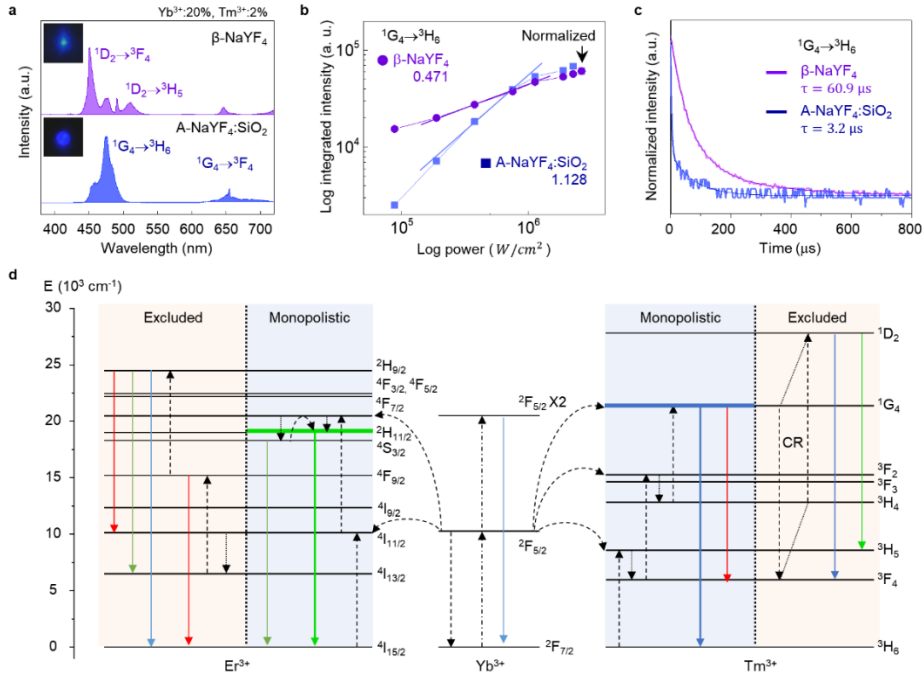


Figure 2.18. Single-band upconversion luminescence of A-NaYF₄:SiO₂, Yb³⁺, Tm³⁺ and the proposed mechanism of single-band upconversion: (a) Upconversion luminescence spectra of A-NaYF₄:SiO₂ and β-NaYF₄ co-doped with Yb³⁺ and Tm³⁺ (20%, 2%) at 3 × 10⁶ W cm⁻². (b-c) Comparison of the power dependence (b) and the decay time (c) of ¹G₄ → ³H₆ corresponding to the enhanced transition in the liquid-quenched amorphous matrix. The intensity was normalized to the end point of maximum power. (d) The proposed mechanism of the single-band upconversion in Er³⁺ and Tm³⁺ sensitized by Yb³⁺. Dotted, dot-dashed, dashed, and solid lines indicate non-radiative relaxation, photon absorption, energy transfer, and upconversion emission, respectively. CR indicates cross-relaxation.

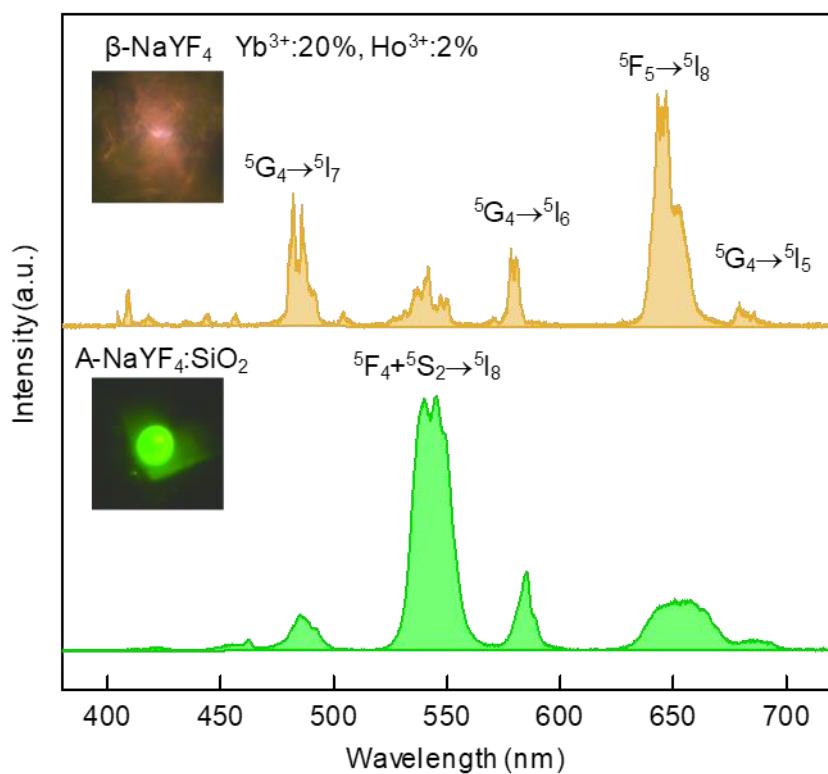


Figure 2.19. Upconversion luminescence spectrum of A-NaYF₄:SiO₂, Yb³⁺, Ho³⁺ (20%, 2%).

Chapter 3

Ultralow-threshold wavelength- tunable continuous-wave upconversion microlasers

3.1 Introduction

Microscale lasers have become crucial to widespread applications of on-chip optoelectronics [127-129] and biomedical photonics [130-132] for the efficient delivery of coherent photons into designated spaces without significant optical power loss by simply locating the light sources near the target volume. Such demands have given rise to a compelling pursuit of smaller but more efficient microlasers. To this end, diverse materials, structures, and principles have been tested, *e.g.*, vertical-cavity surface-emitting lasers [133-135], whispering-gallery-mode lasers [136-138], photonic-crystal lasers [139-141], plasmonic lasers [142-144], and upconversion lasers [145-148]. In particular, an ultralow-threshold, wavelength-tunable, and continuous-wave microlaser with a narrow linewidth has been sought for high-resolution spectroscopy [149-151], interferometric phase imaging [152,153], and wavelength-division-multiplexing [154,155]. However, these applications have remained challenging because a microscale cavity makes lasing difficult due to high radiative intracavity loss [156,157] and a small pump-to-gain interaction volume [158,159].

Lanthanide-doped upconversion nanoparticles (UcNPs) generate ultraviolet (UV) and visible-wavelength emission under near-infrared wavelength excitation via multiphoton absorption [160]. Compared to traditional luminophores such as fluorescent dyes and quantum dots, the use

of UCNPs to create high-energy photons via low-energy pump photons is biologically amicable, photobleaching-resistant, and non-blinking, and provides deeper penetration into human tissues ^[1,2]. Furthermore, UCNPs provide a large anti-Stokes-shift, excellent photostability, and intermediate energy states for efficient population inversion [161], making them an attractive gain medium for the development of anti-Stokes-shift microlasers. Therefore, a number of attempts have been made to utilize UCNPs to realize anti-Stokes-shift upconversion microlasers, for example, coating UCNPs on the surface of spherical or cylindrical microresonators [145-148]. However, anti-Stokes-shift laser operation by multiphoton absorption involves a lasing threshold ($>10^7 \text{ W}\cdot\text{cm}^{-2}$) [148] that is five orders of magnitude higher than that associated with Stokes-shift laser operation ($<10^2 \text{ W}\cdot\text{cm}^{-2}$) [129]; as a result, anti-Stokes-shift laser operation has been demonstrated using high-power low-repetition-rate pulsed pump sources, such as Q-switched Nd:YAG pulse lasers with nonlinear optical parametric oscillators [145-147]. Such operation involves enormous equipment costs and low wall-plug efficiencies, discouraging potential users from employing such lasers. As a notable example of progress, a continuous-wave upconversion microlaser was recently reported by ‘energy-looping’ UCNPs coated on a 5- μm -diameter polymeric microsphere [148]. The energy-looping mechanism amplifies the population of an excited state through intrinsic cross-relaxation, allowing for

a significant reduction in the upconversion lasing threshold to as low as 10^4 $\text{W}\cdot\text{cm}^{-2}$ and stable operation with continuous-wave pump sources.

In this chapter, we demonstrate the first realization of an ultralow-threshold, wavelength-tunable, diode-pumped, continuous-wave, upconversion microlaser of 2.44 μm in diameter by liquid quenching of UCNPs. The liquid quenching newly provides 1) a smooth surface texture that enables efficient light coupling to whispering-gallery-mode (WGM) resonators, resulting in low intracavity scattering loss; 2) a monolithic internal structure that inherently supports high pump-to-gain interactions compared to previous coating approaches for upconversion microlasers [145-148]; and 3) a highly efficient energy transfer upconversion (ETU) mechanism, which was enabled by the use of a sensitizer, and a simple emission pathway for the establishment of population inversion. Overall, these superior characteristics of our liquid-quenched upconversion microspheres (LQUMs) resulted in an ultralow upconversion lasing threshold of $43.75 \text{ W}\cdot\text{cm}^{-2}$ with a narrow linewidth, which makes the anti-Stokes-shift-based microlaser competitive against the state-of-the-art Stokes-shift microlasers [129]. Additionally, our upconversion microlasers provide a high wall-plug pump efficiency because they can be directly pumped by 980-nm near-infrared diode lasers, which are widely used in laboratories and industry. Furthermore, the laser output wavelengths of our upconversion microlaser are readily tuned to be as large

as 3.56 nm by a thermally expanded cavity size controlled by the operation temperature and the injection pump power. This tuning process over a wide spectral range is much simpler than that of semiconductor lasers [162]. The operation of the LQUM microlaser was also confirmed with alternative doping ions, implying the device's universal applicability with other lanthanides for the expansion of output laser wavelengths.

3.2 Materials and methods

Materials: $\text{ErCl}_3 \cdot 6\text{H}_2\text{O}$ (99.9%), $\text{YCl}_3 \cdot 6\text{H}_2\text{O}$ (99.9%), $\text{YbCl}_3 \cdot 6\text{H}_2\text{O}$ (99.9%), $\text{TmCl}_3 \cdot 6\text{H}_2\text{O}$ (99.9%), $\text{HoCl}_3 \cdot 6\text{H}_2\text{O}$ (99.9%), NaOH (98+%), NH_4F (98+%), 1-octadecene (ODE) (90%), oleic acid (OA) (90%), Igepal CO-520, $\text{NH}_3 \cdot \text{H}_2\text{O}$ (30 wt%), and tetraethyl orthosilicate (TEOS) (99.0+%) were purchased from Sigma-Aldrich. All chemicals were used as received without further purification.

Preparation of upconversion nanoparticles: Silica-coated $\beta\text{-NaYF}_4\text{:Yb}^{3+}, \text{Er}^{3+}$ (20%, 2%) upconversion nanoparticles (UcNPs) were prepared by an organometallic method. A stoichiometric amount of $\text{LnCl}_3 \cdot 6\text{H}_2\text{O}$ (1 mmol, $\text{Ln}=\text{Y}, \text{Yb}, \text{Er}$) was dissolved in 15 ml of ODE and 6 ml of OA under vigorous stirring in a 250-ml three-neck flask. The mixture was heated to 160 °C for 1 h under an inert atmosphere to remove water and oxygen. After cooling to 25 °C, 10 ml of methanol containing NH_4F and NaOH was added dropwise

and stirred for 30 min, followed by heating to 120 °C for 1 h to remove the methanol. Then, UCNPs of ~45 nm in diameter were synthesized by heating to 320 °C for 1 h. After being washed several times with ethanol, the synthesized UCNPs (1 mmol) were redispersed in 10 ml of cyclohexane. To coat a thin SiO₂ layer of ~8 nm in thickness, 0.4 ml of the prepared UCNP solution (0.04 mmol) was mixed with 0.5 ml of Igepal CO-520 and 9.6 ml of cyclohexane in a 20-ml glass vial and stirred for 30 min before 0.08 ml of NH₃·H₂O was added. Then, 0.04 ml of TEOS, a SiO₂ precursor, was added to the solution, and the container was sealed hermetically with vigorous stirring for 24 hours to form an amorphous silica layer. As-prepared UCNPs coated with silica were washed with ethanol and stored in distilled water before use. To alter the lanthanide activator ion from Er³⁺ to Tm³⁺, TmCl₃·6H₂O was substituted for ErCl₃·6H₂O, while the other procedures were identical.

Liquid-quenched upconversion microspheres: Liquid-quenched upconversion microspheres (LQUMs) were fabricated by following our previous work [163]. A solution of UCNPs (40 µl) was deposited onto a Si wafer (5 mm × 5 mm) to form a hemispherical drop, followed by drying at 65 °C. Then, the UCNPs were annealed at 250 °C for 12 h in a low-vacuum furnace (7.0×10^{-2} Torr) to facilitate the laser melting process. By rubbing, the UCNPs were deposited on a TEM finder grid's wall and terrace. The prepared TEM finder grid was loaded on a glass slide and covered by a cover

slip to illuminate the focused laser beam through the oil-type 100× objective lens of an optical microscope. Under the focused laser spot of 3 MW cm^{-2} (a single-mode 980-nm continuous-wave diode laser, RGB photonics, PB 980-250), the UcNPs were rapidly liquefied by the heat generated during the upconversion process and spontaneously quenched to the LQUM on the TEM finder grid's wall and terrace.

Optical characterization: The LQUMs were characterized using the same optical setup employed for fabrication. The LQUMs were pumped and observed using the same objective lens. Before observation, the emission was filtered by a short-pass filter (95% transmittance at 400-745 nm, Chromafilter, ET750sp-2p8). The emission spectrum was measured by an EMCCD (Andor, DU970P) equipped with a spectrograph (Andor, Shamrock 303i). With a grating of $1200 \text{ lines}\cdot\text{mm}^{-1}$ (500 nm centered), the spectral resolution achieved by our setup was 0.12 nm (confirmed by a 532-nm laser with a linewidth of 0.28 pm). The emissive spot of the LQUM was precisely selected by an entrance slit of 20 μm to yield pure laser emission. A half-wave plate (Thorlabs, WPH10M-980) and a birefringent polarizer (Thorlabs, GL 10) were installed before and after the excitation, respectively, to investigate the transverse modes and the polarization of the laser emission.

Microscopic temperature control: The operation temperature of the LQUM microlasers was controlled using a home-built microscopic heating system

and calibrated by an upconversion temperature sensor. Heating above 423 K was restrained due to the operating temperature range of the optical microscope. After heating, the sample was cooled naturally.

3.3 Liquid-quenched upconversion microspheres as an optical resonator

Monolithic lanthanide-doped microspheres, serving as microscale WGM resonators, were fabricated by rapid liquid quenching of UcNPs as shown in Figure 3.1a, following the procedures described in our previous report [163]. A group of silica-coated β -NaYF₄:Yb³⁺, Er³⁺ (or Tm³⁺) (20%, 2%) UcNPs on a TEM grid was liquefied by focusing an intense continuous-wave 980-nm diode laser beam with a photon density of 3.0 MW·cm⁻². The molten upconversion host matrix was irreversibly solidified into a uniform and smooth microsphere with the aid of surface tension during liquefaction (Figure 3.1b). Because the surface tension enables excellent surface finish [137], noticeable defects on the microsphere's surface were not observed in a 1.4-nm high-resolution SEM image (Figure 3.1c). As a result, the fabricated LQUM serves as an excellent optical resonator that features strong light confinement in WGMs for laser operation [164].

We investigated the size effect on the laser emission characteristics because the WGM resonances are highly sensitive to the resonator's size

[164]. We found that the best laser emission was observed from a LQUM of 2.44 μm in diameter (Figure 3.1). At diameters smaller than 2.44 μm , an exponential increase in curvature loss [130] and the mismatch of resonance conditions with each emission band impede efficient laser emission (Figure 3.2). Nevertheless, the proposed liquid-quenching method allows for miniaturization of the resonator down to its ultimate boundary, yielding the smallest upconversion microlaser ever. Compared to the conventional upconversion microlasers fabricated by UcNP coating methods [145-148], the LQUM provides lower intracavity loss [165] and higher pump-to-gain interaction [166] because of the seamless cavity design and high surface smoothness with the internally incorporated lanthanides. We believe that such successful miniaturization of the WGM resonator is one of the most important factors in lasing threshold reduction by strengthening the quantum electrodynamic effect of the optical cavity [136,167].

3.4 Continuous-wave upconversion lasing

A LQUM of a 2.44- μm in diameter (Figure 3.1b, c) was investigated for continuous-wave anti-Stokes-shift upconversion lasing by pumping with a 980-nm diode laser at a power density of 3.16 $\text{MW}\cdot\text{cm}^{-2}$. The small and smooth WGM resonator exhibited excellent laser emission characteristics. The intense laser outputs were observed at multiple emission bands of 525,

550, and 665 nm (Figure 3.1d). The narrowest spectral linewidth was measured to be 0.27 nm at 525.79 nm, the Q factor of which was as high as 1,947, and the free-spectral range corresponded to 22.44 nm; the former implies a low optical loss in the resonator, and the latter reflects the small size of the resonator. The average output power of each lasing mode was stable without significant drift or fluctuation (Figure 3.3) over the entire investigation period of several days. Additionally, the laser emission exhibited negligible sensitivity to the pump laser's polarization axis owing to the amorphous nature of the LQUM [163] (Figure 3.4), which relaxes pump requirements.

Energy transfer upconversion (ETU) is the most efficient upconversion mechanism that can utilize a sensitizer (*e.g.*, Yb^{3+}) to enhance the upconversion efficiency [1]. However, because the use of sensitizers generally hinders the population inversion of activators (*e.g.*, Er^{3+} or Tm^{3+}) through detrimental energy back transfer [160], ETU has been difficult to incorporate into the upconversion laser process [160]. However, the LQUM provides a unique ETU mechanism in sensitizer and activator codoping systems, which effectively dominates over non-radiative energy transfers, such as energy back transfer and cross-relaxation. The reason is that the radiation lifetime is exceptionally short, reaching a few microseconds compared with tens or hundreds of microseconds in conventional

upconversion host materials [163]. Therefore, the ETU of LQUM provides a significant benefit in exploiting the sensitizer for upconversion lasing process. Furthermore, because the LQUM provides much simpler emission pathways than other upconversion materials [1], the upconverted photons in the LQUM can be effectively concentrated in the upconversion lasing states of $^2H_{11/2}$, $^4S_{3/2} (\rightarrow ^4I_{15/2})$ and $^4F_{9/2} (\rightarrow ^4I_{15/2})$ for green (525 nm, 550 nm) and red (660 nm) bands, respectively (Figure 3.1e). Taken together, the efficient ETU and the simple emission pathway could provide an unprecedented advantage in achieving efficient population inversion of upconversion microlasers.

3.5 Lasing threshold investigation

Through the smooth surface and effective photon transfer in the LQUM, as well as the enhanced pump-to-gain interaction, we could generate stable continuous-wave lasing at pump power densities below $10^3 \text{ W}\cdot\text{cm}^{-2}$ (Figure 3.5a, b), which is a remarkable finding for anti-Stokes-shift microlasers. The laser peaks were generated following the ascending order of the energy levels of the excited states of each peak, from $^4F_{9/2}$, $^4S_{3/2}$ to $^2H_{11/2}$, as shown in Figure 3.5c. This order indicates that multiphonon relaxation is involved in the lasing process to populate the lower excited energy. Resultantly, the lowest lasing threshold of $43.75 \text{ W}\cdot\text{cm}^{-2}$ was observed at $^4F_{9/2} \rightarrow ^4I_{15/2}$. As the pump power increases, the intensity of the laser peaks

increases proportionally with the upconversion luminescence intensity of their corresponding emission bands, where the power dependence of the green emission band is higher than that of the red emission band, thus yielding an intense laser spectrum, as shown in Figure 3.1d (Figure 3.6). Above the lasing threshold, the spectral linewidth of each lasing mode decreases and finally converges to 0.27, 0.28, and 0.48 nm at 525, 550, and 665 nm, respectively (Figure 3.5d). Such narrow linewidths have never been obtained in a continuous-wave microlaser of a few microns in diameter.

3.6 Classical laser physics

Next, we analyzed the spatial, spectral, and polarization characteristics of the LQUM microlaser in accordance with classical laser physics, as shown in Figure 3.7. The output beams are emitted from both sides of the microsphere rim; one beam circulates in the clockwise direction along the pump beam direction, whereas the other beam circulates in the counterclockwise direction [138]. Each laser peak showed a distinct polarization mode, transverse electric (TE) mode or transverse magnetic (TM) mode; the overall lasing wavelengths from mode number 15 to 20 agree well with the theoretical calculation based on asymptotic solutions [168]. Because a small sample volume restricts the refractometry measurement, we were not able to directly measure the refractive index of the LQUM. Nevertheless, by

virtue of its sparse and simple lasing spectrum (only the first-order mode there exists), the refractive index was approximated from the laser emission spectrum. We used the laser emission spectrum attained under the coldest pump conditions (Figure 3.8a) to provide the precise radius of the LQUM, which was determined by SEM imaging (2.44 μm). Using asymptotic solutions⁴, the integer mode numbers of the transverse magnetic mode laser peaks were determined to be 14~20 by using a constant refractive index value of 1.73 with the least-squares regression method. However, under real conditions, because the refractive index varies with the given wavelengths (*i.e.*, not constant), we recalculated the refractive index at the given wavelengths using the asymptotic solutions with the determined mode numbers (marked in Figure 3.8b). From the recalculated refractive indices, we could fit the refractive index curve (n) using the one-term Sellmeier equation⁵ (one of the simplest equations with high accuracy in the visible range for many oxides and silicates);

$$\frac{1}{n^2 - 1} = -\frac{A}{\lambda^2} + B$$

where parameter A gives the dispersion of the material and parameter B predicts the refractive index value at infinite wavelength, $\lambda = \infty$. As a result, we could calculate the one-term Sellmeier parameters of the LQUM: $A = 109.1 \times 10^{-16} \text{ m}^2$ and $B = 0.5366$. The dispersion (*i.e.*, parameter A) of the

LQUM is unusually higher, as much as that of transition metal compounds ($>80 \times 10^{-16} \text{ m}^2$), than that of conventional upconversion host materials⁶. Such high dispersion supports the high refractive index of the LQUM⁷. Notably, the higher refractive index of the LQUM (~ 1.73) compared with the refractive indices of the initial materials, $\beta\text{-NaYF}_4$ (~ 1.48)⁸ and amorphous silica (~ 1.45)⁹, is advantageous for light confinement in an optical cavity¹⁰, contributing to the successful miniaturization of the upconversion microlaser.

The emission beams of the LQUM all exhibited well-defined Gaussian shapes for both the TE and TM modes over a broad spectral range from 520 to 680 nm (Figure 3.7b and 3c); this finding was confirmed by deconvoluting the spatial modes into central broadband upconversion luminescence and narrow-band side modes (Figure 3.7c). The same spatial profile and spectral distribution of the pair of emission beams with different circulating directions support the high-quality surface and high internal homogeneity of the microspheres [169]. The emission polarization states of the TE and TM modes were confirmed by rotating a birefringent polarizer with a high extinction ratio of $10^6:1$, as shown in Figure 3.7a. Each lasing mode showed a distinct linear TE or TM polarization state (Figure 3.7d and 3.7e), which agreed well with the theoretical expectation for the WGM. For the TM_{20} mode, the intensity ratio between the two polarization states was 90:10, as shown in Figure 3.7f. Such a linear polarization state in microlasers

would allow for the intracellular sensing of molecular orientations attached to the microsphere's surface [170].

3.7 Robust operation and reversible wavelength-tunability

Wavelength tunability is a prerequisite for a continuous-wave laser for high-resolution spectroscopy to scan the laser wavelength over atomic/molecular absorption lines and for on-chip optical signal processing to increase the number of signal channels through dense-wavelength-division-multiplexing. The multiple output wavelengths of our upconversion microlasers can be tuned either by controlling the WGM cavity size via temperature or by adjusting the injection pump power density (Figure 3.9a). To demonstrate a wide-range wavelength tuning capability, the output wavelengths were first red-shifted by ~ 2.62 nm by increasing the pump power density from 0.01 to 3.16 MWcm^{-2} at 298 K and then red-shifted further by ~ 0.94 nm by increasing the operation temperature of the LQUM microlaser from 298 to 423 K (Figure 3.9b) using a home-built microscopic temperature controller (Figure 3.10). The home-built heating system for the microscopic sample was operated by a temperature controller (Thorlabs, TC200) via the feedback process of a metal ceramic heater (Thorlabs, HT19R) and a temperature detector (Thorlabs, TH100PT) (Figure 3.10a). To adjust the inevitable temperature gradient between the heater and samples, we

conducted temperature calibration via an upconversion temperature sensor¹¹ using β -NaYF₄:Yb³⁺, Er³⁺ (20%, 2%) microparticles. The β -NaYF₄:Yb³⁺, Er³⁺ microparticles were synthesized by the hydrothermal method, as previously reported¹². As-synthesized upconversion microparticles (Figure 3.10b) were deposited on a TEM grid and excited by a CW 980-nm pump laser (Figure 3.10c). Figure 3.10d shows the upconversion spectrum of β -NaYF₄:Yb³⁺, Er³⁺ (20%, 2%) microparticles at various temperatures of the heater. Given that the intensity ratio of $^2H_{11/2} \rightarrow ^4I_{15/2}$ to $^4S_{3/2} \rightarrow ^4I_{15/2}$ (R_{HS}) is dominated by a Boltzmann thermal distribution¹³, the temperature of the sample in the microscopic heating system can be estimated by using the equation $R_{HS} = \alpha \exp(-\Delta E/k_b T)$, where ΔE is the energy separation between the $^2H_{11/2}$ and $^4S_{3/2}$ states ($\sim 800 \text{ cm}^{-1}$), k_b is Boltzmann's constant and T is the absolute temperature. The surrounding temperature of the microscopic sample was calibrated as shown in Figure 3.10e using the constant α , which is determined by a reference value at room temperature. The increase in the internal temperature of the LQUM microlaser causes thermal expansion of the cavity length and an increase in the refractive index, both of which cause a red-shift of the lasing wavelengths [171,172].

Owing to the excellent photo, thermal, and structural stabilities inherited from inorganic upconversion host materials [2], the lasing was well sustained even in a harsh operation environment – at a power density of 3.16

MWcm^{-2} and a temperature of 423 K– without noticeable degradation over 6 hours of continuous operation (Figure 3.9c above). Furthermore, wavelength tuning was confirmed to be repeatable over 30 cycles in a fully reversible manner (Figure 3.9c below). The laser wavelengths were linearly proportional to the applied pump power density (Figure 3.9d) and the operation temperature (Figure 3.9e). Because the lasing wavelength shift simply reflects the partial change from the initial spectral positions, we could observe the largest shift of 3.56 nm at the longest emission band at ~ 660 nm, corresponding to $^4\text{F}_{9/2} \rightarrow ^4\text{I}_{15/2}$. This value is remarkable because such wavelength tunability over several nanometers has never been demonstrated in relatively hard inorganic WGM resonators [172] but only in soft organic ones (*e.g.*, polymers) (\sim several tens of nanometers), which are sensitive to external forces, such as mechanical deformation [173] or electrical field [174]. However, these materials are vulnerable to high temperature and high excitation power, which are often induced to utilize the materials as a strong light source [148]. Our wavelength tuning over a wide spectral range was realized in a much simpler process than the wavelength tuning in semiconductor lasers manufactured by complex deposition and lithography processes [174]. Furthermore, the wavelength coverage of the laser emission by the LQUM was easily expanded from the green and red emission bands of Er^{3+} to the blue emission band of Tm^{3+} by simply adopting Tm^{3+} , one of the

most popular activators, as an alternative to Er^{3+} because the light amplification of the LQUM was realized without a dopant-specific upconversion mechanism that could restrict available activator ions [148]. We observed robust continuous-wave upconversion lasing in the blue emission bands in the Tm^{3+} -doped LQUM of 1.99 μm in diameter, which supports WGM resonances at ~ 475 nm; the lasing threshold was also considerably low at 1.5 kW cm^{-2} (Figure 3.11). We also used Ho^{3+} , but the fabrication was not feasible because the heat generated through the upconversion in Ho^{3+} was insufficient to induce the successful liquid-quenching phenomenon.

3.8 Conclusions

In conclusion, an anti-Stokes-shift upconversion microlaser with an ultralow threshold, long-term stability, continuous-wave operation, narrow spectral linewidth and broad wavelength tunability was demonstrated. Unprecedented microscale monolithic WGM resonators were synthesized with smooth surface texture via rapid liquid quenching of UCNPs while retaining the inorganic material's excellent stability. Furthermore, the miniaturized resonators enabled strong light amplification irrespective of the activator ions with low lasing thresholds. Well-defined multi-wavelength outputs were observed at red, green, and blue wavelengths from Er^{3+} and Tm^{3+} with wavelength tunability over several nanometers. These

upconversion microlasers are directly pumped by widely commercialized 980-nm pump diode lasers, which enables a high wall-plug efficiency, a long lifetime, and wide-spread applications. Therefore, this novel light source will pave a promising way to sub-cellular-scale biotechnologies and on-chip sub-micron-scale optoelectronics.

Work presented in this chapter is currently under preparation for submission (2019).

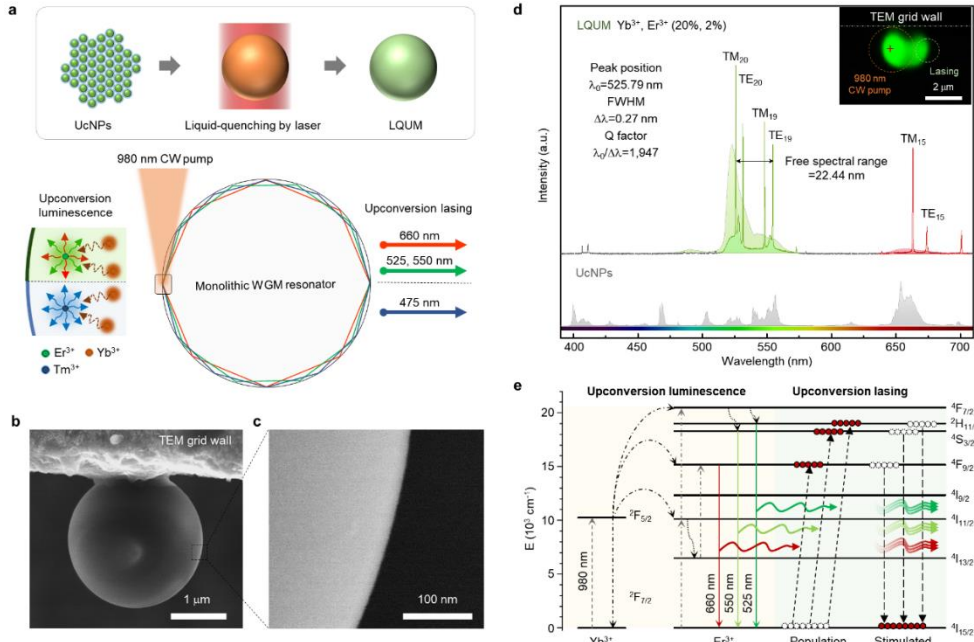


Figure 3.1. Continuous-wave upconversion lasing in liquid-quenched upconversion microspheres (LQUM): a. Schematic of the fabrication of a LQUM and the upconversion lasing in the LQUM through a free-space beam with a 980-nm continuous-wave pump laser. The LQUM accommodates the upconversion lasing through energy transfer upconversion of the activator (Er^{3+} or Tm^{3+}) with the sensitizer (Yb^{3+}). b-c. SEM image of the LQUM at low (b) and high magnification (c). Because the direction of light circulation must be aligned perfectly with the circumference of the microsphere, a LQUM dangling on the TEM grid wall was selected for the formation of WGM resonators. d. The upconversion luminescence of UCNPs (below) and a LQUM with the upconversion lasing (above). Doping concentrations of Yb^{3+} and Er^{3+} were 20% and 2%, respectively. The color inset shows an optical microscopy image of the illuminated LQUM. e. The upconversion lasing supported by the energy transfer upconversion process in the LQUM. Short-dashed, dot-dashed, solid, long-dashed, and dotted lines indicate absorption, energy transfer, spontaneous emission, stimulated emission, and non-radiative relaxation.

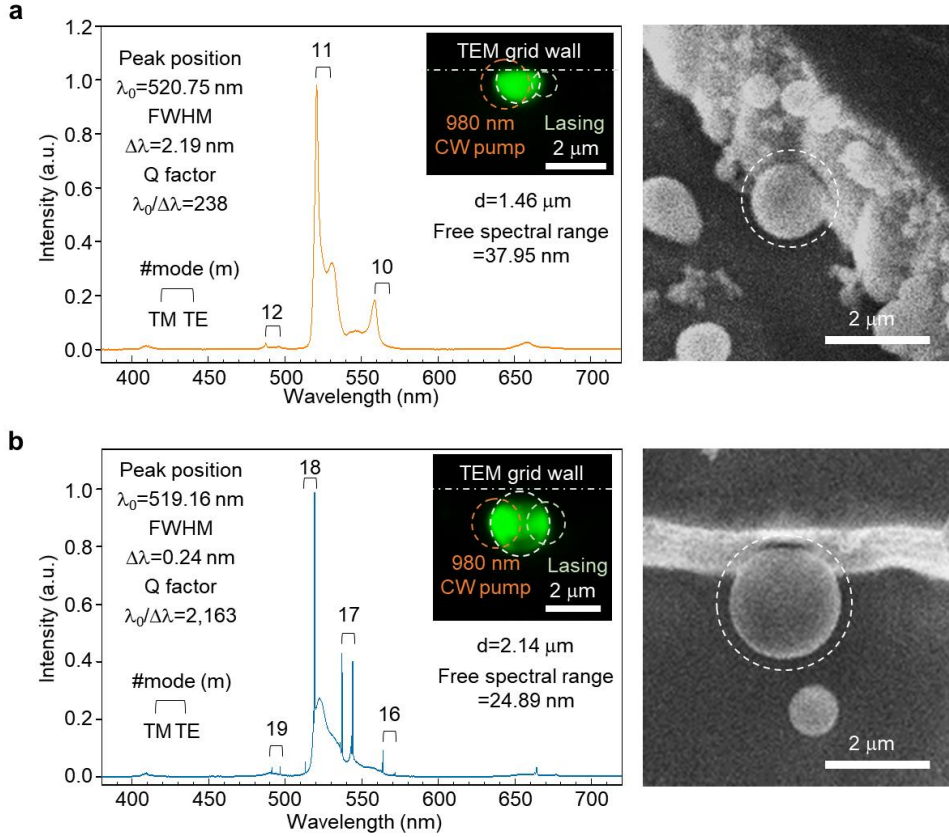


Figure 3.2. Study of the size of liquid-quenched upconversion microspheres (LQUM). a-b. Emission spectrum of upconversion lasing from LQUMs of various diameters. A LQUM of 1.46 μ m in diameter (a) exhibits a low Q factor due to high curvature loss [130]. A LQUM of 2.14 μ m in diameter (b) does not exhibit resonance wavelengths in the red emission band of Er^{3+} ; therefore, the upconverted photons of the red emission band could not participate in the laser process. Therefore, to maximize the laser efficiency, we concluded that 2.44 μ m is the optimal LQUM diameter in the present study, which is in line with the theoretical calculation [175].

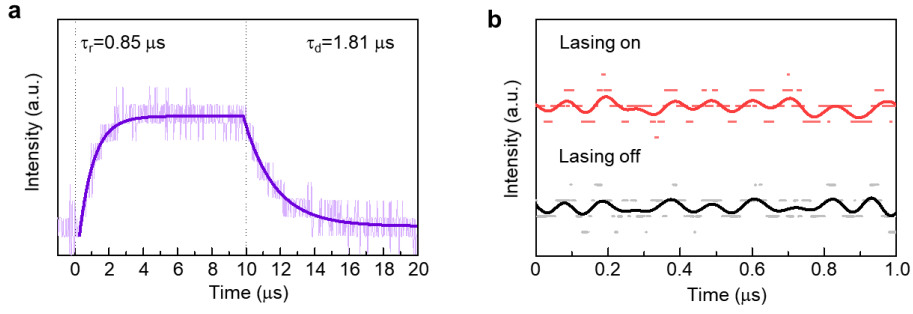


Figure 3.3. Continuous-wave laser operation. a. The rise and decay times were measured using pulsed excitation with a 10-μs pulse width. b. Temporal stability analysis reveals that the continuous-wave laser operation is stable within the instrumental noise level. To investigate the temporal behavior, the excitation pulse was generated from a 980-nm continuous-wave diode laser equipped with an arbitrary function generator (Rigol, DG4102). The emission was measured by a Si-APD (Thorlabs, APD410A) and recorded with an oscilloscope (Rigol, DS2102A-S). The rise and decay curves were fitted with a single-exponential function to calculate the rise and decay times [72] using the equation $y = y_0 + A \times \exp^{-(x-x_0)/t}$.

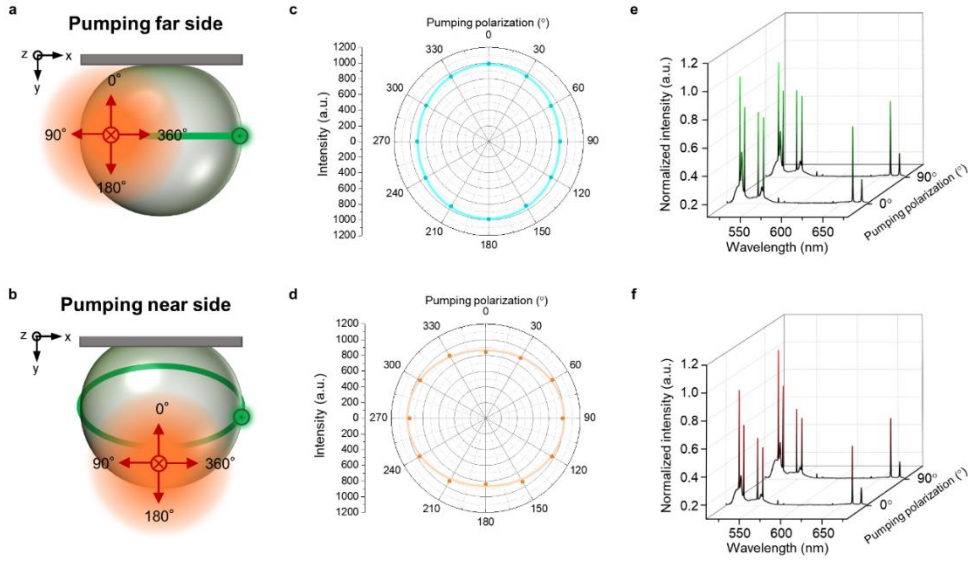


Figure 3.4. Pumping polarization effect. a-b. Two cases of pumping depending on the pumping sides: the pumping far (a) and near (b) sides from the laser emission point. c-d. Polar plot of the intensity of laser emission along with the pumping polarization angle in the xy plane for the far (c) and near (d) sides. e-f. Emission spectrum with the pumping polarization angle in the xy plane (0° and 90°) for the pumping far (e) and near (f) sides. By controlling the pumping polarization angle, we confirmed that the laser emission exhibits negligible sensitivity to the pumping polarization.

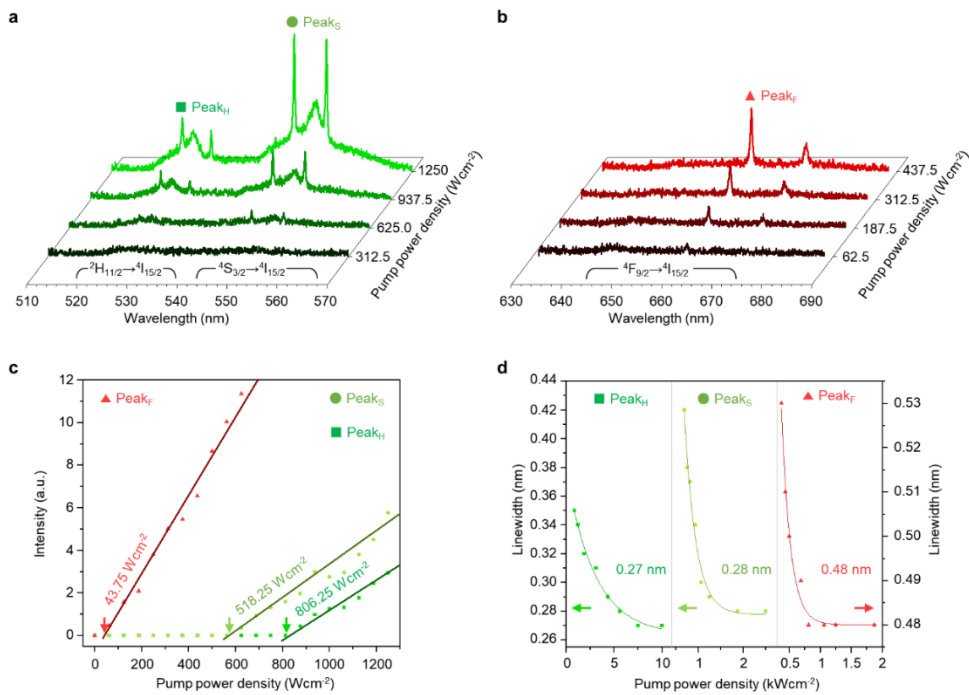


Figure 3.5. Ultralow-threshold continuous-wave upconversion lasing: a-b. Emission spectrum of a LQUM doped with Yb^{3+} and Er^{3+} in green (a) and red (b) bands around the lasing threshold. The laser peaks corresponding to $^2\text{H}_{11/2} \rightarrow ^4\text{I}_{15/2}$, $^4\text{S}_{3/2} \rightarrow ^4\text{I}_{15/2}$ and $^4\text{F}_{9/2} \rightarrow ^4\text{I}_{15/2}$ are labeled to Peak_H, Peak_S and Peak_F, respectively. c-d. Generation (c) and linewidth saturation (d) of the laser peaks with increasing pump power density.

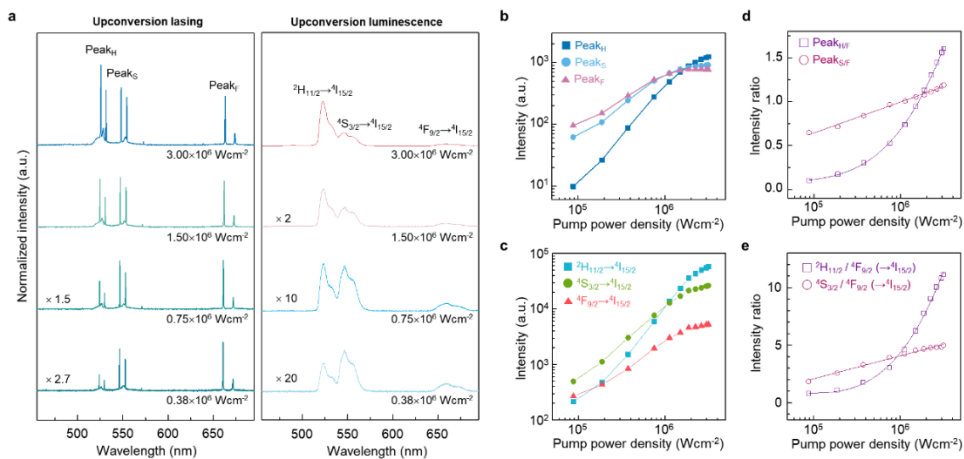


Figure 3.6. Power dependence of upconversion lasing. a. Comparison of upconversion lasing and upconversion luminescence at different pump power densities. b-e. Power dependence of the intensities and the intensity ratios of upconversion lasing (b) and upconversion luminescence (c). Above the lasing thresholds, the upconversion lasing intensity increases proportionally with the upconversion luminescence intensity of the corresponding emission bands. This finding is confirmed by the identical intensity ratios of Peak_H/Peak_F and $^2H_{11/2}/^4F_{9/2} (\rightarrow ^4I_{15/2})$ in upconversion lasing (d) and upconversion luminescence (e), respectively.

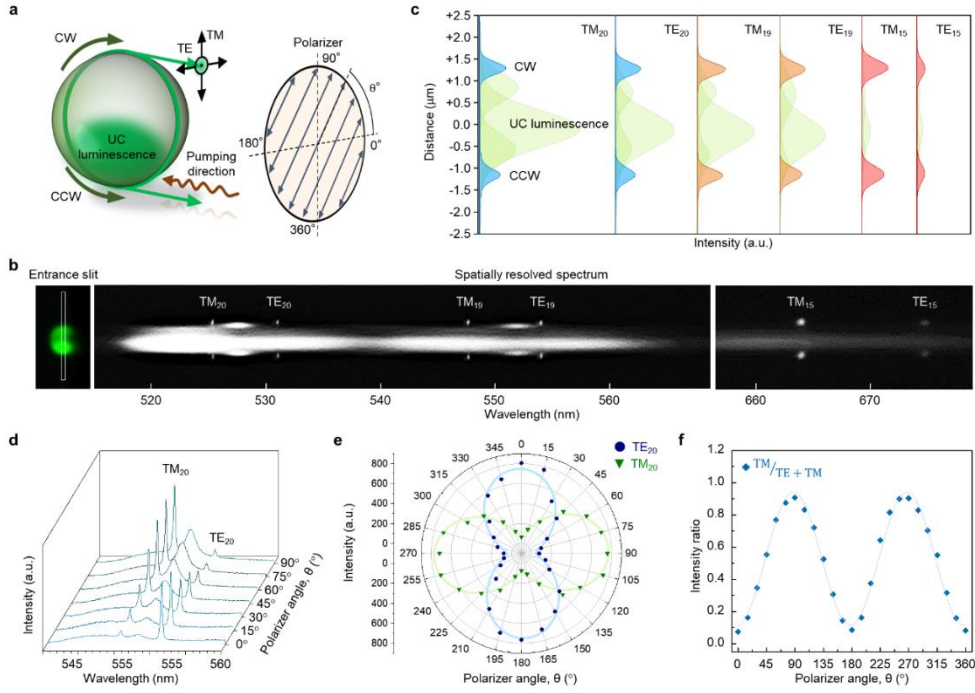


Figure 3.7. Spatial, spectral, and polarization analysis of laser emission: a. Schematic of whispering-gallery-mode analysis in the LQUM determined by circulating directions (clockwise (CW) and counterclockwise (CCW)) and transverse modes (transverse magnetic (TM) and transverse electric (TE) modes). b. Spatially resolved spectrum of the laser emission from the LQUM. The narrow rectangular section was spatially selected by the spectrograph's entrance slit and resolved using a high-resolution grating. c. Deconvolution of the laser peaks using Gaussian-Lorentz fitting. d-f. Polarization investigation of the laser peaks using the emission spectrum (d), a polar plot of the intensities (e) and the intensity ratio (f). The fitting curves in e and f were drawn by a cosine-square function.

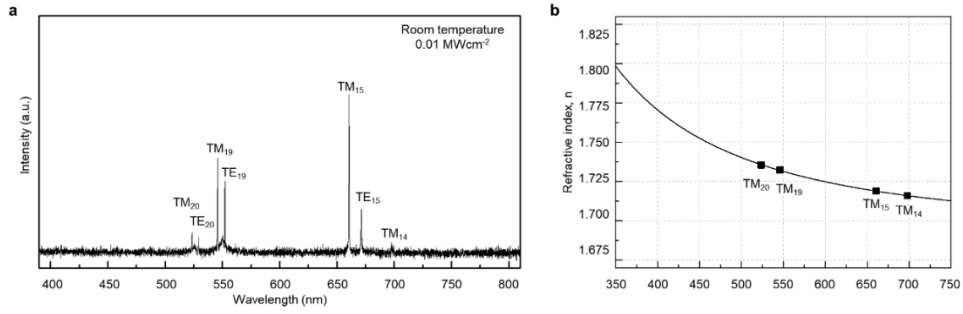


Figure 3.8. Theoretical investigation of laser wavelength. a, The laser emission spectrum of a LQUM under a weak excitation of 0.01 MWcm^{-2} at room temperature was used to investigate the coldest pump conditions. b, Refractive index (n) curves were calculated from the transverse magnetic mode lasing wavelengths of a.

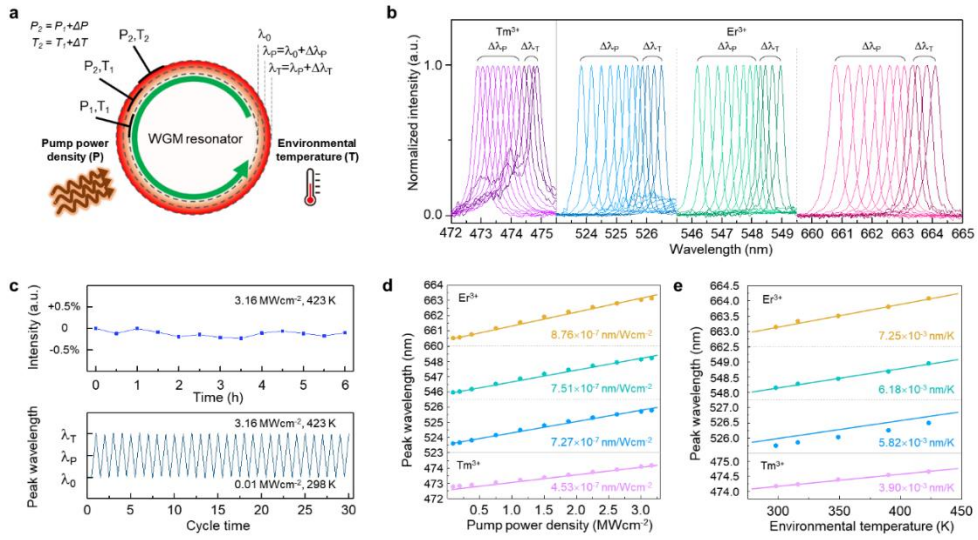


Figure 3.9. Wavelength tuning of laser emission wavelengths: a. Schematic of wavelength tuning achieved by controlling the pump power density (ΔP) and operation temperature (ΔT). The initial lasing wavelength and the shifted lasing wavelengths under the control of the pump power density and operation temperature are indicated by λ_0 , λ_P and λ_T , respectively. b. Emission spectrum of the spectrally tuned laser peaks. $\Delta\lambda_P$ and $\Delta\lambda_T$ indicate the shifts in the lasing wavelength with the increase in pump power density (from 0.01 to 3.16 MW cm⁻²) and operation temperature (from 298 to 423 K). c. Stability analysis in terms of static (above) and dynamic (below) operations. d-e. Linear plots of the laser peaks' wavelength as a function of pump power density (d) and operation temperature (e).

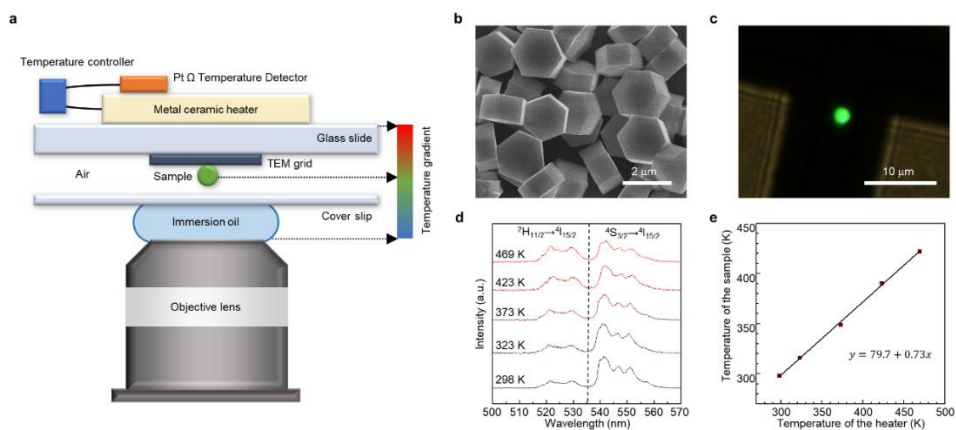


Figure 3.10. Microscopic heating of a sample. a. Schematic of the home-built heating system. b-c. SEM (b) and color (c) images of upconversion microparticles used for temperature calibration. d. Emission spectrum of the upconversion microparticles as a function of the metal ceramic heater's temperature. e. Calibrated temperature obtained using the intensity ratio, $^2H_{11/2}/^4S_{3/2} (\rightarrow ^4I_{15/2})$ of the upconversion microparticles.

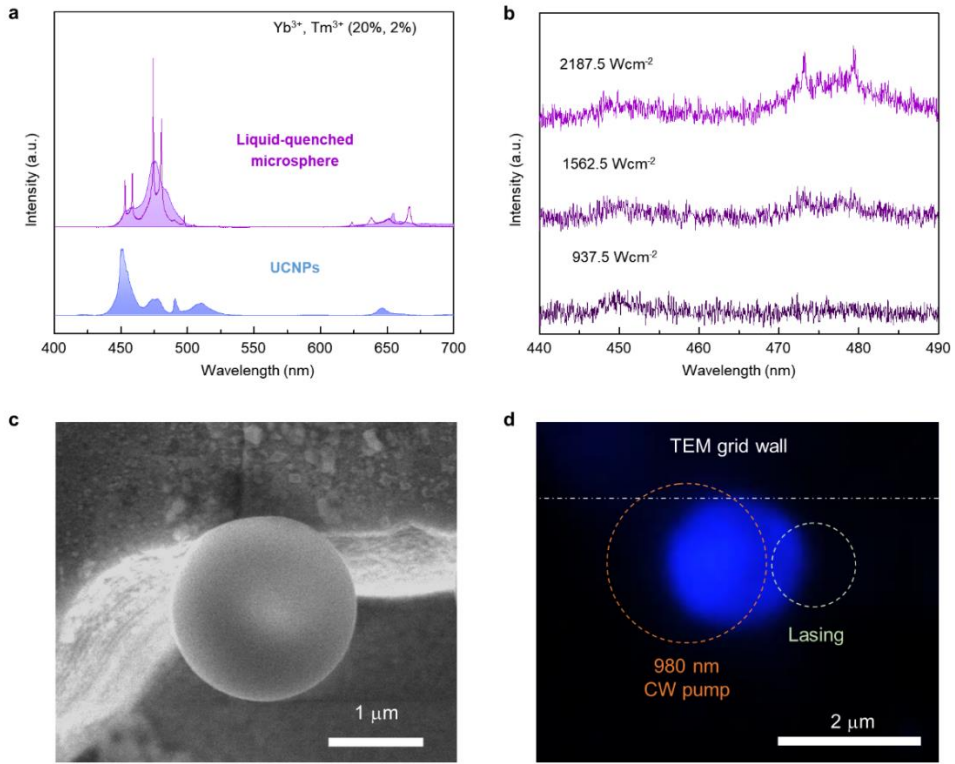


Figure 3.11. a. Upconversion luminescence and upconversion lasing in a LQUM doped with Yb^{3+} and Tm^{3+} (20% and 2%) b. Emission spectrum in the blue emission band around the lasing threshold of $\sim 1.5 \text{ kWcm}^{-2}$. c-d, SEM (c) and color (d) images of a LQUM measuring $1.99 \mu\text{m}$ in diameter doped with Yb^{3+} and Tm^{3+} .

Chapter 4

Conclusions and outlook

4.1 Conclusions

In this thesis, a new class of upconversion host material, which developed by hyper-quenching of the molten inorganic species to possess completely amorphous microstructure without short-range order, is investigated. The bright single-band upconversion emission of Er^3 at green region with exceptionally fast decay time was realized by the matchlessly high transition probabilities originated from the non-centrosymmetric crystal-fields of disordered host matrix. It was found that this upconversion emission accompanies simple and unitary energy transfer pathway possessing the minimal energy loss in two-photon upconversion process. Therefore, the dissipative energy loss (phonon generation) was minimized in contrast to previously demonstrated single-band upconversion at red or NIR regions, which involve complex multistep energy transfer pathways. Furthermore, the altered balance of transition probabilities was found to effectively alleviate detrimental nonradiative energy transfers, such like cross-relaxation and energy back transfer. By lasing experiments, it was found that this unique feature provides a significant privilege to establish population inversion in the excited states of lanthanides. As a result, the highly efficient upconversion lasing compared with other previous materials was demonstrated.

4.2 Outlook

Expanding the capability of upconversion materials, i.e., the development of structurally disordered host matrix, could give the valuable insight for successful realization of the potential upconversion applications, such like deep human brain optogenetics with NIR remote stimulation and microscale optical components for photonic microprocessor (by converting NIR signal to visible signal). For these applications, there are two important breakthroughs to be overcome; the fabrication methods for mass-production and the integration with electric devices. For mass-production, one might try microsecond-pulsed laser-ablation at quenching bath for liquefying inorganic host materials, followed by droplet formation and rapid quenching process. Otherwise, high-pressure spraying of molten inorganic host materials would be a potential method. However, in contrast, integrating with electric devices seems quite difficult because the inorganic host materials are generally insulators. The use of electronic tunneling effect can be a great approach. By concluding the thesis, we believe that bringing the future applications of upconversion in our daily life will be realized by overcoming these challenging tasks which require continued research with multidisciplinary perspectives.

References

- [1] Dong, H., Sun, L. D. & Yan, C. H. Energy transfer in lanthanide upconversion studies for extended optical applications. *Chem. Soc. Rev.* **44**, 1608-1634 (2015).
- [2] Zheng, W. *et al.* Lanthanide-doped upconversion nano-bioprobes: electronic structures, optical properties, and biodetection. *Chem. Soc. Rev.* **44**, 1379-1415 (2015).
- [3] Wang, F. & Liu, X. Recent advances in the chemistry of lanthanide-doped upconversion nanocrystals. *Chem. Soc. Rev.* **38**, 976-989 (2009).
- [4] Liu, X., Yan, C. H. & Capobianco, J. A. Photon upconversion nanomaterials. *Chem. Soc. Rev.* **44**, 1299-1301 (2015).
- [5] Eliseeva, S. V. & Bunzli, J. C. Lanthanide luminescence for functional materials and bio-sciences. *Chem. Soc. Rev.* **39**, 189-227 (2010).
- [6] Zhao, J. *et al.* Single-nanocrystal sensitivity achieved by enhanced upconversion luminescence. *Nat Nanotechnol* **8**, 729-734 (2013).
- [7] Zhou, J., Liu, Q., Feng, W., Sun, Y. & Li, F. Upconversion luminescent materials: advances and applications. *Chem. Rev.* **115**, 395-465 (2015).
- [8] Huang, X., Han, S., Huang, W. & Liu, X. Enhancing solar cell efficiency: the search for luminescent materials as spectral converters. *Chem. Soc. Rev.* **42**, 173-201 (2013).
- [9] Deng, R. *et al.* Temporal full-colour tuning through non-steady-state upconversion. *Nat Nanotechnol* **10**, 237-242 (2015).
- [10] Chen, S. *et al.* Near-infrared deep brain stimulation via upconversion nanoparticle-mediated optogenetics. *Science* **359**, 679-684 (2018).
- [11] Park, W., Lu, D. & Ahn, S. Plasmon enhancement of luminescence upconversion. *Chem. Soc. Rev.* **44**, 2940-2962 (2015).
- [12] Chen, G., Qiu, H., Prasad, P. N. & Chen, X. Upconversion nanoparticles: design, nanochemistry, and applications in theranostics.

Chem. Rev. **114**, 5161-5214 (2014).

- [13] Chen, G., Agren, H., Ohulchanskyy, T. Y. & Prasad, P. N. Light upconverting core-shell nanostructures: nanophotonic control for emerging applications. *Chem. Soc. Rev.* **44**, 1680-1713 (2015).
- [14] Li, X., Zhang, F. & Zhao, D. Lab on upconversion nanoparticles: optical properties and applications engineering via designed nanostructure. *Chem. Soc. Rev.* **44**, 1346-1378 (2015).
- [15] Halir, R. *et al.* Waveguide sub-wavelength structures: a review of principles and applications. *Laser & Photonics Reviews* **9**, 25-49 (2015).
- [16] Yan, R., Pausauskie, P., Huang, J. & Yang, P. Direct photonic-plasmonic coupling and routing in single nanowires. *Proceedings of the National Academy of Sciences* **106**, 21045-21050 (2009).
- [17] Barrelet, C. J., Greytak, A. B. & Lieber, C. M. Nanowire photonic circuit elements. *Nano Letters* **4**, 1981-1985 (2004).
- [18] Cadarso, V. J., Llobera, A., Puyol, M. & Schiff, H. Integrated Photonic Nanofences: Combining Subwavelength Waveguides with an Enhanced Evanescent Field for Sensing Applications. *ACS nano* **10**, 778-785 (2015).
- [19] De Angelis, F. *et al.* A hybrid plasmonic- photonic nanodevice for label-free detection of a few molecules. *Nano letters* **8**, 2321-2327 (2008).
- [20] Guo, X., Ying, Y. & Tong, L. Photonic nanowires: From subwavelength waveguides to optical sensors. *Accounts of chemical research* **47**, 656-666 (2013).
- [21] Law, M. *et al.* Nanoribbon waveguides for subwavelength photonics integration. *Science* **305**, 1269-1273 (2004).
- [22] Wang, P. *et al.* Polymer nanofibers embedded with aligned gold nanorods: a new platform for plasmonic studies and optical sensing. *Nano letters* **12**, 3145-3150 (2012).

- [23] Kasaya, K., Mitomi, O., Naganuma, M., Kondo, Y. & Noguchi, Y. A simple laterally tapered waveguide for low-loss coupling to single-mode fibers. *IEEE photonics technology letters* **5**, 345-347 (1993).
- [24] Liu, H., Edel, J. B., Bellan, L. M. & Craighead, H. Electrospun polymer nanofibers as subwavelength optical waveguides incorporating quantum dots. *Small* **2**, 495-499 (2006).
- [25] Pan, A. *et al.* Optical waveguide through CdS nanoribbons. *Small* **1**, 980-983 (2005).
- [26] Zhao, Y. S., Zhan, P., Kim, J., Sun, C. & Huang, J. Patterned growth of vertically aligned organic nanowire waveguide arrays. *ACS nano* **4**, 1630-1636 (2010).
- [27] Zhang, C., Zheng, J. Y., Zhao, Y. S. & Yao, J. Self-Modulated White Light Outcoupling in Doped Organic Nanowire Waveguides via the Fluctuations of Singlet and Triplet Excitons During Propagation. *Advanced Materials* **23**, 1380-1384 (2011).
- [28] O'Carroll, D., Lieberwirth, I. & Redmond, G. Microcavity effects and optically pumped lasing in single conjugated polymer nanowires. *Nature nanotechnology* **2**, 180-184 (2007).
- [29] Zhang, R., Yu, H. & Li, B. Active nanowaveguides in polymer doped with CdSe–ZnS core–shell quantum dots. *Nanoscale* **4**, 5856-5859 (2012).
- [30] Sun, L.-D., Wang, Y.-F. & Yan, C.-H. Paradigms and challenges for bioapplication of rare earth upconversion luminescent nanoparticles: small size and tunable emission/excitation spectra. *Accounts of chemical research* **47**, 1001-1009 (2014).
- [31] Wang, F. & Liu, X. Multicolor tuning of lanthanide-doped nanoparticles by single wavelength excitation. *Accounts of chemical research* **47**, 1378-1385 (2014).
- [32] Zheng, W. *et al.* Lanthanide-doped upconversion nano-bioprobes: electronic structures, optical properties, and biodetection. *Chemical Society Reviews* **44**, 1379-1415 (2015).

- [33] Chen, D. *et al.* Nd³⁺-Sensitized Ho³⁺ Single-Band Red Upconversion Luminescence in Core–Shell Nanoarchitecture. *The Journal of Physical Chemistry Letters* **6**, 2833-2840 (2015).
- [34] Wang, F. *et al.* Tuning upconversion through energy migration in core–shell nanoparticles. *Nature Materials* **10**, 968-973 (2011).
- [35] Chen, D., Xu, M. & Huang, P. Core@shell upconverting nanoarchitectures for luminescent sensing of temperature. *Sensors and Actuators B: Chemical* **231**, 576-583 (2016).
- [36] Langrock, C. *et al.* Highly efficient single-photon detection at communication wavelengths by use of upconversion in reverse-proton-exchanged periodically poled LiNbO₃ waveguides. *Optics letters* **30**, 1725-1727 (2005).
- [37] Chen, X. *et al.* Large Upconversion Enhancement in the "Islands" Au-Ag Alloy/NaYF₄: Yb³⁺, Tm³⁺/Er³⁺ Composite Films, and Fingerprint Identification. *Advanced Functional Materials* **25**, 5462-5471 (2015).
- [38] Zhu, H. *et al.* Lead halide perovskite nanowire lasers with low lasing thresholds and high quality factors. *Nature materials* **14**, 636-642 (2015).
- [39] Chen, B., Sun, T., Qiao, X., Fan, X. & Wang, F. Directional Light Emission in a Single NaYF₄ Microcrystal via Photon Upconversion. *Advanced Optical Materials* **3**, 1577-1581 (2015).
- [40] Zhang, Y. *et al.* Multicolor barcoding in a single upconversion crystal. *Journal of the American Chemical Society* **136**, 4893-4896 (2014).
- [41] Wang, X., Zhuang, J., Peng, Q. & Li, Y. A general strategy for nanocrystal synthesis. *Nature* **437**, 121-124 (2005).
- [42] Bai, X. *et al.* Concentration-controlled emission in LaF₃: Yb³⁺/Tm³⁺ nanocrystals: switching from UV to NIR regions. *Journal of Materials Chemistry* **22**, 24698-24704 (2012).
- [43] Chen, X. *et al.* Large Upconversion Enhancement in the “Islands”

- Au–Ag Alloy/NaYF₄: Yb³⁺, Tm³⁺/Er³⁺ Composite Films, and Fingerprint Identification. *Advanced Functional Materials* **25**, 5462–5471 (2015).
- [44] Yin, A., Zhang, Y., Sun, L. & Yan, C. Colloidal synthesis and blue based multicolor upconversion emissions of size and composition controlled monodisperse hexagonal NaYF₄: Yb, Tm nanocrystals. *Nanoscale* **2**, 953–959 (2010).
- [45] Zhao, J. *et al.* Single-nanocrystal sensitivity achieved by enhanced upconversion luminescence. *Nature nanotechnology* **8**, 729–734 (2013).
- [46] Pollnau, M., Gamelin, D., Lüthi, S., Güdel, H. & Hehlen, M. Power dependence of upconversion luminescence in lanthanide and transition-metal-ion systems. *Physical Review B* **61**, 3337 (2000).
- [47] Brites, C. D. *et al.* Instantaneous ballistic velocity of suspended Brownian nanocrystals measured by upconversion nanothermometry. *Nature Nanotechnology* (2016).
- [48] Liu, T., Xu, W., Bai, X. & Song, H. Tunable silica shell and its modification on photoluminescent properties of Y₂O₃: Eu³⁺@ SiO₂ nanocomposites. *Journal of Applied Physics* **111**, 064312 (2012).
- [49] Drozdowski, W. & Wojtowicz, A. J. Fast 20ns 5d–4f luminescence and radiation trapping in BaF₂: Ce. *Nuclear Instruments and Methods in Physics Research Section A: Accelerators, Spectrometers, Detectors and Associated Equipment* **486**, 412–416 (2002).
- [50] Tong, L. *et al.* Subwavelength-diameter silica wires for low-loss optical wave guiding. *Nature* **426**, 816–819 (2003).
- [51] Sokolov, V. *et al.* Determination of the refractive index of β -NaYF₄/Yb³⁺/Er³⁺/Tm³⁺ nanocrystals using spectroscopic refractometry. *Optics and Spectroscopy* **118**, 609–613 (2015).
- [52] Yi, Z. *et al.* Remarkable NIR Enhancement of Multifunctional Nanoprobes for In Vivo Trimodal Bioimaging and Upconversion Optical/T₂-Weighted MRI-Guided Small Tumor Diagnosis.

Advanced Functional Materials **25**, 7119-7129 (2015).

- [53] Maji, S. K. *et al.* Upconversion Nanoparticles as a Contrast Agent for Photoacoustic Imaging in Live Mice. *Advanced Materials* **26**, 5633-5638 (2014).
- [54] Wang, Y., Song, S., Liu, J., Liu, D. & Zhang, H. ZnO-Functionalized Upconverting Nanotheranostic Agent: Multi-Modality Imaging-Guided Chemotherapy with On-Demand Drug Release Triggered by pH. *Angewandte Chemie International Edition* **54**, 536-540 (2015).
- [55] Min, Y., Li, J., Liu, F., Yeow, E. K. L. & Xing, B. Near-Infrared Light-Mediated Photoactivation of a Platinum Antitumor Prodrug and Simultaneous Cellular Apoptosis Imaging by Upconversion-Luminescent Nanoparticles. *Angewandte Chemie* **126**, 1030-1034 (2014).
- [56] Wang, H.-Q., Batentschuk, M., Osvet, A., Pinna, L. & Brabec, C. J. Rare-Earth Ion Doped Up-Conversion Materials for Photovoltaic Applications. *Advanced Materials* **23**, 2675-2680 (2011).
- [57] Greybush, N. J. *et al.* Plasmon-Enhanced Upconversion Luminescence in Single Nanophosphor-Nanorod Heterodimers Formed through Template-Assisted Self-Assembly. *ACS Nano* **8**, 9482-9491 (2014).
- [58] Ivaturi, A. *et al.* Optimizing infrared to near infrared upconversion quantum yield of β -NaYF₄:Er³⁺ in fluoropolymer matrix for photovoltaic devices. *Journal of Applied Physics* **114**, 013505 (2013).
- [59] Li, X., Wang, R., Zhang, F. & Zhao, D. Engineering Homogeneous Doping in Single Nanoparticle To Enhance Upconversion Efficiency. *Nano Letters* **14**, 3634-3639 (2014).
- [60] Chen, G., Qiu, H., Prasad, P. N. & Chen, X. Upconversion Nanoparticles: Design, Nanochemistry, and Applications in Theranostics. *Chemical Reviews* **114**, 5161-5214 (2014).
- [61] Sarkar, S. *et al.* Giant Increase in the Metal-Enhanced Fluorescence of Organic Molecules in Nanoporous Alumina Templates and Large

- Molecule-Specific Red/Blue-Shift of the Fluorescence Peak. *Nano Letters* **14**, 5973-5978 (2014).
- [62] Wang, Y.-L. *et al.* Tailoring Plasmonic Enhanced Upconversion in Single NaYF₄:Yb³⁺/Er³⁺ Nanocrystals. *Scientific Reports* **5**, 10196 (2015).
- [63] Wu, D. M., García-Etxarri, A., Salleo, A. & Dionne, J. A. Plasmon-Enhanced Upconversion. *The Journal of Physical Chemistry Letters* **5**, 4020-4031 (2014).
- [64] Niu, W. *et al.* Synergetically Enhanced Near-Infrared Photoresponse of Reduced Graphene Oxide by Upconversion and Gold Plasmon. *Small* **10**, 3637-3643 (2014).
- [65] Saboktakin, M. *et al.* Metal-Enhanced Upconversion Luminescence Tunable through Metal Nanoparticle–Nanophosphor Separation. *ACS Nano* **6**, 8758-8766 (2012).
- [66] Schietinger, S., Aichele, T., Wang, H.-Q., Nann, T. & Benson, O. Plasmon-Enhanced Upconversion in Single NaYF₄:Yb³⁺/Er³⁺ Codoped Nanocrystals. *Nano Letters* **10**, 134-138 (2010).
- [67] Guo, L., Ferhan, A. R., Lee, K. & Kim, D.-H. Nanoarray-Based Biomolecular Detection Using Individual Au Nanoparticles with Minimized Localized Surface Plasmon Resonance Variations. *Analytical Chemistry* **83**, 2605-2612 (2011).
- [68] Feng, A. L. *et al.* Distance-dependent plasmon-enhanced fluorescence of upconversion nanoparticles using polyelectrolyte multilayers as tunable spacers. *Sci Rep* **5**, 7779 (2015).
- [69] Xu, W. *et al.* A novel strategy for improving upconversion luminescence of NaYF₄:Yb, Er nanocrystals by coupling with hybrids of silver plasmon nanostructures and poly(methyl methacrylate) photonic crystals. *Nano Research* **6**, 795-807 (2013).
- [70] Reineck, P. *et al.* Distance and Wavelength Dependent Quenching of Molecular Fluorescence by Au@SiO₂ Core–Shell Nanoparticles. *ACS Nano* **7**, 6636-6648 (2013).

- [71] Zhang, X. *et al.* Wavelength, Concentration, and Distance Dependence of Nonradiative Energy Transfer to a Plane of Gold Nanoparticles. *ACS Nano* **6**, 9283-9290 (2012).
- [72] Liu, X. *et al.* Probing the nature of upconversion nanocrystals: instrumentation matters. *Chem. Soc. Rev.* **44**, 1479-1508 (2015).
- [73] Walsh, B. M. in *Advances in Spectroscopy for Lasers and Sensing* 403-433 (Springer, 2006).
- [74] Yin, D. *et al.* Enhancing upconversion luminescence of NaYF₄:Yb/Er nanocrystals by Mo(3+) doping and their application in bioimaging. *Dalton Trans* **43**, 12037-12043 (2014).
- [75] Cheng, Q., Sui, J. & Cai, W. Enhanced upconversion emission in Yb³⁺ and Er³⁺ codoped NaGdF₄ nanocrystals by introducing Li⁺ ions. *Nanoscale* **4**, 779-784 (2012).
- [76] Zhao, C. *et al.* Li⁺ ion doping: an approach for improving the crystallinity and upconversion emissions of NaYF₄:Yb³⁺, Tm³⁺ nanoparticles. *Nanoscale* **5**, 8084-8089 (2013).
- [77] Hao, J., Zhang, Y. & Wei, X. Electric-induced enhancement and modulation of upconversion photoluminescence in epitaxial BaTiO₃:Yb/Er thin films. *Angew. Chem. Int. Ed. Engl.* **50**, 6876-6880 (2011).
- [78] Wisser, M. D. *et al.* Strain-induced modification of optical selection rules in lanthanide-based upconverting nanoparticles. *Nano Lett.* **15**, 1891-1897 (2015).
- [79] Liu, Q., Feng, W., Yang, T., Yi, T. & Li, F. Upconversion luminescence imaging of cells and small animals. *Nat Protoc* **8**, 2033-2044 (2013).
- [80] Zhou, B., Shi, B., Jin, D. & Liu, X. Controlling upconversion nanocrystals for emerging applications. *Nat Nanotechnol* **10**, 924-936 (2015).
- [81] Ye, X. *et al.* Morphologically controlled synthesis of colloidal upconversion nanophosphors and their shape-directed self-assembly.

Proc Natl Acad Sci U S A **107**, 22430-22435 (2010).

- [82] Auzel, F. Upconversion and anti-stokes processes with f and d ions in solids. *Chem. Rev.* **104**, 139-174 (2004).
- [83] Sun, L. D., Wang, Y. F. & Yan, C. H. Paradigms and challenges for bioapplication of rare earth upconversion luminescent nanoparticles: small size and tunable emission/excitation spectra. *Acc. Chem. Res.* **47**, 1001-1009 (2014).
- [84] Lei, L., Zhang, J. & Xu, S. The progress of single-band upconversion nanomaterials. *RSC Adv.* **6**, 81076-81084 (2016).
- [85] Zhou, L. *et al.* Single-band upconversion nanoprobe for multiplexed simultaneous in situ molecular mapping of cancer biomarkers. *Nat Commun* **6**, 6938 (2015).
- [86] Meruga, J. M., Baride, A., Cross, W., Kellar, J. J. & May, P. S. Red-green-blue printing using luminescence-upconversion inks. *J. Mater. Chem. C* **2**, 2221 (2014).
- [87] Wang, Z. *et al.* Size/morphology induced tunable luminescence in upconversion crystals: ultra-strong single-band emission and underlying mechanisms. *Nanoscale* **7**, 9552-9557 (2015).
- [88] Chen, D. *et al.* Intrinsic single-band upconversion emission in colloidal Yb/Er(Tm):Na₃Zr(Hf)F₇ nanocrystals. *Chem Commun (Camb)* **48**, 10630-10632 (2012).
- [89] Wang, Y. *et al.* Low-Temperature Fluorination Route to Lanthanide-Doped Monoclinic ScOF Host Material for Tunable and Nearly Single Band Up-Conversion Luminescence. *J. Phys. Chem. C* **118**, 10314-10320 (2014).
- [90] Chen, G., Liu, H., Somesfalean, G., Liang, H. & Zhang, Z. Upconversion emission tuning from green to red in Yb³⁺/Ho³⁺-codoped NaYF₄ nanocrystals by tridoping with Ce³⁺ ions. *Nanotechnology* **20**, 385704 (2009).
- [91] Wang, F. & Liu, X. Upconversion multicolor fine-tuning: Visible to

- near-infrared emission from lanthanide-doped NaYF₄ nanoparticles. *J. Am. Chem. Soc.* **130**, 5642-+ (2008).
- [92] Tian, G. *et al.* Mn²⁺ dopant-controlled synthesis of NaYF₄:Yb/Er upconversion nanoparticles for in vivo imaging and drug delivery. *Adv. Mater.* **24**, 1226-1231 (2012).
- [93] Wang, J., Wang, F., Wang, C., Liu, Z. & Liu, X. Single-band upconversion emission in lanthanide-doped KMnF₃ nanocrystals. *Angew. Chem. Int. Ed. Engl.* **50**, 10369-10372 (2011).
- [94] Chan, E. M. *et al.* Combinatorial discovery of lanthanide-doped nanocrystals with spectrally pure upconverted emission. *Nano Lett.* **12**, 3839-3845 (2012).
- [95] Nadort, A., Zhao, J. & Goldys, E. M. Lanthanide upconversion luminescence at the nanoscale: fundamentals and optical properties. *Nanoscale* **8**, 13099-13130 (2016).
- [96] Gargas, D. J. *et al.* Engineering bright sub-10-nm upconverting nanocrystals for single-molecule imaging. *Nat Nanotechnol* **9**, 300-305 (2014).
- [97] Li, Z., Zhang, Y. & Jiang, S. Multicolor Core/Shell-Structured Upconversion Fluorescent Nanoparticles. *Adv. Mater.* **20**, 4765-4769 (2008).
- [98] Zhang, Z., Li, J. C. & Jiang, Q. Modelling for size-dependent and dimension-dependent melting of nanocrystals. *J. Phys. D: Appl. Phys.* **33**, 2653 (2000).
- [99] Tikhomirov, V. K. *et al.* Optical nanoheater based on the Yb³⁺-Er³⁺ co-doped nanoparticles. *Opt. Express* **17**, 11794-11798 (2009).
- [100] Boyd, D. C. *et al.* in *Kirk-Othmer Encyclopedia of Chemical Technology* (John Wiley & Sons, Inc., 2000).
- [101] Gupta, P. K. Rigidity, Connectivity, and Glass-Forming Ability. *J. Am. Ceram. Soc.* **76**, 1088-1095 (1993).
- [102] Gupta, P. K. Non-crystalline solids: glasses and amorphous solids. *J.*

Non-Cryst. Solids **195**, 158-164 (1996).

- [103] Tu, D. *et al.* Breakdown of crystallographic site symmetry in lanthanide-doped NaYF₄ crystals. *Angew. Chem. Int. Ed. Engl.* **52**, 1128-1133 (2013).
- [104] Judd, B. R. Optical Absorption Intensities of Rare-Earth Ions. *Phys. Rev.* **127**, 750-761 (1962).
- [105] Ofelt, G. S. Intensities of Crystal Spectra of Rare-Earth Ions. *The Journal of Chemical Physics* **37**, 511-520 (1962).
- [106] Hehlen, M. P., Brik, M. G. & Krämer, K. W. 50th anniversary of the Judd–Ofelt theory: An experimentalist's view of the formalism and its application. *J. Lumin.* **136**, 221-239 (2013).
- [107] Krupke, W. Radiative transition probabilities within the 4 f 3 ground configuration of Nd: YAG. *IEEE J. Quantum Electron.* **7**, 153-159 (1971).
- [108] Luo, W., Liao, J., Li, R. & Chen, X. Determination of Judd-Ofelt intensity parameters from the excitation spectra for rare-earth doped luminescent materials. *Phys. Chem. Chem. Phys.* **12**, 3276-3282 (2010).
- [109] Yao, G., Lin, C., Meng, Q., Stanley May, P. & Berry, M. T. Calculation of Judd-Ofelt parameters for Er³⁺ in β -NaYF₄: Yb³⁺, Er³⁺ from emission intensity ratios and diffuse reflectance spectra. *J. Lumin.* **160**, 276-281 (2015).
- [110] Quimby, R. S. & Miniscalco, W. J. Modified Judd–Ofelt technique and application to optical transitions in Pr³⁺-doped glass. *J. Appl. Phys.* **75**, 613-615 (1994).
- [111] Weber, M. J. Probabilities for Radiative and Nonradiative Decay of Er³⁺ in LaF₃. *Phys. Rev.* **157**, 262-272 (1967).
- [112] Nachimuthu, P. & Jagannathan, R. Judd-Ofelt Parameters, Hypersensitivity, and Emission Characteristics of Ln³⁺ (Nd³⁺, Ho³⁺, and Er³⁺) Ions Doped in PbO-PbF₂ Glasses. *J. Am. Ceram. Soc.* **82**,

387-392 (1999).

- [113] Jørgensen, C. K. & Reisfeld, R. Judd-Ofelt parameters and chemical bonding. *J. Less-Common Met.* **93**, 107-112 (1983).
- [114] Ebendorff-Heidepriem, H. & Ehrt, D. Tb³⁺ f-d absorption as indicator of the effect of covalency on the Judd-Ofelt Ω_2 parameter in glasses. *J. Non-Cryst. Solids* **248**, 247-252 (1999).
- [115] Wu, S. *et al.* Non-blinking and photostable upconverted luminescence from single lanthanide-doped nanocrystals. *Proceedings of the National Academy of Sciences* **106**, 10917-10921 (2009).
- [116] Berthou, H. & Jørgensen, C. K. Optical-fiber temperature sensor based on upconversion-excited fluorescence. *Opt. Lett.* **15**, 1100-1102 (1990).
- [117] Pollnau, M., Gamelin, D. R., Lüthi, S. R., Güdel, H. U. & Hehlen, M. P. Power dependence of upconversion luminescence in lanthanide and transition-metal-ion systems. *Physical Review B* **61**, 3337-3346 (2000).
- [118] Yu, W., Xu, W., Song, H. & Zhang, S. Temperature-dependent upconversion luminescence and dynamics of NaYF₄:Yb³⁺/Er³⁺ nanocrystals: influence of particle size and crystalline phase. *Dalton Trans* **43**, 6139-6147 (2014).
- [119] Xu, X. *et al.* Phonon-Assisted Population Inversion in Lanthanide-Doped Upconversion Ba₂LaF₇ Nanocrystals in Glass-Ceramics. *Adv. Mater.* **28**, 8045-8050 (2016).
- [120] Martín-Rodríguez, R., Rabouw, F. T., Trevisani, M., Bettinelli, M. & Meijerink, A. Upconversion Dynamics in Er³⁺-Doped Gd₂O₂S: Influence of Excitation Power, Er³⁺Concentration, and Defects. *Adv. Opt. Mater.* **3**, 558-567 (2015).
- [121] Suyver, J. F., Aebischer, A., García-Revilla, S., Gerner, P. & Güdel, H. U. Anomalous power dependence of sensitized upconversion luminescence. *Physical Review B* **71** (2005).

- [122] Wang, G. *et al.* Intense ultraviolet upconversion luminescence from hexagonal NaYF₄:Yb³⁺/Tm³⁺ microcrystals. *Opt. Express* **16**, 11907-11914 (2008).
- [123] Reisfeld, R. & Eckstein, Y. Dependence of spontaneous emission and nonradiative relaxations of Tm³⁺ and Er³⁺ on glass host and temperature. *The Journal of Chemical Physics* **63**, 4001 (1975).
- [124] Carnall, W., Crosswhite, H. & Crosswhite, H. M. Energy level structure and transition probabilities in the spectra of the trivalent lanthanides in LaF₃. [Tables, diagrams]. (Argonne National Lab., IL (USA), 1978).
- [125] Cotter, D. *et al.* Nonlinear Optics for High-Speed Digital Information Processing. *Science* **286**, 1523-1528 (1999).
- [126] Loerting, T., Brazhkin, V. V. & Morishita, T. in *Adv. Chem. Phys.* 29-82 (John Wiley & Sons, Inc., 2009).
- [127] Smit, M., van der Tol, J. & Hill, M. Moore's law in photonics. *Laser & Photonics Reviews* **6**, 1-13 (2012).
- [128] Vahala, K. J. Optical microcavities. *Nature* **424**, 839 (2003).
- [129] Hill, M. T. & Gather, M. C. Advances in small lasers. *Nature Photonics* **8**, 908-918 (2014).
- [130] Humar, M. & Yun, S. H. Intracellular microlasers. *Nat Photonics* **9**, 572-576 (2015).
- [131] Gather, M. C. & Yun, S. H. Single-cell biological lasers. *Nature Photonics* **5**, 406-410 (2011).
- [132] Kim, T.-i. *et al.* Injectable, Cellular-Scale Optoelectronics with Applications for Wireless Optogenetics. *Science* **340**, 211-216 (2013).
- [133] Barland, S. *et al.* Cavity solitons as pixels in semiconductor microcavities. *Nature* **419**, 699 (2002).
- [134] Huang, M. C., Zhou, Y. & Chang-Hasnain, C. J. A surface-emitting laser incorporating a high-index-contrast subwavelength grating.

Nature photonics **1**, 119 (2007).

- [135] Kapon, E. & Sirbu, A. Long-wavelength VCSELs: Power-efficient answer. *Nature Photonics* **3**, 27 (2009).
- [136] Spillane, S. M., Kippenberg, T. J. & Vahala, K. J. Ultralow-threshold Raman laser using a spherical dielectric microcavity. *Nature* **415**, 621 (2002).
- [137] Armani, D. K., Kippenberg, T. J., Spillane, S. M. & Vahala, K. J. Ultra-high-Q toroid microcavity on a chip. *Nature* **421**, 925-928 (2003).
- [138] Zhu, J. *et al.* On-chip single nanoparticle detection and sizing by mode splitting in an ultrahigh-Q microresonator. *Nature Photonics* **4**, 46-49 (2009).
- [139] Wu, S. *et al.* Monolayer semiconductor nanocavity lasers with ultralow thresholds. *Nature* **520**, 69-72 (2015).
- [140] Colombelli, R. *et al.* Quantum cascade surface-emitting photonic crystal laser. *Science* **302**, 1374-1377 (2003).
- [141] Park, H.-G. *et al.* Electrically driven single-cell photonic crystal laser. *Science* **305**, 1444-1447 (2004).
- [142] Khajavikhan, M. *et al.* Thresholdless nanoscale coaxial lasers. *Nature* **482**, 204-207 (2012).
- [143] Min, B. *et al.* High-Q surface-plasmon-polariton whispering-gallery microcavity. *Nature* **457**, 455-458 (2009).
- [144] Oulton, R. F. *et al.* Plasmon lasers at deep subwavelength scale. *Nature* **461**, 629-632 (2009).
- [145] Jin, L. M., Chen, X., Siu, C. K., Wang, F. & Yu, S. F. Enhancing Multiphoton Upconversion from NaYF₄:Yb/Tm@NaYF₄ Core-Shell Nanoparticles via the Use of Laser Cavity. *ACS Nano* **11**, 843-849 (2017).
- [146] Zhu, H. *et al.* Amplified spontaneous emission and lasing from

- lanthanide-doped up-conversion nanocrystals. *ACS Nano* **7**, 11420-11426 (2013).
- [147] Chen, X. *et al.* Confining energy migration in upconversion nanoparticles towards deep ultraviolet lasing. *Nat Commun* **7**, 10304 (2016).
- [148] Fernandez-Bravo, A. *et al.* Continuous-wave upconverting nanoparticle microlasers. *Nat Nanotechnol* **13**, 572-577 (2018).
- [149] Mhibik, O. *et al.* An ultra-narrow linewidth solution-processed organic laser. *Light: Science & Applications* **5**, e16026 (2016).
- [150] Myers, T. L. *et al.* Free-running frequency stability of mid-infrared quantum cascade lasers. *Opt. Lett.* **27**, 170-172 (2002).
- [151] Faist, J. *et al.* Quantum Cascade Laser. *Science* **264**, 553-556 (1994).
- [152] Pariente, G., Gallet, V., Borot, A., Gobert, O. & Quéré, F. Space-time characterization of ultra-intense femtosecond laser beams. *Nature Photonics* **10**, 547 (2016).
- [153] Siddiqui, M. *et al.* High-speed optical coherence tomography by circular interferometric ranging. *Nature Photonics* **12**, 111-116 (2018).
- [154] Luo, L.-W. *et al.* WDM-compatible mode-division multiplexing on a silicon chip. *Nat. Commun.* **5**, 3069 (2014).
- [155] Karl, N. J., McKinney, R. W., Monnai, Y., Mendis, R. & Mittleman, D. M. Frequency-division multiplexing in the terahertz range using a leaky-wave antenna. *Nature Photonics* **9**, 717 (2015).
- [156] Francois, A. & Himmelhaus, M. Whispering gallery mode biosensor operated in the stimulated emission regime. *Appl. Phys. Lett.* **94**, 031101 (2009).
- [157] Fujita, M., Ushigome, R. & Baba, T. Continuous wave lasing in GaInAsP microdisk injection laser with threshold current of 40 μ A. *Electron. Lett.* **36**, 1 (2000).
- [158] Gorodetsky, M. L. & Ilchenko, V. S. Optical microsphere resonators:

- optimal coupling to high-Q whispering-gallery modes. *J. Opt. Soc. Am. B* **16**, 147-154 (1999).
- [159] Jiang, X. F., Zou, C. L., Wang, L., Gong, Q. & Xiao, Y. F. Whispering-gallery microcavities with unidirectional laser emission. *Laser & Photonics Reviews* **10**, 40-61 (2016).
- [160] Scheps, R. Upconversion laser processes. *Progress in Quantum Electronics* **20**, 271-358 (1996).
- [161] Liu, Y. *et al.* Amplified stimulated emission in upconversion nanoparticles for super-resolution nanoscopy. *Nature* **543**, 229-233 (2017).
- [162] Huang, M. C., Zhou, Y. & Chang-Hasnain, C. J. A nanoelectromechanical tunable laser. *Nature Photonics* **2**, 180 (2008).
- [163] Moon, B. S., Kim, H. E. & Kim, D. H. Ultrafast Single-Band Upconversion Luminescence in a Liquid-Quenched Amorphous Matrix. *Adv. Mater.* **30**, e1800008 (2018).
- [164] He, L., Özdemir, Ş. K. & Yang, L. Whispering gallery microcavity lasers. *Laser & Photonics Reviews* **7**, 60-82 (2013).
- [165] Righini, G. *et al.* Whispering gallery mode microresonators: fundamentals and applications. *Rivista del Nuovo Cimento* **34**, 435-488 (2011).
- [166] Gu, F. *et al.* Single whispering-gallery mode lasing in polymer bottle microresonators via spatial pump engineering. *Light Sci Appl* **6**, e17061 (2017).
- [167] Hayenga, W. E. & Khajavikhan, M. Unveiling the physics of microcavity lasers. *Light Sci Appl* **6**, e17091 (2017).
- [168] Tang, S. K. Y., Derda, R., Quan, Q., Lončar, M. & Whitesides, G. M. Continuously tunable microdroplet-laser in a microfluidic channel. *Opt. Express* **19**, 2204-2215 (2011).
- [169] Kippenberg, T. J. Particle sizing by mode splitting. *Nature Photonics* **4**, 9-10 (2010).

- [170] Noto, M., Keng, D., Teraoka, I. & Arnold, S. Detection of protein orientation on the silica microsphere surface using transverse electric/transverse magnetic whispering gallery modes. *Biophys. J.* **92**, 4466-4472 (2007).
- [171] Guan, G., Arnold, S. & Otugen, V. Temperature Measurements Using a Microoptical Sensor Based on Whispering Gallery Modes. *AIAA J.* **44**, 2385-2389 (2006).
- [172] Cai, Z. P., Xu, H. Y., Stéphan, G. M., Féron, P. & Mortier, M. Red-shift in Er:ZBLALiP whispering gallery mode laser. *Opt. Commun.* **229**, 311-315 (2004).
- [173] Ta, V. D., Chen, R. & Sun, H. D. Tuning whispering gallery mode lasing from self-assembled polymer droplets. *Sci Rep* **3**, 1362 (2013).
- [174] Humar, M., Ravnik, M., Pajk, S. & Muševič, I. Electrically tunable liquid crystal optical microresonators. *Nature Photonics* **3**, 595-600 (2009).
- [175] Kippenberg, T. J. A. *Nonlinear optics in ultra-high Q whispering-gallery optical microcavities*, California Institute of Technology, (2004).

국문 초록

란탄족 이온이 도핑된 구조적으로 무질서한 호스트 매트릭스에서의 상향변환 특성 연구

서울대학교

재료공학부

문 병 석

란탄족 3가 이온 (Ln^{3+})이 도핑 되어 있는 무기질 호스트 물질은 4f-4f 전이로부터 비롯되는 사다리형 구조의 촘촘한 에너지 레벨을 갖으며, 이를 통해 상향변환이라는 고유한 광학 현상을 나타낸다. 상향변환은 낮은 에너지의 광자를 순차적으로 흡수하여 높은 에너지의 광자로 변환 및 방출하는 현상으로 근적외선 빛을 가시광선 혹은 자외선 빛으로 바꾸어 줄 수 있어 태양 전지를 위한 에너지 하베스팅, 3D 체적 디스플레이 또는 심뇌 광유전학과 같은 응용 분야에 유망하다. 이와 같은 다양한 응용 분야에 활용하기 위해, 최근 몇 년간 상향변환 효율을 높이고 발광 스펙트럼을 제어하려는 연구 노력이 집중되어 왔다. 란탄족 이온의 광학 특성은 결합하고 있는 호스트 이온으로부터

비롯되는 비-중심대칭결정장과의 상호 작용에 의해 양자역학적으로 결정되기 때문에, 상향변환 특성을 향상시키기 위한 가장 강력한 접근법 중 하나는 ‘호스트 엔지니어링’이라고 할 수 있다. 일반적으로 낮은 결합 대칭성을 갖는 호스트 매트릭스는 더 큰 비-중심대칭결정장 상호 작용을 가져오며, 이로 인해 높은 상향변환 효율을 갖는다. 호스트 매트릭스의 결합 대칭성을 파괴하기 위해, 외부 전기장 및 기계적 압력을 가하거나 침입형 불순물을 도핑하는 등 다양한 전략이 시도되었다. 그러나 현재까지 시도된 접근법들은 무기물질이 가지고 있는 강력한 결합 특성, 즉 단거리-영역(1차 배위권 내 결합구조) 내에 존재하는 대칭성을 극복하지 못하였기 때문에 호스트 엔지니어링을 통한 성능 향상의 잠재력은 제한되어 왔다.

본 학위논문에서는 호스트 매트릭스 내에 단거리-영역 질서를 갖지 않는 새로운 종류의 상향변환 호스트 물질을 연구한다. 이 물질은 용융된 상향변환 물질을 빠른 속도로 급랭하여 제조되었으며 비정질 미세구조를 갖기에 강력한 비-중심대칭결정장을 생성한다. 이 효과로 Er^{3+} 는 향상된 발광 전이 확률을 갖을 수 있으며, 결과적으로 기존보다 매우 빠른 감쇠시간과 기존보다 밝은 녹색 단일-밴드 상향변환 발광이 시연되었다. 이 현상은 포논 생성이 수반되는 복잡한 에너지 전달 경로를 통해 실현된 적색 또는 NIR 영역에서의 단일-밴드 상향변환과 달리 최소한의 에너지 손실을 통해 2광자 상향변환을

실현한다. 또한 이 현상으로 인해 발광 전이 확률의 균형이 변함에 따라, 교차-이완 및 에너지 역전달과 같은 유해한 비방사성 에너지 전달이 효과적으로 완화된다. 이 독특한 특징은 란타늄족 이온의 밀도 반전을 확립하는데 중요한 역할을 하며, 이로 인해 지금까지 보고된 다른 재료에 비해 매우 효율적인 상향변환 레이저를 구현할 수 있었다. 구조적으로 무질서한 호스트 매트릭스의 개발 및 분석을 통해 얻어진 위와 같은 발견들은 미래의 상향변환 기반 소자를 설계하는데 귀중한 통찰력을 제공할 것이며, 이는 상향변환 물질이 갖는 잠재적 응용 분야의 실현을 위해 활용될 것이다.

주요어: 란타늄족이 도핑된 무기물질, 상향변환, 호스트 엔지니어링,
단일-밴드 발광, 마이크로 레이저

학 번: 2014-21475